# Planar beam-forming antenna array for 60-GHz broadband communication

**Please check the document version of this publication:**

# Planar Beam-forming Antenna Array for 60-GHz Broadband Communication

# Planar Beam-forming Antenna Array for 60-GHz Broadband Communication

PROEFSCHRIFT

ter verkrijging van de graad van doctor aan de
Technische Universiteit Eindhoven, op gezag van de
Rector Magnificus, prof.dr.ir. C.J. van Duijn, voor een
commissie aangewezen door het College voor
Promoties in het openbaar te verdedigen
op maandag 16 maart 2009 om 16.00 uur

door

Johannes Antonius Gerardus Akkermans

geboren te Wouw

Dit proefschrift is goedgekeurd door de promotoren:

prof.dr.ir. E.R. Fledderus
en
prof.Dr.-Ing. T. Kürner

Copromotor:
dr.ir. M.H.A.J. Herben

Cover title "Riding the millimeter wave"; cover design by Johannes Akkermans.

Samenstelling van de promotiecommissie:

prof. dr. ir. A.C.P.M. Backx, voorzitter
prof. dr. ir. E.R. Fledderus, Technische Universiteit Eindhoven, eerste promotor
prof. Dr.-Ing. T. Kürner, Technische Universität Braunschweig, tweede promotor
dr. ir. M.H.A.J. Herben, Technische Universiteit Eindhoven, co-promotor
dr. ir. P.F.M. Smulders, Technische Universiteit Eindhoven
prof. dr. ir. D. de Zutter, Universiteit Gent
dr. ir. D. Liu, Thomas J. Watson Research Center
dr. ir. M.C. van Beurden, Technische Universiteit Eindhoven

SiGi Spot **TU/e** Technische Universiteit **Eindhoven** University of Technology    Ministerie van Economische Zaken

# Summary

The 60-GHz frequency band can be employed to realise the next-generation wireless high-speed communication that is capable of handling data rates of multiple gigabits per second. Advances in silicon technology allow the realisation of low-cost radio frequency (RF) front-end solutions. Still, to obtain the link-budget that is required for wireless gigabit-per-second communication, antenna arrays are needed that have sufficient gain and that support beam-forming. This requires the realisation of antenna arrays that maintain a high radiation efficiency while operating at millimeter-wave frequencies. Moreover, the antenna array and the RF front-end should be integrated into a single low-cost package that can be realised in a standard production process. In this work, an antenna solution is presented that meets these requirements.

The relevant production processes that can be used for antennas and packaging realise planar multi-layered structures. Therefore, the modelling of passive electromagnetic structures in stratified media is investigated. A computationally efficient modelling technique is employed that provides an in-depth analysis of the physical behaviour of the electromagnetic structure. The modelling technique is used to design an antenna element that can be realised in planar technology and that can be placed in an array configuration. This antenna element is named the balanced-fed aperture-coupled patch antenna. In the design, the radiation efficiency is optimised through the use of two distant coupling apertures that minimise surface-wave losses and significantly enlarge the bandwidth of the antenna. To improve the front-to-back ratio, a reflector element is introduced. Both these design strategies are used together for the first time, to enhance the global efficiency of the antenna. The antenna is realised in printed circuit-board (PCB) technology. To validate the performance of the antenna element, a special measurement setup is developed that characterises the bandwidth and radiation pattern of millimeter-wave antennas.

To maximise the performance of the antenna, an optimisation algorithm is presented that optimises the bandwidth and radiation efficiency of the antenna element. This algorithm gives the designer the flexibility to obtain the best antenna design for the

iv

considered application. Hereafter, the antenna element is placed in an array config-
uration that enables beam-forming. The performance of the beam-forming antenna
array is investigated in terms of radiation efficiency, bandwidth and gain. Measure-
ments of realised antenna arrays show that the antenna array can be employed to
obtain the required gain under beam-forming conditions.

Furthermore, the integration of the antenna array and the RF front-end is investi-
gated. The packaging of antenna array and RF front-end is discussed and a demon-
strator is realised in PCB technology that integrates an RF power amplifier and an
antenna element. It is shown that planar technology can be successfully employed to
realise a package that embeds the antenna array and that supports the RF front-end.
The presented concepts can be readily used for the realisation of a transceiver pack-
age that embeds a beam-forming antenna array and that supports gigabit-per-second
communication.

# Contents

# Introduction

## 1.1 Wireless communication

Wireless communication is omnipresent in our society. It is used for cellular telephony, short-range communication, product identification, data transfer, sensor networks and many other applications. Wireless communication relies on the transmission of information through electromagnetic (EM) waves. The coupling between these EM waves and the electronic devices that employ wireless communication is realised through antennas. Although many antennas are not directly visible due to the fact that they are embedded within the devices, they are crucial for reliable communication. Moreover, as the number of wireless applications increases, the performance of the antenna structures becomes more important to retain wireless connections between all these devices. Therefore, smart antenna structures are needed that support a multitude of applications and frequency bands.

## 1.2 Broadband communication in the 60-GHz frequency band

The vast majority of current wireless applications operates within the frequency range from approximately 1 to 6 GHz. This is strengthened by the ample availability of

radio frequency (RF) components for this frequency range. The realisation of wireless communication systems can therefore be well-controlled and low-cost, which explains the rapid expansion of these systems. The result of the expansion is a scarcity of available bandwidth and allowable transmit power. Rigorous spectrum and energy limitations have been introduced to avoid interference between wireless communication services. These services are now forced to make a trade-off between quality, speed and availability of information transfer. Basically, present wireless systems have to cope with their own succes.

Simultaneously, a trend that is observed in wireless communication systems is the demand for the support of increasing data rates over decreasing distances. Wireless communication systems have evolved from cellular telephony with data rates of kilobits per second (kbps) over distances of kilometers to wireless local area networks (WLANs) and wireless personal area networks (WPANs) that communicate with megabits per second (Mbps) over distances of meters. The use of current frequency bands limits further evolvement to higher data rates and shorter distances for two main reasons. First, the bandwidth of these systems is limited and this puts a limit on the achievable data rate. Second, interference limits the operation of parallel systems that operate within a limited range of each other.

To alleviate these problems and to significantly increase the data-rate potential of wireless systems, new frequency bands should be exploited. This explains the increasing interest to use the license-free frequency band around 60 GHz for short-range communication. This frequency band has an available bandwidth of about 7 GHz worldwide. For example, the United States allocated the frequency band from 57 to 64 GHz [1], and in Europe a 9 GHz bandwidth from 57 to 66 GHz is recommended. Wireless systems that use this frequency band have the potential to achieve data rates of multiple gigabits per second (Gbps). In comparison, current wireless local area network (WLAN) systems have an available bandwidth of about 150 MHz (i.e., 0.15 GHz) [2]. The use of the 60 GHz frequency band can provide an increase in data rate of 10 to 100 times and therefore it has the potential to provide the next step in high-data-rate wireless systems.

To employ the potential of the 60-GHz frequency band, low-cost wireless RF front-ends are needed that operate at these high frequencies. A block diagram of a typical wireless transceiver system is shown in Fig. 1.1 [3]. The transmitter (TX) RF front-end consists of an up-converter that converts the baseband signal to the RF domain, a power amplifier (PA) that amplifies the transmitted signal and an antenna that transmits the RF signal. This RF signal propagates in the environment and is received, possibly via multiple reflections, by the receive antenna of the receiver (RX) front-end. In the receiver, a low-noise amplifier (LNA) amplifies the received signal and a down-converter converts the RF signal to baseband.

The active components that are needed for the up-conversion, down-conversion and amplification (e.g., voltage controlled oscillator, mixer, phase shifter, PA, LNA) can
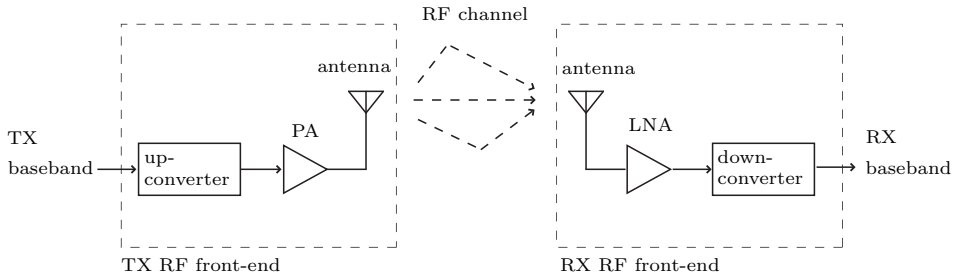
Figure 1.1: Block diagram of a transceiver system.

be realised in silicon manufacturing technology [4, 5, 6], which allows for a low-cost solution that is realised as one integrated circuit (IC). The antenna can be placed on the IC as well, but the performance of such an antenna is limited because of substrate losses. Reported radiation efficiencies of antennas that are realised in a standard silicon chip proces are less than 10% [7], [8]. Therefore, antennas cannot be placed on the IC as long as link-budget requirements are critical. In these cases, the antennas need to be placed off-chip and an RF interconnection between IC and antenna needs to be realised.

For multiple Gbps transmission in the 60-GHz band, the link-budget requirements are indeed stringent [9]. Intuitively, this can be derived from Friis' free-space transmission formula (see e.g. [10]) that relates the ratio of transmitted power $P_t$ and received power $P_r$ in free-space conditions to the wavelength, viz,

$$\frac{P_r}{P_t} = \frac{G_t G_r \lambda^2}{(4\pi R)^2},\tag{1.1}$$

where $G_t$ is the gain of the transmit antenna, $G_r$ is the gain of the receive antenna, $\lambda$ is the wavelength of the RF carrier and $R$ is the distance between the transmit and receive antenna. From Friis' transmission formula it is immediately observed that as the frequency increases, i.e., the wavelength decreases, the ratio of transmitted and received power decreases. To compensate for this decrease in received power, the distance between transmit and receive antenna should be decreased and the gain of the transmit and receive antenna should be increased. Obviously, the distance between transmit and receive antenna depends on the application and is not something that can be adjusted easily. Therefore, the gain of the transmit and receive antenna should be increased. This is the real challenge of 60-GHz communication. Antenna designs are needed that realise sufficient gain under varying conditions, i.e., in line-of-sight (LOS), non-LOS and mobile scenarios. Because a high-gain antenna has a small beam-width it is important that the antenna can perform adaptive beam-forming such that the RF channel is optimised and the user is provided with the highest data rate possible [11].
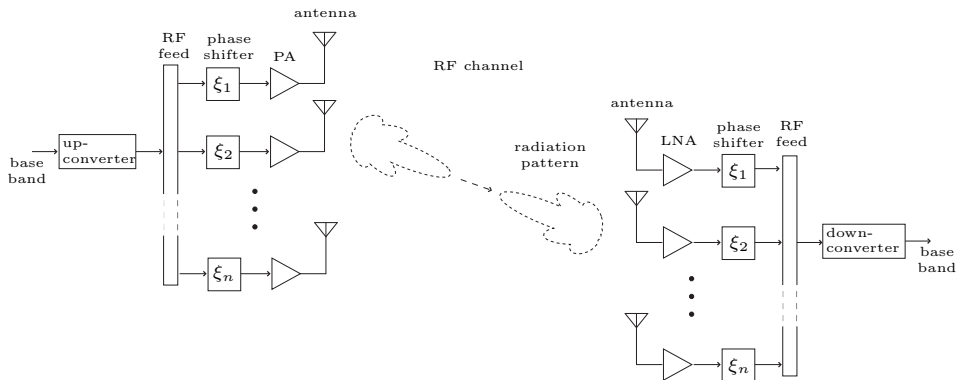
Figure 1.2: Block diagram of an active phased-array transceiver system with RF beam-forming.

## 1.3   Adaptive beam-forming antennas

To realise adaptive beam-forming antennas, active phased antenna arrays can be used [12]. These antenna arrays consist of multiple antenna elements that all have their own phase shifter. These phase shifters control the radiation pattern of the antenna array. The gain of the antenna array depends on the number of antenna elements. By increasing the number of elements the total gain of the antenna array can be increased as well. Therefore, the active phased array topology is a flexible solution that can be used for applications that have different gain requirements. An additional advantage of the active antenna array is that each antenna element can be equipped with a PA or LNA. As the operation frequency increases, it becomes more difficult to realise an amplifier with a large gain and therefore, the use of multiple amplifiers in parallel is advantageous since it alleviates the requirements on the PA and LNA.

The block diagram of an active phased-array transceiver is shown in Fig. 1.2. In this transceiver, beam-forming is realised in the RF domain. Multiple antennas are used and each antenna element has its own PA/LNA and phase shifter. An RF feed network distributes the RF signals between the mixer and the phase shifters. It is noted that from an antenna point-of-view it does not matter which beam-forming topology is applied in the RF front-end. Alternative topologies for beam-forming are possible as well. For example, beam-forming can be performed at the mixer stage or at baseband [13]. The advantage of RF beam-forming is that it minimises the number of RF components that is needed, since only one VCO and one mixer is needed per transmitter/receiver. Therefore this is an important topology for 60-GHz transceiver systems. The disadvantage is that it requires a phase shifter that operates at 60 GHz.

## 1.4  Packaging

The integration of the RF IC and the antenna array should be given careful consideration at these relatively high frequencies [14]. To allow for a simple integration with the RF IC, the antenna has to be realised in a planar manufacturing technology. Flip-chip technology can be employed to provide a reliable RF interconnection between the RF IC and the antenna [15]. In this work, printed circuit-board (PCB) technology is chosen for the manufacturing of the antenna array since it is a mature and low-cost technology that is easily accessible.

PCB technology can be used for the realisation of the antenna array, but it can also be used for the realisation of the complete transceiver package. The PCB can protect the RF IC and can also embed the antenna array and the required circuitry for the control of the transceiver. The materials that are used for the realisation of this package should be chosen carefully to obtain good performance at millimeter-wave frequencies. Moreover, the influence of etching and alignment tolerances should be taken into account to obtain a robust design. Additionally, the flip-chip interconnection between the RF IC and the PCB needs to be characterised carefully to retain the performance of the transceiver.

## 1.5  Background and objectives

This work is part of the SiGi-Spot project (IGC0503) that is funded by the Dutch ministry of Economic affairs within the IOP-GenCom programme. The project partners are Technische Universiteit Eindhoven, Technische Universiteit Delft and TNO Science and Industry. The goal of this project is to investigate low-cost radio technologies that employ the 60-GHz frequency band for ultra-fast data transport. The project supports five researchers (postdoctoral and Ph.D. students) and investigates

- application scenarios and user and system requirements,
- antenna design,
- RF front-end design,
- baseband algorithms and channel coding,
- higher layer protocols.

The research in this thesis focuses on the antenna design. The objective is to come up with 60-GHz antenna solutions that are tailored for low-cost, high capacity and
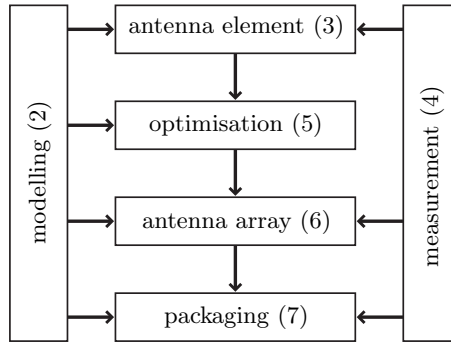
Figure 1.3: Structure of the thesis. The number in between the brackets denotes the associated chapter.

effective coverage.  To realise a low-cost antenna solution, planar technology is employed.  A high capacity can only be realised when the whole available bandwidth is supported by the antenna and by providing sufficient antenna gain.  To provide effective coverage, an antenna is needed that supports beam-forming.

## 1.6  Outline of the thesis

The outline of the thesis is depicted in Fig. 1.3.  Since the antenna is realised in a planar manufacturing technology, the modelling of electromagnetic structures in planar, or stratified, media is discussed first.  This can be found in Chapter 2, where also the evaluation of the radiation pattern and input impedance of antenna structures is discussed. The modelling techniques that are presented here have been used throughout the thesis.  In Chapter 3 the design of an antenna element is presented that combines good performance in bandwidth and radiation efficiency and that fulfills the requirements for 60-GHz communication.  This antenna element is named the balanced-fed aperture-coupled patch (BFACP) antenna.  The measurement and verification of millimeter-wave antenna structures is a complicated task.  Therefore, a measurement setup is proposed in Chapter 4 that allows for an accurate verification of the proposed antenna element.

An optimisation technique is discussed in Chapter 5 that can be used to optimise EM structures.  This technique is employed to optimise both the bandwidth and the radiation efficiency of the BFACP antenna element.  The optimised antenna element is used in an array configuration to realise a beam-forming antenna array in Chapter 6. The integration of the antenna element and the active electronics is investigated in Chapter 7.  A PCB package is proposed and realised that integrates the antenna and RF electronics into one package. It is shown that the presented concepts can be readily used for the realisation of a transceiver package that embeds a beam-forming

antenna array and that supports gigabit-per-second communication.

## 1.7 Contributions of this thesis

The main contributions of the work that is presented in this thesis are listed as follows:

- A planar BFACP antenna element is designed in Chapter 3 that combines a high radiation efficiency with a large bandwidth. In the design, the radiation efficiency is optimised through the use of two distant coupling apertures that minimise surface-wave losses and significantly enlarge the bandwidth of the antenna. To improve the front-to-back ratio, a reflector element is introduced. These two design strategies are combined for the first time, to enhance the global efficiency and bandwidth of the antenna. The performance of the antenna design is verified through measurements that reported a bandwidth 15% and an antenna gain of 5.6 dBi.

- An efficient method-of-moment based model is derived in Chapter 3 for the analysis of the BFACP antenna. Both sub-domain and entire-domain basis functions are used to obtain a model with a limited number of unknowns. This reduces the computational effort that is needed to analyse the performance of the antenna. Moreover, the model is extended such that it can be used for the analysis of the antenna in array configurations as well (Chapter 6).

- In Chapter 4, a measurement setup is developed for the accurate characterisation of the scattering parameters of millimeter-wave antennas. To obtain a reliable interconnection, RF probes are used to connect to the antenna under test (AUT). To support the use of these probes, specific transitions have been developed, viz, a transition from coplanar waveguide (CPW) to microstrip (MS) and a transition from microstrip to coplanar microstrip (CPS).

- To characterise the radiation of millimeter wave antennas, a far-field radiation pattern measurement setup is designed in Chapter 4 as well. This setup is tailored for the measurement of the radiation pattern of millimeter-wave antennas and beam-forming antenna arrays. It is designed to minimise scattering from the measurement setup itself and it supports the use of RF probes for the interconnection with the AUT.

- To investigate the effect of manufacturing tolerances on antenna performance, a sensitivity analysis method is proposed in Chapter 5. This method is generalised for application to a wide class of EM problems. The sensitivity analysis is employed to optimise the performance of the antenna element as well. It is shown that the proposed optimisation algorithm is very efficient, since it is able to obtain an optimal antenna design within few iterations.

- The performance of beam-forming antenna arrays is investigated in Chapter 6. A circular-array topology is proposed that fulfills the gain requirements, has low mutual coupling and a high radiation efficiency for a wide scan range. The performance of the array is validated through the realisation of several prototypes that demonstrate beam-forming for specific scan angles.

- The complete transceiver has to be integrated into a single package that combines the active electronics, RF feed network, antenna array and control circuitry. The requirements on such a package are investigated and several topologies are discussed in Chapter 7. A specific package is proposed that embeds the BFACP antenna and integrates this antenna with a CMOS power amplifier. This package combines ceramic-based layers and teflon-based layers. The ceramic-based layers provide the package with stiffness and are used to realise the RF feed network, whereas the teflon-based layers are employed to allow an antenna design that has a high radiation efficiency.

# Electromagnetic modelling

## 2.1 Introduction

The modelling of electromagnetic problems is an extensive field of research. Many different methods have been proposed to model the EM fields for all kind of problems. Obviously, each method has its advantages and disadvantages. Some methods are more generally applicable, but computationally intensive, while other methods are computationally efficient, but only applicable to specific problems. In this chapter, a method is presented that is tailored to the analysis and design of millimeter-wave antennas that are realised in planar technology. Although a wide class of antennas can be analysed with the presented method, the knowledge about the technology choice is exploited to obtain a computationally efficient modelling method.

In planar technology, multiple material layers are stacked to create a multi-layered topology. Embedded metal traces define the antenna structures as well as other structures such as RF feed, vias and signal traces. An important approximation that is made in the modelling of this multi-layered stack is the assumption that the material layers extend to infinity in the lateral dimensions. Green's functions of this extended layered (or stratified) medium can be determined that describe the fields resulting from a point source that is located in the medium. With the help of Green's functions, integral equations can be formulated that describe the EM problem under consideration. The integral equations are expressed in terms of unknown surface-current densities. To solve these surface-current densities, the integral equations are

discretised to obtain a set of linear equations, following a method-of-moments (MoM) approach [16]. With the MoM only the surface-current densities are discretised and there is no need to discretise the fields in the background medium. Therefore, the number of unknowns remains limited such that the method can be computationally efficient.

To derive the Green's function, some knowledge is required about Maxwell's equations (see Section 2.2) and about vector potentials (see Section 2.3). Green's functions for a stratified medium are presented in Section 2.4. This work is based on [17, 18, 19]. The MoM is introduced in Section 2.5. Here, the discretisation of the integral equations is represented in matrix notation. These matrix elements are analysed in Section 2.6.

An important aspect of planar antenna structures is the presence of surface waves. Surface waves propagate in the layered medium and are discussed in Section 2.7. Obviously, the radiation of planar antennas is also very important. Therefore, the derivation of the radiation pattern of planar antennas is described in Section 2.8. The excitation of the EM structures is discussed in Section 2.9. To clarify the presented theory, an example is given in Section 2.10 in which a planar microstrip dipole is analysed. The modelling method that in presented is this chapter will be used throughout the thesis for planar antenna design and optimisation. In parallel, commercial tools are used as well. A comparison between these tools and the derived model is presented in Section 2.11.

## 2.2   Maxwell's equations and the constitutive relations

The relationship between the electromagnetic field and their electric and magnetic sources are given by Maxwell's equations. For continuously differentiable fields, these equations can be written in differential form as

$$
\begin{aligned}
\nabla \times \boldsymbol{\mathcal{H}}(\mathbf{r}, t) &= \frac{\partial \boldsymbol{\mathcal{D}}(\mathbf{r}, t)}{\partial t} + \boldsymbol{\mathcal{J}}(\mathbf{r}, t), \\
\nabla \times \boldsymbol{\mathcal{E}}(\mathbf{r}, t) &= -\frac{\partial \boldsymbol{\mathcal{B}}(\mathbf{r}, t)}{\partial t} - \boldsymbol{\mathcal{M}}(\mathbf{r}, t), \\
\nabla \cdot \boldsymbol{\mathcal{B}}(\mathbf{r}, t) &= \varrho_m(\mathbf{r}, t), \\
\nabla \cdot \boldsymbol{\mathcal{D}}(\mathbf{r}, t) &= \varrho_s(\mathbf{r}, t).
\end{aligned}
\tag{2.1}
$$

Here, $\boldsymbol{\mathcal{E}}(\mathbf{r}, t)$ is the electric-field strength, $\boldsymbol{\mathcal{H}}(\mathbf{r}, t)$ is the magnetic-field strength, $\boldsymbol{\mathcal{D}}(\mathbf{r}, t)$ is the electric-flux density, $\boldsymbol{\mathcal{B}}(\mathbf{r}, t)$ is the magnetic-flux density, $\boldsymbol{\mathcal{J}}(\mathbf{r}, t)$ is the electric-current density, $\boldsymbol{\mathcal{M}}(\mathbf{r}, t)$ is the magnetic-current density, $\varrho_s(\mathbf{r}, t)$ is the electric-charge density and $\varrho_m(\mathbf{r}, t)$ is the magnetic-charge density. The position vector is denoted as $\mathbf{r}$ and the time variable is denoted as $t$.

From the conservation of charge, two additional equations can be formed; the electric-source continuity equation and the magnetic-source continuity equation, viz,

$$\nabla \cdot \boldsymbol{J}(\mathbf{r},t) + \frac{\partial \varrho_s(\mathbf{r},t)}{\partial t} = 0,$$
$$\nabla \cdot \boldsymbol{\mathcal{M}}(\mathbf{r},t) + \frac{\partial \varrho_m(\mathbf{r},t)}{\partial t} = 0. \tag{2.2}$$

Harmonic time dependence is assumed for the field and source terms. Therefore a scalar term $\varrho(\mathbf{r},t)$ is written as

$$\varrho(\mathbf{r},t) = \mathsf{Re}\{\rho(\mathbf{r})e^{j\omega t}\}, \tag{2.3}$$

and a vector term $\boldsymbol{\mathcal{E}}(\mathbf{r},t)$ is written as

$$\boldsymbol{\mathcal{E}}(\mathbf{r},t) = \mathsf{Re}\{\mathbf{E}(\mathbf{r})e^{j\omega t}\}, \tag{2.4}$$

where $\omega$ is the angular frequency. Once harmonic time dependence is assumed, Maxwell's equations (2.1) can be written in a slightly simplified form as

$$\nabla \times \mathbf{H}(\mathbf{r}) = j\omega \mathbf{D}(\mathbf{r}) + \mathbf{J}(\mathbf{r}),$$
$$\nabla \times \mathbf{E}(\mathbf{r}) = -j\omega \mathbf{B}(\mathbf{r}) - \mathbf{M}(\mathbf{r}),$$
$$\nabla \cdot \mathbf{B}(\mathbf{r}) = \rho_m(\mathbf{r}),$$
$$\nabla \cdot \mathbf{D}(\mathbf{r}) = \rho_s(\mathbf{r}). \tag{2.5}$$

Here, the harmonic time dependence $e^{j\omega t}$ of the source and the fields is omitted. The continuity equations (2.2) are now given as

$$\nabla \cdot \mathbf{J}(\mathbf{r}) + j\omega \rho_s(\mathbf{r}) = 0,$$
$$\nabla \cdot \mathbf{M}(\mathbf{r}) + j\omega \rho_m(\mathbf{r}) = 0. \tag{2.6}$$

## 2.2.1 Constitutive relations

To complete the formulations for the electromagnetic field, constitutive relations have to be specified. The constitutive relations describe the interaction of the medium with the electromagnetic field. For a linearly reacting, homogeneous and isotropic medium, the constitutive relations result in a linear relation between $\mathbf{E}$, $\mathbf{D}$ and $\mathbf{H}$, $\mathbf{B}$, viz,

$$\mathbf{D}(\mathbf{r}) = \varepsilon \mathbf{E}(\mathbf{r}),$$
$$\mathbf{B}(\mathbf{r}) = \mu \mathbf{H}(\mathbf{r}). \tag{2.7}$$

Here $\varepsilon$ is the permittivity of the medium and $\mu$ is the permeability of the medium. In general, these parameters are written as

$$\varepsilon = \varepsilon_0 \varepsilon_r,$$
$$\mu = \mu_0 \mu_r, \tag{2.8}$$

where $\varepsilon_0$ is the permittivity of free space, $\varepsilon_r$ is the relative permittivity of the medium, $\mu_0$ is the permeability of free space and $\mu_r$ is the relative permeability of the medium. The relative permittivity $\varepsilon_r$ and the relative permeability $\mu_r$ are dependent on the medium.

The electric-current and magnetic-current densities can be written as the sum of a primary and secondary current density [20, Chapt. 2]. The primary current density is not influenced by the EM field, i.e., it is impressed, whereas the secondary current density represents the interaction of the medium with the electromagnetic field. In a conducting medium, an additional constitutive relation can be used to describe the interaction between the electric field and the secondary electric-current density $\mathbf{J}^{\mathrm{sec}}$, viz,

$$\mathbf{J}^{\mathrm{sec}}(\mathbf{r}) = \sigma \mathbf{E}(\mathbf{r}), \tag{2.9}$$

where $\sigma$ is the conductivity of the medium.

## 2.2.2   Boundary conditions

At the boundary between two different media, the fields and the sources at the boundary are related through the boundary conditions. The boundary conditions are (see e.g. [20, Chapt. 2])

$$\begin{aligned}
\mathbf{n} \times (\mathbf{H}_2(\mathbf{r}) - \mathbf{H}_1(\mathbf{r})) &= \mathbf{J}_s(\mathbf{r}), \\
\mathbf{n} \times (\mathbf{E}_2(\mathbf{r}) - \mathbf{E}_1(\mathbf{r})) &= -\mathbf{M}_s(\mathbf{r}), \\
\mathbf{n} \cdot (\mathbf{D}_2(\mathbf{r}) - \mathbf{D}_1(\mathbf{r})) &= \rho_s(\mathbf{r}), \\
\mathbf{n} \cdot (\mathbf{B}_2(\mathbf{r}) - \mathbf{B}_1(\mathbf{r})) &= \rho_m(\mathbf{r}).
\end{aligned} \tag{2.10}$$

Here, the subscripts 1, 2 denote the two separate media, $\mathbf{n}$ is a normal vector pointing from medium 1 into medium 2, and $\mathbf{J}_s$, $\mathbf{M}_s$ are electric and magnetic surface-current densities that are flowing along the boundary between the two media, i.e., orthogonal to the normal vector.

For penetrable media, i.e., $\varepsilon_r$, $\mu_r$ and $\sigma$ are finite in both regions, no secondary electric-current and magnetic-current densities are present. Consequently, when no primary electric-current and magnetic-current densities are impressed at the boundary, the boundary conditions (2.10) can be written as

$$\begin{aligned}
\mathbf{n} \times (\mathbf{H}_2(\mathbf{r}) - \mathbf{H}_1(\mathbf{r})) &= \mathbf{0}, \\
\mathbf{n} \times (\mathbf{E}_2(\mathbf{r}) - \mathbf{E}_1(\mathbf{r})) &= \mathbf{0}, \\
\mathbf{n} \cdot (\mathbf{D}_2(\mathbf{r}) - \mathbf{D}_1(\mathbf{r})) &= \rho_s(\mathbf{r}), \\
\mathbf{n} \cdot (\mathbf{B}_2(\mathbf{r}) - \mathbf{B}_1(\mathbf{r})) &= \rho_m(\mathbf{r}).
\end{aligned} \tag{2.11}$$

In a medium that is a perfect electric conductor (PEC), no fields are present inside the medium and the tangential electric field at the boundary is zero. Now, consider

that medium 1 is a PEC and medium 2 is a penetrable medium. In this case, the boundary conditions can be obtained from (2.6), (2.10) as

$$
\begin{aligned}
\mathbf{n} \times \mathbf{H}_2(\mathbf{r}) &= \mathbf{J}_s, \\
\mathbf{n} \times \mathbf{E}_2(\mathbf{r}) &= \mathbf{0}, \\
\mathbf{n} \cdot \mathbf{D}_2(\mathbf{r}) &= \rho_s(\mathbf{r}), \\
\mathbf{n} \cdot \mathbf{B}_2(\mathbf{r}) &= 0.
\end{aligned}
\tag{2.12}
$$

## 2.3  Vector potentials

The electric and magnetic field in a homogeneous, isotropic medium can be written in terms of the electric vector potential $\mathbf{F}$ and the magnetic vector potential $\mathbf{A}$ [20, Chapt. 5]. This relation is given as

$$
\begin{aligned}
\mathbf{E}(\mathbf{r}) &= -\frac{j\omega}{k^2}\Big[k^2 + \nabla\nabla\cdot\Big]\mathbf{A}(\mathbf{r}) - \frac{1}{\varepsilon}\nabla \times \mathbf{F}(\mathbf{r}), \\
\mathbf{H}(\mathbf{r}) &= -\frac{j\omega}{k^2}\Big[k^2 + \nabla\nabla\cdot\Big]\mathbf{F}(\mathbf{r}) + \frac{1}{\mu}\nabla \times \mathbf{A}(\mathbf{r}),
\end{aligned}
\tag{2.13}
$$

where $k = \omega\sqrt{\mu\varepsilon}$ is the propagation constant of the medium. To obtain (2.13), the Lorenz conditions have been employed [20, Chapt. 5]. The vector potentials must obey the Helmholtz equation, i.e.,

$$
\begin{aligned}
\left(k^2 + \nabla^2\right)\mathbf{A}(\mathbf{r}) &= -\mu\mathbf{J}(\mathbf{r}), \\
\left(k^2 + \nabla^2\right)\mathbf{F}(\mathbf{r}) &= -\varepsilon\mathbf{M}(\mathbf{r}).
\end{aligned}
\tag{2.14}
$$

The solutions to $\mathbf{A}$ and $\mathbf{F}$ are often determined using the accompanying dyadic Green's functions for the vector potentials, viz,

$$
\begin{aligned}
\mathbf{A}(\mathbf{r}) &= \int_{V'} \left[\underline{\underline{\mathbf{G}}}^{AJ}(\mathbf{r},\mathbf{r}') \cdot \mathbf{J}(\mathbf{r}') + \underline{\underline{\mathbf{G}}}^{AM}(\mathbf{r},\mathbf{r}') \cdot \mathbf{M}(\mathbf{r}')\right] dV', \\
\mathbf{F}(\mathbf{r}) &= \int_{V'} \left[\underline{\underline{\mathbf{G}}}^{FJ}(\mathbf{r},\mathbf{r}') \cdot \mathbf{J}(\mathbf{r}') + \underline{\underline{\mathbf{G}}}^{FM}(\mathbf{r},\mathbf{r}') \cdot \mathbf{M}(\mathbf{r}')\right] dV',
\end{aligned}
\tag{2.15}
$$

where a dyadic Green's function $\underline{\underline{\mathbf{G}}}^{PQ}$ describes the vector potential at $\mathbf{r}$ due to a point source that is located at $\mathbf{r}'$. The superscript $PQ$ denotes the appropriate Green's function, i.e., $P \in \{A, F\}$ relates to the magnetic or electric vector potential $(\mathbf{A}, \mathbf{F})$ and $Q \in \{J, M\}$ relates to the electric or magnetic current-density source $(\mathbf{J}, \mathbf{M})$.

To obtain a more compact notation, the fields are expressed as

$$
\begin{aligned}
\mathbf{E}(\mathbf{r}) &= \mathbb{L}\{\mathbf{J}, \mathbf{M}\}(\mathbf{r}), \\
\mathbf{H}(\mathbf{r}) &= \mathbb{K}\{\mathbf{J}, \mathbf{M}\}(\mathbf{r}),
\end{aligned}
\tag{2.16}
$$

where the operators $\mathbb{L}$, $\mathbb{K}$ are obtained from (2.13), (2.15) as

$$
\begin{aligned}
\mathbb{L}\{\mathbf{J}, \mathbf{M}\}(\mathbf{r}) &= -\frac{j\omega}{k^2}\Big[k^2 + \nabla\nabla\cdot\Big]\mathbf{A}(\mathbf{r}) - \frac{1}{\varepsilon}\nabla\times\mathbf{F}(\mathbf{r}), \\
\mathbb{K}\{\mathbf{J}, \mathbf{M}\}(\mathbf{r}) &= -\frac{j\omega}{k^2}\Big[k^2 + \nabla\nabla\cdot\Big]\mathbf{F}(\mathbf{r}) + \frac{1}{\mu}\nabla\times\mathbf{A}(\mathbf{r}).
\end{aligned}
\tag{2.17}
$$

## 2.4    Green's functions for stratified media

A Green's function relates the electric or magnetic field to an electric or magnetic point source. A Green's function depends on the medium in which the source is embedded. Once a Green's function is known, more complex sources can be analysed as well. In this section, all required Green's functions for stratified media are derived.

The geometry of a stratified medium is shown in Fig. 2.1. It consists of $N_l$ layers that extend to infinity in the lateral direction. Moreover, it is assumed that the top layer extends to infinity in the direction of stratification as well. Each layer $n$ has accompanying material properties like relative permittivity $\varepsilon_r^n$ and relative permeability $\mu_r^n$. The relative permittivity and permeability can be complex and therefore it is possible to account for dielectric losses in the stratification. In the presented derivation, it is assumed that the bottom layer is grounded with a perfect electric conductor (PEC). It is straightforward to apply other boundary conditions, but this setup is suited to the antenna problems that will be discussed in the remainder of this thesis. In the following derivation, Green's functions are obtained for this stratified medium where the stratification is assumed to be in the $z$-direction.

### 2.4.1    Hertz-Debye potentials

The fields in the stratification can be written in terms of the electric vector potential $\mathbf{F}$ and the magnetic vector potential $\mathbf{A}$, as shown in Section 2.3. To describe the electric and magnetic fields, not all 6 scalar components of the $\mathbf{A}$ and $\mathbf{F}$ vector potentials are required. In a source-free region, two scalar components are sufficient for the unique description of the fields [17], [21]. Therefore, several choices are possible and these result in different formulations for the vector potentials [19], [22]. A particular choice, that will be followed here, is to use Hertz-Debye potentials[1], where the $z$ component of both potentials are chosen to describe the fields, i.e., $\mathbf{A}(\mathbf{r}) = A_z(\mathbf{r})\mathbf{u}_z$ and $\mathbf{F}(\mathbf{r}) = F_z(\mathbf{r})\mathbf{u}_z$. As a result, only the $zx$, $zy$ and $zz$ components of the Green's

---

[1]Another popular choice is to use Sommerfeld potentials, where $\mathbf{F} = \mathbf{0}$ and only components of $\mathbf{A}$ are selected (see also [19]).
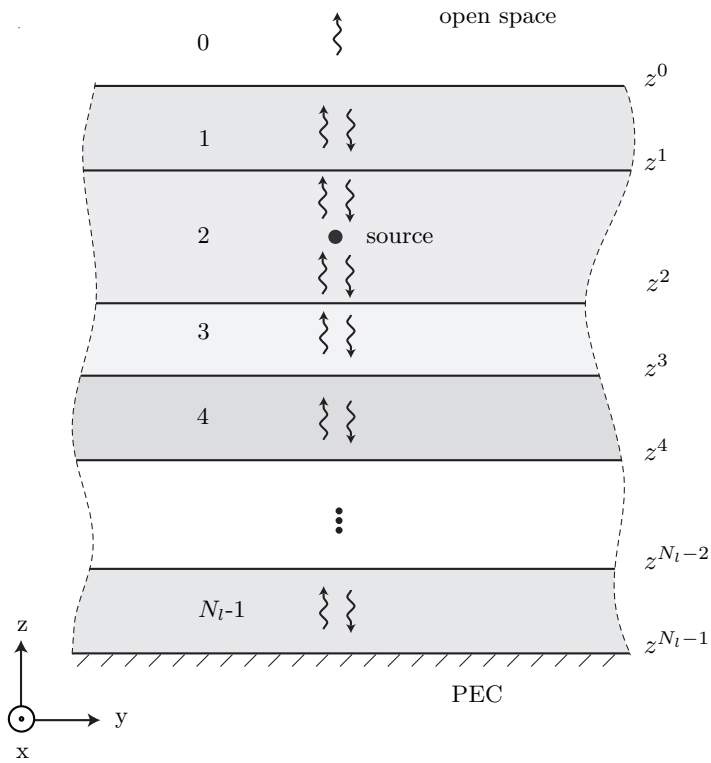
Figure 2.1: Layout of a stratified medium

dyadic have to be determined, i.e.,

$$\underline{\underline{\mathbf{G}}}^{PQ}(\mathbf{r}, \mathbf{r}') = \begin{bmatrix} 0 & 0 & 0 \\ 0 & 0 & 0 \\ G_{zx}^{PQ}(\mathbf{r}, \mathbf{r}') & G_{zy}^{PQ}(\mathbf{r}, \mathbf{r}') & G_{zz}^{PQ}(\mathbf{r}, \mathbf{r}') \end{bmatrix}. \tag{2.18}$$

### 2.4.2   Helmholtz equation in the spectral-domain

Now, consider a *point source* in a homogeneous medium (i.e., one layer of the stratified medium) that is located at $\mathbf{r}_s$. Outside the source region, the Helmholtz equations (2.14) in this homogeneous medium can be written as

$$\begin{aligned} \left(k^2 + \nabla^2\right) G_{zi}^{AQ}(\mathbf{r}|\mathbf{r}_s) &= 0, \\ \left(k^2 + \nabla^2\right) G_{zi}^{FQ}(\mathbf{r}|\mathbf{r}_s) &= 0, \end{aligned} \tag{2.19}$$

where $i \in \{x, y, z\}$ is determined by the orientation of the source. When this equation can be solved for the Green's functions of the magnetic and electric vector potential in the stratified medium, the fields can be described uniquely through (2.13) and (2.15). In the spatial domain, it is not possible to find a closed-form solution for (2.19) in a stratified medium. However, when the problem is transformed to the spectral domain in the $x$-$y$ plane, an analytical expression for the Green's function of the vector potentials can be found. The Fourier transformation that is used for the mapping from the spatial domain to the spectral domain and vice versa is defined as

$$\hat{\varphi}(k_x, k_y, z) = \int\limits_{-\infty}^{\infty} \int\limits_{-\infty}^{\infty} \varphi(x, y, z) e^{jk_x x + jk_y y} dx dy,$$

$$\varphi(x, y, z) = \frac{1}{4\pi^2} \int\limits_{-\infty}^{\infty} \int\limits_{-\infty}^{\infty} \hat{\varphi}(k_x, k_y, z) e^{-jk_x x - jk_y y} dk_x dk_y. \tag{2.20}$$

With the use of the Fourier transformation, (2.19) can be written in the spectral domain as

$$\begin{aligned} \left[k_z^2 + \partial_z^2\right] \hat{G}_{zi}^{AQ}(k_x, k_y, z|\mathbf{r}_s) &= 0, \\ \left[k_z^2 + \partial_z^2\right] \hat{G}_{zi}^{FQ}(k_x, k_y, z|\mathbf{r}_s) &= 0, \end{aligned} \tag{2.21}$$

where $k_z = \sqrt{k^2 - k_\rho^2}$ and $k_\rho = \sqrt{k_x^2 + k_y^2}$. Note that the use of the Fourier transformation allows us to write the set of partial differential equations (2.19) as a set of ordinary differential equations.

To solve the Green's function in the homogeneous layer that contains the point source, the layer is divided in two separate source-free regions. One region is defined above the point source and the other region is defined below the source. The homogeneous

solution of (2.21) for a point source that is located in layer $n = n_s$ for $z_s < z < z^{n_s-1}$ can be written as

$$
\begin{aligned}
\hat{G}_{zi,u}^{AQ,n_s}(k_x, k_y, z|\mathbf{r}_s) &= K_{A,u}^{n_s}\Big[e^{-jk_z^{n_s}(z-z_s)} + \Gamma_{A,u}^{n_s}e^{jk_z^{n_s}(z-z_s)}\Big]e^{jk_x x_s + jk_y y_s}, \\
\hat{G}_{zi,u}^{FQ,n_s}(k_x, k_y, z|\mathbf{r}_s) &= K_{F,u}^{n_s}\Big[e^{-jk_z^{n_s}(z-z_s)} + \Gamma_{F,u}^{n_s}e^{jk_z^{n_s}(z-z_s)}\Big]e^{jk_x x_s + jk_y y_s},
\end{aligned}
\tag{2.22}
$$

and for $z^{n_s} < z < z_s$ as

$$
\begin{aligned}
\hat{G}_{zi,d}^{AQ,n_s}(k_x, k_y, z|\mathbf{r}_s) &= K_{A,d}^{n_s}\Big[e^{jk_z^{n_s}(z-z_s)} + \Gamma_{A,d}^{n_s}e^{-jk_z^{n_s}(z-z_s)}\Big]e^{jk_x x_s + jk_y y_s}, \\
\hat{G}_{zi,d}^{FQ,n_s}(k_x, k_y, z|\mathbf{r}_s) &= K_{F,d}^{n_s}\Big[e^{jk_z^{n_s}(z-z_s)} + \Gamma_{F,d}^{n_s}e^{-jk_z^{n_s}(z-z_s)}\Big]e^{jk_x x_s + jk_y y_s},
\end{aligned}
\tag{2.23}
$$

where the subscripts $u, d$ represent the region of interest, i.e., $u$ represents the region above the source (up), and $d$ represents the region below the source (down). In (2.22), (2.23) amplitude coefficients $K_{A,u}^{n_s}$, $K_{F,u}^{n_s}$, $K_{A,d}^{n_s}$, $K_{F,d}^{n_s}$ and reflection coefficients $\Gamma_{A,u}^{n_s}$, $\Gamma_{F,u}^{n_s}$, $\Gamma_{A,d}^{n_s}$, $\Gamma_{F,d}^{n_s}$ have been introduced. Note that the dependency of the amplitude and reflection coefficients on $k_x, k_y, z, z_s$ has been omitted. Each of these solutions can be interpreted as the summation of two waves. One wave that is moving away from the point source and one wave that is reflected at the boundary of the stratification and that is moving towards the source.

### 2.4.3 Amplitude and reflection coefficients

The amplitude coefficients can be found from the boundary conditions at the source location. These terms depend on the source type, i.e., electric or magnetic, and on the orientation of the source. The reflection coefficients can be obtained from the boundary conditions at the edges of the separate layers. The derivation of these coefficients is demonstrated for an $x$-oriented electric point source. The coefficients for different orientations and other source types can be found in Appendix A. The amplitude coefficients will be discussed first, hereafter the reflection coefficients are considered.

Consider an $x$-oriented electric point source that is located at $\mathbf{r}_s = \{x_s, y_s, z_s\}$,

$$
\mathbf{J}(\mathbf{r}) = \delta(x - x_s)\delta(y - y_s)\delta(z - z_s)\mathbf{u}_x.
\tag{2.24}
$$

The boundary conditions (2.10) for this point source can be written in the spectral domain as

$$
\begin{aligned}
\mathbf{n} \times (\hat{\mathbf{H}}^u(k_x, k_y, z) - \hat{\mathbf{H}}^d(k_x, k_y, z)) &= \delta(z - z_s)e^{jk_x x_s + jk_y y_s}\mathbf{u}_x, \\
\mathbf{n} \times (\hat{\mathbf{E}}^u(k_x, k_y, z) - \hat{\mathbf{E}}^d(k_x, k_y, z)) &= 0,
\end{aligned}
\tag{2.25}
$$

where the fields $\hat{\mathbf{E}}$, $\hat{\mathbf{H}}$ in the spectral domain can be obtained from (2.13) as

$$
\begin{aligned}
\hat{E}_x(k_x, k_y, z) &= -\frac{\omega k_x}{k^2}\partial_z \hat{A}_z(k_x, k_y, z) - \frac{jk_y}{\varepsilon}\hat{F}_z(k_x, k_y, z), \\
\hat{E}_y(k_x, k_y, z) &= -\frac{\omega k_y}{k^2}\partial_z \hat{A}_z(k_x, k_y, z) + \frac{jk_x}{\varepsilon}\hat{F}_z(k_x, k_y, z), \\
\hat{E}_z(k_x, k_y, z) &= -j\omega \hat{A}_z(k_x, k_y, z) - \frac{j\omega}{k^2}\partial_z^2 \hat{A}_z(k_x, k_y, z), \\
\hat{H}_x(k_x, k_y, z) &= -\frac{\omega k_x}{k^2}\partial_z \hat{F}_z(k_x, k_y, z) + \frac{jk_y}{\mu}\hat{A}_z(k_x, k_y, z), \\
\hat{H}_y(k_x, k_y, z) &= -\frac{\omega k_y}{k^2}\partial_z \hat{F}_z(k_x, k_y, z) - \frac{jk_x}{\mu}\hat{A}_z(k_x, k_y, z), \\
\hat{H}_z(k_x, k_y, z) &= -j\omega \hat{F}_z(k_x, k_y, z) - \frac{j\omega}{k^2}\partial_z^2 \hat{F}_z(k_x, k_y, z).
\end{aligned}
\tag{2.26}
$$

Substitution of (2.26) in the boundary conditions (2.25) and the use of (2.22), (2.23) allow us to solve the amplitude coefficients of the Green's functions $\hat{G}_{zx}^{AJ,n_s}$ and $\hat{G}_{zx}^{FJ,n_s}$, i.e.,

$$
\begin{aligned}
K_{A,u}^{n_s} &= \frac{jk_x\mu^{n_s}(1 - \Gamma_{A,d}^{n_s})}{2k_\rho^2(1 - \Gamma_{A,u}^{n_s}\Gamma_{A,d}^{n_s})}, \\
K_{F,u}^{n_s} &= \frac{jk_y\omega\mu^{n_s}\varepsilon^{n_s}(1 + \Gamma_{F,d}^{n_s})}{2k_z^{n_s}k_\rho^2(1 - \Gamma_{F,u}^{n_s}\Gamma_{F,d}^{n_s})}, \\
K_{A,d}^{n_s} &= -\frac{jk_x\mu^{n_s}(1 - \Gamma_{A,u}^{n_s})}{2k_\rho^2(1 - \Gamma_{A,u}^{n_s}\Gamma_{A,d}^{n_s})}, \\
K_{F,d}^{n_s} &= \frac{jk_y\omega\mu^{n_s}\varepsilon^{n_s}(1 + \Gamma_{F,u}^{n_s})}{2k_z^{n_s}k_\rho^2(1 - \Gamma_{F,u}^{n_s}\Gamma_{F,d}^{n_s})}.
\end{aligned}
\tag{2.27}
$$

Here, the superscript $n_s$ indicates the layer at which the coefficients should be determined. For different source orientations and magnetic point sources, similar expressions can be derived (see Appendix A.1).

The solution of (2.21) in a layer $n = n_u$ above the $x$-oriented electric point source can be written as

$$
\begin{aligned}
\hat{G}_{zx}^{AJ,n_u}(k_x, k_y, z|\mathbf{r}_s) &= K_A^{n_u}\left[e^{-jk_z^{n_u}(z-z^{n_u})} + \Gamma_A^{n_u}e^{jk_z^{n_u}(z-z^{n_u})}\right]e^{jk_x x_s + jk_y y_s}, \\
\hat{G}_{zx}^{FJ,n_u}(k_x, k_y, z|\mathbf{r}_s) &= K_F^{n_u}\left[e^{-jk_z^{n_u}(z-z^{n_u})} + \Gamma_F^{n_u}e^{jk_z^{n_u}(z-z^{n_u})}\right]e^{jk_x x_s + jk_y y_s}.
\end{aligned}
\tag{2.28}
$$

To obtain expressions for the reflection coefficients, the boundary conditions at the boundaries between the source layer and the neighbouring layers have to be considered. At the boundary of two layers, the tangential components of the electric and magnetic fields have to be continuous. This results in a relation between the reflection coefficients of neighbouring layers. For example, the reflection coefficients of the source layer can be expressed in terms of the reflection coefficients of the layer above

the source as

$$
\begin{aligned}
\Gamma_{A,u}^{n_s} &= \frac{k_z^{n_s}\varepsilon^{n_s-1}(1+\Gamma_A^{n_s-1}) - k_z^{n_s-1}\varepsilon^{n_s}(1-\Gamma_A^{n_s-1})}{k_z^{n_s}\varepsilon^{n_s-1}(1+\Gamma_A^{n_s-1}) + k_z^{n_s-1}\varepsilon^{n_s}(1-\Gamma_A^{n_s-1})} e^{-2jk_z^{n_s}(z^{n_s-1}-z_s)}, \\
\Gamma_{F,u}^{n_s} &= \frac{k_z^{n_s}\mu^{n_s-1}(1+\Gamma_F^{n_s-1}) - k_z^{n_s-1}\mu^{n_s}(1-\Gamma_F^{n_s-1})}{k_z^{n_s}\mu^{n_s-1}(1+\Gamma_F^{n_s-1}) + k_z^{n_s-1}\mu^{n_s}(1-\Gamma_F^{n_s-1})} e^{-2jk_z^{n_s}(z^{n_s-1}-z_s)}.
\end{aligned}
\tag{2.29}
$$

In a similar way, an expression can be found for the reflection coefficients below the source. It is observed that the reflection coefficient of the inner layers relate to the reflection coefficients of the outer layers. At the top layer, the reflection coefficients are zero, since it is assumed that this layer extends to infinity. At the bottom layer, PEC is assumed which forces the tangential electric field to zero. Therefore the reflection coefficient $\Gamma_A^{N-1} = 1$ and $\Gamma_F^{N-1} = -1$.

The continuity of the tangential electric and magnetic fields at the boundary relates the amplitude coefficient of neighbouring layers as well. For example, the amplitude coefficient of the layer above the source can be expressed in terms of the amplitude coefficient of the source layer as

$$
\begin{aligned}
K_A^{n_s-1} &= \frac{2K_{A,u}^{n_s} k_z^{n_s}\mu^{n_s-1}\varepsilon^{n_s-1}}{k_z^{n_s}\mu^{n_s}\varepsilon^{n_s-1}(1+\Gamma_A^{n_s-1}) + k_z^{n_s-1}\mu^{n_s}\varepsilon^{n_s}(1-\Gamma_A^{n_s-1})} e^{-jk_z^{n_s}(z^{n_s-1}-z_s)}, \\
K_F^{n_s-1} &= \frac{2K_{F,u}^{n_s} k_z^{n_s}\mu^{n_s-1}\varepsilon^{n_s-1}}{k_z^{n_s}\mu^{n_s-1}\varepsilon^{n_s}(1+\Gamma_A^{n_s-1}) + k_z^{n_s-1}\mu^{n_s}\varepsilon^{n_s}(1-\Gamma_A^{n_s-1})} e^{-jk_z^{n_s}(z^{n_s-1}-z_s)}.
\end{aligned}
\tag{2.30}
$$

Following this approach, relations can be found between the coefficients of neighbouring layers below and further away from the source. Once all these coefficients are determined, the fields resulting from a point source are known everywhere in the stratification.

## 2.5 Method of moments

The fields resulting from electric and magnetic point sources can be obtained from the Green's functions for stratified media. With the help of Green's functions, integral equations can be formulated that describe the electromagnetic behaviour of more complex sources and geometries embedded in a stratified medium. These integral equations are expressed in terms of unknown surface-current densities. To solve these surface-current densities, the integral equations are discretised to obtain a set of linear equations, following a MoM approach.

### 2.5.1   Surface equivalence principle

Consider a homogeneous object embedded in a stratified medium that also contains electric-current and magnetic-current densities $\mathbf{J}^{\mathrm{inc}}$, $\mathbf{M}^{\mathrm{inc}}$ (Fig. 2.2). According to the equivalence principle [20, Chapt. 6], an equivalent problem can be formulated for the fields outside the object (Fig. 2.3). In this formulation, equivalent electric and magnetic surface-current densities $\mathbf{J}^{\mathrm{eq}}$, $\mathbf{M}^{\mathrm{eq}}$ are introduced at the surface of the object. The equivalent surface-current densities are related to the original fields as [20, Chapt. 6]

$$\mathbf{J}^{\mathrm{eq}}(\mathbf{r}) = \mathbf{n} \times \mathbf{H}(\mathbf{r}),$$
$$\mathbf{M}^{\mathrm{eq}}(\mathbf{r}) = -\mathbf{n} \times \mathbf{E}(\mathbf{r}), \tag{2.31}$$

where the normal $\mathbf{n}$ points outwards from the object into the stratified medium. Inside the volume that is surrounded by the equivalent sources, the electric and magnetic fields are zero and therefore this volume can be filled with the original stratified medium without changing the fields outside the volume (Fig. 2.4). The resulting geometry is a stratified medium that contains electric and magnetic surface-current densities only and the Green's functions for the stratified medium (see Section 2.4) can be employed to analyse its electromagnetic behaviour outside the homogeneous object.

To obtain the fields inside the object, an equivalent problem can be formulated as well (Fig. 2.5). Note that the equivalent sources are still defined by (2.31), but the normal vector now points inwards from the stratified medium into the object. In this formulation, the fields are zero outside the volume that is surrounded by equivalent sources. Therefore it is possible to replace the stratified medium with the material of the enclosed object and the Green's functions for a homogenous medium can be employed to derive the fields resulting from the equivalent sources.

From the boundary conditions at the surface of the object, an electric-field integral equation (EFIE) and a magnetic-field integral equation (MFIE) can be obtained that relate the current densities $\mathbf{J}^{\mathrm{inc}}$ and $\mathbf{M}^{\mathrm{inc}}$ to the equivalent surface-current densities $\mathbf{J}^{\mathrm{eq}}$ and $\mathbf{M}^{\mathrm{eq}}$. This is explained further in the following sections.

### 2.5.2   Perfect electric conductor

When a perfect electric conductor (PEC) is embedded in the stratification, the boundary conditions at the surface force the tangential electric field to zero and the EFIE can be written as

$$\mathbf{n} \times \left[ \mathbf{E}^{\mathrm{inc}}(\mathbf{r}) + \mathbf{E}^{\mathrm{eq}}(\mathbf{r}) \right] = 0, \tag{2.32}$$

where the fields are evaluated at the boundary of the PEC. Since the tangential electric field at the boundary is zero, the equivalent sources consist of electric-current

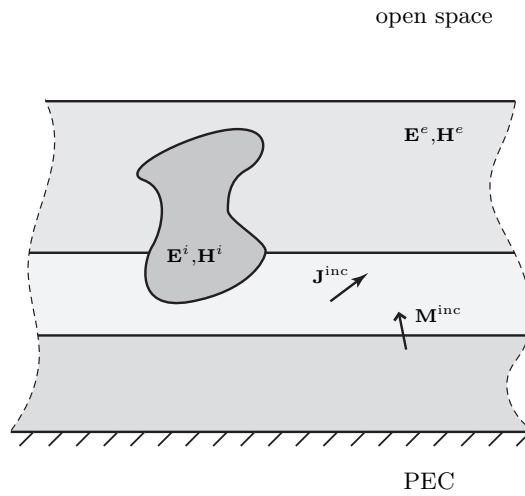open space



Figure 2.2: Layout of a stratified medium with embedded object and current sources.
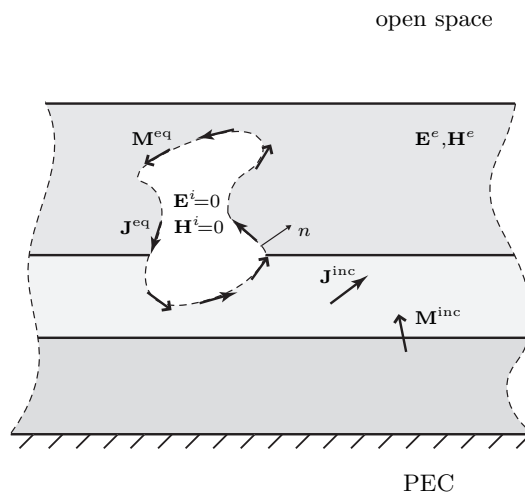
open space



Figure 2.3: Equivalent problem for the fields outside the object.
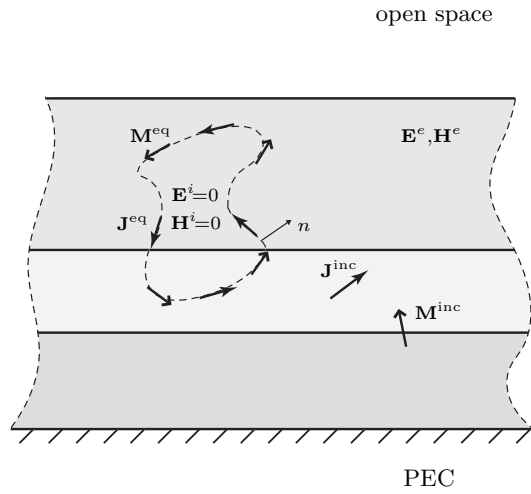
open space



Figure 2.4:  Equivalent problem for the fields outside the object and a stratified medium as geometry.
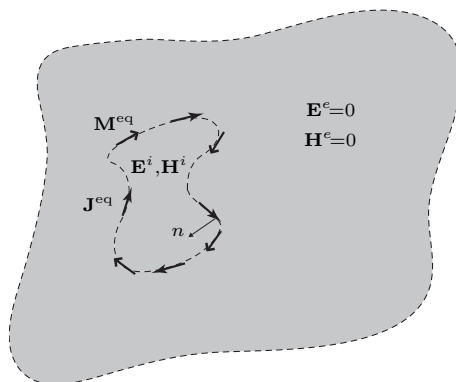


Figure 2.5: Equivalent problem for the fields inside the object embedded in a homogeneous medium.

densities only ($\mathbf{M}^{\text{eq}} = \mathbf{0}$). Using (2.16), this EFIE can therefore be written as[2]

$$\mathbf{n} \times \left[ \mathbf{E}^{\text{inc}}(\mathbf{r}) + \mathbb{L}\{\mathbf{J}^{\text{eq}}, \mathbf{0}\}(\mathbf{r}) \right] = 0. \tag{2.33}$$

To solve (2.33), the equivalent electric-current density is approximated as

$$\mathbf{J}^{\text{eq}}(\mathbf{r}) \approx \sum_{n=0}^{N_b-1} \kappa_n \mathbf{f}_n(\mathbf{r}), \tag{2.34}$$

where $\mathbf{f}_n$ is a basis function that is used to expand the equivalent current density, $\kappa_n$ is a complex amplitude that determines its contribution, and $N_b$ is the number of basis functions. The electric-current density is approximated with a finite set of basis functions and therefore a residue term $\mathbf{R}$ is introduced in (2.33) that accounts for the difference between the actual and the approximated current, viz,

$$\mathbf{n} \times \left[ \mathbf{E}^{\text{inc}}(\mathbf{r}) + \sum_{n=0}^{N_b-1} \kappa_n \mathbb{L}\{\mathbf{f}_n, \mathbf{0}\}(\mathbf{r}) \right] = \mathbf{n} \times \mathbf{R}(\mathbf{r}). \tag{2.35}$$

Ideally, the residue term is zero everywhere. However, this requires the exact solution of the current density and typically this is not feasible with a limited number of basis functions. Therefore, the residue term is weighed to zero, i.e., we enforce

$$\left\langle \mathbf{n} \times \mathbf{g}_m(\mathbf{r}), \mathbf{n} \times \mathbf{R}(\mathbf{r}) \right\rangle = 0. \tag{2.36}$$

Here, $\mathbf{g}_m$ is known as a test function and the inner product $\langle \cdot, \cdot \rangle$ is defined as

$$\left\langle \mathbf{a}(\mathbf{r}), \mathbf{b}(\mathbf{r}) \right\rangle = \int_{S_a} \mathbf{a}(\mathbf{r}) \cdot \mathbf{b}(\mathbf{r}) dS_a, \tag{2.37}$$

where $S_a$ is the support of $\mathbf{a}$. In (2.36), the right-hand side of (2.35) is weighed with $\mathbf{n} \times \mathbf{g}_m$ instead of $\mathbf{g}_m$ since this allows us to rewrite (2.36) as

$$\left\langle \mathbf{g}_m(\mathbf{r}), \mathbf{R}(\mathbf{r}) \right\rangle = 0, \tag{2.38}$$

under the assumption that $\mathbf{g}_m$ is tangential to the boundary of the PEC. Now, the weighed residue term in (2.38) can be expanded using (2.35) as

$$\left\langle \mathbf{g}_m(\mathbf{r}), \mathbf{E}^{\text{inc}}(\mathbf{r}) \right\rangle + \left\langle \mathbf{g}_m(\mathbf{r}), \sum_{n=0}^{N_b-1} \kappa_n \mathbb{L}\{\mathbf{f}_n, \mathbf{0}\}(\mathbf{r}) \right\rangle = 0. \tag{2.39}$$

To solve for all coefficients $\kappa_n$, (2.39) is tested with $N_b$ independent test functions, i.e.,

$$\left\langle \mathbf{g}_m(\mathbf{r}), \mathbf{E}^{\text{inc}}(\mathbf{r}) \right\rangle + \left\langle \mathbf{g}_m(\mathbf{r}), \sum_{n=0}^{N_b-1} \kappa_n \mathbb{L}\{\mathbf{f}_n, \mathbf{0}\}(\mathbf{r}) \right\rangle = 0 \quad \forall\, m \in \{0, \dots, N_b - 1\}. \tag{2.40}$$

---

[2]In (2.33), the argument of $\mathbb{L}$ is the surface-current density $\mathbf{J}^{\text{eq}}$. Strictly speaking, the operator $\mathbb{L}$ is defined for volume-current densities [see (2.17)]. However, overloading is admitted here since the definition of the operator $\mathbb{L}$ for surface-current densities is identical, except for the volume integrals in (2.15) that change to surface integrals.

In a more compact form, this can be written in matrix notation as

$$\mathtt{Z}\mathtt{I} = \mathtt{V}, \tag{2.41}$$

where the excitation vector $\mathtt{V}$ is a column vector that represents the sources in the electromagnetic problem and the interaction matrix $\mathtt{Z}$ measures the interaction between the expansion functions $\mathbf{f}$ and the test functions $\mathbf{g}$. The current vector $\mathtt{I}$ is a column vector that contains the coefficients $\kappa_n$, which define the complex amplitude of the expansion functions. The elements of the excitation vector and the interaction matrix are defined as

$$\begin{aligned}
\mathtt{V}_m &= -\Big\langle \mathbf{g}_m(\mathbf{r}), \mathbf{E}^{\mathrm{inc}}(\mathbf{r}) \Big\rangle, \\
\mathtt{Z}_{mn} &= \Big\langle \mathbf{g}_m(\mathbf{r}), \mathbb{L}\{\mathbf{f}_n, \mathbf{0}\}(\mathbf{r}) \Big\rangle.
\end{aligned} \tag{2.42}$$

The current vector is obtained from (2.41) as

$$\mathtt{I} = \mathtt{Z}^{-1}\mathtt{V}. \tag{2.43}$$

Once this current vector is known, an approximation of the equivalent electric-current density on the PEC is known as well and the (approximated) fields outside the object can be determined everywhere.

### 2.5.3  Dielectric object

In case a dielectric object is embedded in the stratification, both equivalent magnetic-current and electric-current densities are needed to derive an equivalent problem for the interior and exterior region. The fields in the interior and exterior regions can be represented as

$$\begin{aligned}
\mathbf{E}^e(\mathbf{r}) &= \mathbf{E}^{\mathrm{inc}}(\mathbf{r}) + \mathbb{L}^e\{\mathbf{J}^{\mathrm{eq},e}, \mathbf{M}^{\mathrm{eq},e}\}(\mathbf{r}), \\
\mathbf{H}^e(\mathbf{r}) &= \mathbf{H}^{\mathrm{inc}}(\mathbf{r}) + \mathbb{K}^e\{\mathbf{J}^{\mathrm{eq},e}, \mathbf{M}^{\mathrm{eq},e}\}(\mathbf{r}), \\
\mathbf{E}^i(\mathbf{r}) &= \mathbb{L}^i\{\mathbf{J}^{\mathrm{eq},i}, \mathbf{M}^{\mathrm{eq},i}\}(\mathbf{r}), \\
\mathbf{H}^i(\mathbf{r}) &= \mathbb{K}^i\{\mathbf{J}^{\mathrm{eq},i}, \mathbf{M}^{\mathrm{eq},i}\}(\mathbf{r}),
\end{aligned} \tag{2.44}$$

where the superscripts $e, i$ denote the exterior and interior region, respectively. The operators, $\mathbb{L}^e$, $\mathbb{K}^e$ relate the fields in the exterior region, i.e, the stratified medium, to the sources in the exterior region. The operators $\mathbb{L}^i$, $\mathbb{K}^i$ relate the field in the interior region, i.e., the homogeneous medium, to the sources in the interior region. At the boundary of the original problem, the tangential electric and magnetic fields should

be continuous. Therefore the EFIE and MFIE become

$$\mathbf{n} \times \left[ \mathbf{E}^{\mathrm{inc}}(\mathbf{r}_s) + \lim_{h \downarrow 0} \mathbb{L}^e \{ \mathbf{J}^{\mathrm{eq},e}, \mathbf{M}^{\mathrm{eq},e} \}(\mathbf{r}_s + h\mathbf{n}) \right]$$
$$= \mathbf{n} \times \left[ \lim_{h \downarrow 0} \mathbb{L}^i \{ \mathbf{J}^{\mathrm{eq},i}, \mathbf{M}^{\mathrm{eq},i} \}(\mathbf{r}_s - h\mathbf{n}) \right],$$
$$\mathbf{n} \times \left[ \mathbf{H}^{\mathrm{inc}}(\mathbf{r}_s) + \lim_{h \downarrow 0} \mathbb{K}^e \{ \mathbf{J}^{\mathrm{eq},e}, \mathbf{M}^{\mathrm{eq},e} \}(\mathbf{r}_s + h\mathbf{n}) \right]$$
$$= \mathbf{n} \times \left[ \lim_{h \downarrow 0} \mathbb{K}^i \{ \mathbf{J}^{\mathrm{eq},i}, \mathbf{M}^{\mathrm{eq},i} \}(\mathbf{r}_s - h\mathbf{n}) \right],$$

(2.45)

where $r_s$ is located on the boundary and $n$ is the normal vector pointing outwards from the interior region into the exterior region. The limit terms $\lim_{h \downarrow 0}$ are introduced since the fields cannot be evaluated directly at the boundary because in that case the observation point and the source point would coincide. However, the limit terms can be determined if a small spherical region that includes the source point is excluded from the surface integral over the equivalent surface-current density and integrated separately in the limit where the exclusion region vanishes [23]. Following this approach, the limit terms can be expressed as

$$\lim_{h \downarrow 0} \mathbb{L}^e \{ \mathbf{J}^{\mathrm{eq},e}, \mathbf{M}^{\mathrm{eq},e} \}(\mathbf{r}_s + h\mathbf{n}) = \mathbb{L}^e \{ \mathbf{J}^{\mathrm{eq},e}, \mathbf{M}^{\mathrm{eq},e} \}(\mathbf{r}_s) + \frac{\mathbf{E}^e(\mathbf{r}_s)}{2},$$
$$\lim_{h \downarrow 0} \mathbb{L}^i \{ \mathbf{J}^{\mathrm{eq},i}, \mathbf{M}^{\mathrm{eq},i} \}(\mathbf{r}_s - h\mathbf{n}) = \mathbb{L}^i \{ \mathbf{J}^{\mathrm{eq},i}, \mathbf{M}^{\mathrm{eq},i} \}(\mathbf{r}_s) + \frac{\mathbf{E}^i(\mathbf{r}_s)}{2},$$
$$\lim_{h \downarrow 0} \mathbb{K}^e \{ \mathbf{J}^{\mathrm{eq},e}, \mathbf{M}^{\mathrm{eq},e} \}(\mathbf{r}_s + h\mathbf{n}) = \mathbb{K}^e \{ \mathbf{J}^{\mathrm{eq},e}, \mathbf{M}^{\mathrm{eq},e} \}(\mathbf{r}_s) + \frac{\mathbf{H}^e(\mathbf{r}_s)}{2},$$
$$\lim_{h \downarrow 0} \mathbb{K}^i \{ \mathbf{J}^{\mathrm{eq},i}, \mathbf{M}^{\mathrm{eq},i} \}(\mathbf{r}_s - h\mathbf{n}) = \mathbb{K}^i \{ \mathbf{J}^{\mathrm{eq},i}, \mathbf{M}^{\mathrm{eq},i} \}(\mathbf{r}_s) + \frac{\mathbf{H}^i(\mathbf{r}_s)}{2}.$$

(2.46)

A relation between the equivalent sources of the interior and exterior region can be obtained from the continuity of the tangential fields at the boundary as well, i.e.,

$$\mathbf{J}^{\mathrm{eq}}(\mathbf{r}_s) = \mathbf{J}^{\mathrm{eq},e}(\mathbf{r}_s) \qquad = -\mathbf{J}^{\mathrm{eq},i}(\mathbf{r}_s),$$
$$\mathbf{M}^{\mathrm{eq}}(\mathbf{r}_s) = \mathbf{M}^{\mathrm{eq},e}(\mathbf{r}_s) \quad = -\mathbf{M}^{\mathrm{eq},i}(\mathbf{r}_s).$$

(2.47)

Combining (2.45), (2.46), and (2.47), the EFIE and MFIE can be expressed as

$$-\mathbf{n} \times \mathbf{E}^{\mathrm{inc}}(\mathbf{r}) = \mathbf{n} \times \left[ \mathbb{L}^i \{ \mathbf{J}^{\mathrm{eq}}, \mathbf{M}^{\mathrm{eq}} \}(\mathbf{r}) + \mathbb{L}^e \{ \mathbf{J}^{\mathrm{eq}}, \mathbf{M}^{\mathrm{eq}} \}(\mathbf{r}) \right],$$
$$-\mathbf{n} \times \mathbf{H}^{\mathrm{inc}}(\mathbf{r}) = \mathbf{n} \times \left[ \mathbb{K}^i \{ \mathbf{J}^{\mathrm{eq}}, \mathbf{M}^{\mathrm{eq}} \}(\mathbf{r}) + \mathbb{K}^e \{ \mathbf{J}^{\mathrm{eq}}, \mathbf{M}^{\mathrm{eq}} \}(\mathbf{r}) \right].$$

(2.48)

This formulation is known as the Poggio, Miller, Chang, Harrington, Wu (PMCHW) formulation [23]. Next, these integral equations are discretised to find the (approximated) equivalent surface-current densities. Following the same approach as in Section 2.5.2, the equivalent electric-current and magnetic-current densities are approx-

imated as

$$\mathbf{J}^{\mathrm{eq}}(\mathbf{r}) \approx \sum_{n=0}^{N_b-1} \kappa_n \mathbf{f}_n(\mathbf{r}),$$

$$\mathbf{M}^{\mathrm{eq}}(\mathbf{r}) \approx \sum_{n=0}^{N_b-1} \varsigma_n \mathbf{h}_n(\mathbf{r}), \tag{2.49}$$

and (2.48) is tested with testing functions $\mathbf{g}$ that are tangential to the boundary of the dielectric object. The resulting relation can be written in matrix notation as

$$\left[ \begin{array}{cc} \mathbf{Z}^{EJ} & \mathbf{Z}^{EM} \\ \mathbf{Z}^{HM} & \mathbf{Z}^{HM} \end{array} \right] \left[ \begin{array}{c} \mathbf{I}^J \\ \mathbf{I}^M \end{array} \right] = \left[ \begin{array}{c} \mathbf{V}^E \\ \mathbf{V}^H \end{array} \right] \tag{2.50}$$

where

$$\begin{aligned}
\mathbf{V}_m^E &= -\Big\langle \mathbf{g}_m(\mathbf{r}), \mathbf{E}^{\mathrm{inc}}(\mathbf{r}) \Big\rangle, \\
\mathbf{V}_m^H &= -\Big\langle \mathbf{g}_m(\mathbf{r}), \mathbf{H}^{\mathrm{inc}}(\mathbf{r}) \Big\rangle, \\
\mathbf{Z}_{mn}^{EJ} &= \Big\langle \mathbf{g}_m(\mathbf{r}), \mathbb{L}^i\{\mathbf{f}_n, \mathbf{0}\}(\mathbf{r}) \Big\rangle + \Big\langle \mathbf{g}_m(\mathbf{r}), \mathbb{L}^e\{\mathbf{f}_n, \mathbf{0}\}(\mathbf{r}) \Big\rangle, \\
\mathbf{Z}_{mn}^{EM} &= \Big\langle \mathbf{g}_m(\mathbf{r}), \mathbb{L}^i\{\mathbf{0}, \mathbf{h}_n\}(\mathbf{r}) \Big\rangle + \Big\langle \mathbf{g}_m(\mathbf{r}), \mathbb{L}^e\{\mathbf{0}, \mathbf{h}_n\}(\mathbf{r}) \Big\rangle, \\
\mathbf{Z}_{mn}^{HJ} &= \Big\langle \mathbf{g}_m(\mathbf{r}), \mathbb{K}^i\{\mathbf{f}_n, \mathbf{0}\}(\mathbf{r}) \Big\rangle + \Big\langle \mathbf{g}_m(\mathbf{r}), \mathbb{K}^e\{\mathbf{f}_n, \mathbf{0}\}(\mathbf{r}) \Big\rangle, \\
\mathbf{Z}_{mn}^{HM} &= \Big\langle \mathbf{g}_m(\mathbf{r}), \mathbb{K}^i\{\mathbf{0}, \mathbf{h}_n\}(\mathbf{r}) \Big\rangle + \Big\langle \mathbf{g}_m(\mathbf{r}), \mathbb{K}^e\{\mathbf{0}, \mathbf{h}_n\}(\mathbf{r}) \Big\rangle.
\end{aligned} \tag{2.51}$$

## 2.6 Evaluation of the matrix elements

The evaluation of the matrix elements that are introduced in the method of moments (see Section 2.5) can be a complicated task. Each matrix element requires the evaluation of two nested surface integrals over the domain of the expansion function and the test function. Moreover, to obtain the Green's functions, an inverse Fourier transform has to be computed for each combination of source and observation point as well. For well-defined basis functions, part of the required integral evaluations can be performed analytically. This feature is employed in the spectral-domain representation that is clarified in this section.

### 2.6.1 Spectral-domain representation

Consider a matrix element that is related to an expansion function which represents an electric-current density. This matrix element is defined as [see (2.42)]

$$\mathbf{Z}_{mn} = \Big\langle \mathbf{g}_m(\mathbf{r}), \mathbb{L}\{\mathbf{f}_n, \mathbf{0}\}(\mathbf{r}) \Big\rangle, \tag{2.52}$$

where the $\mathbb{L}$ operator is defined as [see (2.17)]

$$\mathbb{L}\{\mathbf{f}_n, \mathbf{0}\}(\mathbf{r}) = -\frac{j\omega}{k^2}\left[k^2 + \nabla\nabla\cdot\right]\mathbf{A}(\mathbf{r}) - \frac{1}{\varepsilon}\nabla \times \mathbf{F}(\mathbf{r}), \qquad (2.53)$$

with

$$\mathbf{A}(\mathbf{r}) = \int\limits_{S'} \underline{\underline{\mathbf{G}}}^{AJ}(\mathbf{r}, \mathbf{r}') \cdot \mathbf{f}_n(\mathbf{r}') \quad dS',$$

$$\mathbf{F}(\mathbf{r}) = \int\limits_{S'} \underline{\underline{\mathbf{G}}}^{FJ}(\mathbf{r}, \mathbf{r}') \cdot \mathbf{f}_n(\mathbf{r}') \quad dS', \qquad (2.54)$$

and

$$\underline{\underline{\mathbf{G}}}^{PQ}(\mathbf{r}, \mathbf{r}') = \frac{1}{4\pi^2} \int\limits_{-\infty}^{\infty}\int\limits_{-\infty}^{\infty} \underline{\underline{\hat{\mathbf{G}}}}^{PQ}(k_x, k_y, z, \mathbf{r}')e^{-jk_x x - jk_y y}dk_x dk_y. \qquad (2.55)$$

It can be observed from (2.22), (2.23), that it is possible to write the spectral Green's function as

$$\underline{\underline{\hat{\mathbf{G}}}}^{PQ}(k_x, k_y, z, \mathbf{r}') = \underline{\underline{\hat{\mathbf{G}}}}^{PQ}_0(k_x, k_y, z, z')e^{jk_x x' + jk_y y'}. \qquad (2.56)$$

Now, assume that the surface-current densities are defined on a domain $S$ that lies in the $x - y$ plane, i.e., the surface-current densities have no $z$-dependence. In this case, the magnetic vector potential can be rewritten as [see (2.54), (2.56)]

$$\mathbf{A}(\mathbf{r}) =$$

$$\frac{1}{4\pi^2}\int\limits_{S'}\left[\int\limits_{-\infty}^{\infty}\int\limits_{-\infty}^{\infty}\underline{\underline{\hat{\mathbf{G}}}}^{AJ}_0(k_x, k_y, z, z')e^{jk_x x' + jk_y y'}e^{-jk_x x - jk_y y}dk_x dk_y\right] \cdot \mathbf{f}_n(\mathbf{r}') \, dS'$$

$$= \frac{1}{4\pi^2}\int\limits_{\mathbb{R}^{2'}}\left[\int\limits_{-\infty}^{\infty}\int\limits_{-\infty}^{\infty}\underline{\underline{\hat{\mathbf{G}}}}^{AJ}_0(k_x, k_y, z, z')e^{jk_x x' + jk_y y'}e^{-jk_x x - jk_y y}dk_x dk_y\right] \cdot \tilde{\mathbf{f}}_n(\mathbf{r}') \, dx'dy'$$

$$= \frac{1}{4\pi^2}\int\limits_{-\infty}^{\infty}\int\limits_{-\infty}^{\infty}\left[\underline{\underline{\hat{\mathbf{G}}}}^{AJ}_0(k_x, k_y, z, z')e^{-jk_x x - jk_y y}\right] \cdot \hat{\mathbf{f}}_n(k_x, k_y, z') \, dk_x dk_y,$$

$$(2.57)$$

where $\tilde{\mathbf{f}}_n$ is $\mathbf{f}_n$ extended by zero on the domain $\mathbb{R}^2$ and $\hat{\mathbf{f}}_n$ is the spectral-domain representation of $\tilde{\mathbf{f}}_n$. Similarly, the electric vector potential is represented as

$$\mathbf{F}(\mathbf{r}) = \frac{1}{4\pi^2}\int\limits_{-\infty}^{\infty}\int\limits_{-\infty}^{\infty}\left[\underline{\underline{\hat{\mathbf{G}}}}^{FJ}_0(k_x, k_y, z, z')e^{-jk_x x - jk_y y}\right] \cdot \hat{\mathbf{f}}_n(k_x, k_y, z') \, dk_x dk_y. \quad (2.58)$$

It is important that the spectral-domain representation of the expansion function can be obtained analytically to simplify the evaluation of the vector potentials. To further

simplify the evaluation of the matrix element, the inner product with the test function
is written as

$$
\begin{aligned}
\mathrm{Z}_{mn} &= \Big\langle \mathbf{g}_m(\mathbf{r}), \mathbb{L}\{\mathbf{f}_n\}(\mathbf{r}) \Big\rangle \\
&= \int_S \mathbf{g}_m(\mathbf{r}) \cdot \mathbb{L}\{\mathbf{f}_n\}(\mathbf{r})\, dS \\
&= -\int_S \mathbf{g}_m(\mathbf{r}) \cdot \frac{j\omega}{k^2}\Big[k^2 + \nabla\nabla\cdot\Big]\mathbf{A}(\mathbf{r})\, dS - \int_S \mathbf{g}_m(\mathbf{r}) \cdot \frac{1}{\varepsilon}\nabla \times \mathbf{F}(\mathbf{r})\, dS \\
&= \mathrm{Z}_{mn}^A + \mathrm{Z}_{mn}^F.
\end{aligned}
\tag{2.59}
$$

Here, the term $\mathrm{Z}_{mn}^A$ is determined from (2.57), (2.59) as

$$
\begin{aligned}
\mathrm{Z}_{mn}^A = & -\int_S \mathbf{g}_m(\mathbf{r}) \cdot \Bigg[ \frac{j\omega}{4\pi^2 k^2}\Big[k^2 + \nabla\nabla\cdot\Big] \\
& \int_{-\infty}^{\infty}\int_{-\infty}^{\infty} \Big[ \hat{\underline{\underline{\mathbf{G}}}}_0^{AJ}(k_x, k_y, z, z')e^{-jk_x x - jk_y y} \Big] \cdot \hat{\mathbf{f}}_n(k_x, k_y, z')\, dk_x dk_y \Bigg]\, dS \\
= & -\frac{j\omega}{4\pi^2 k^2}\int_S \mathbf{g}_m(\mathbf{r}) \cdot \Bigg[ \int_{-\infty}^{\infty}\int_{-\infty}^{\infty}\Big[k^2 + \hat{\nabla}\hat{\nabla}\cdot\Big] \\
& \Big[ \hat{\underline{\underline{\mathbf{G}}}}_0^{AJ}(k_x, k_y, z, z')e^{-jk_x x - jk_y y} \Big] \cdot \hat{\mathbf{f}}_n(k_x, k_y, z')\, dk_x dk_y \Bigg]\, dS,
\end{aligned}
\tag{2.60}
$$

where we have introduced the spectral nabla vector as

$$
\hat{\nabla} = \begin{bmatrix} -jk_x \\ -jk_y \\ \partial_z \end{bmatrix}.
\tag{2.61}
$$

Next, the test function $\mathbf{g}_m$ is extended to zero on the domain $\mathbb{R}^2$ and transformed to
the spectral domain, i.e.,

$$
\begin{aligned}
\mathrm{Z}_{mn}^A = & -\frac{j\omega}{4\pi^2 k^2}\int_{-\infty}^{\infty}\int_{-\infty}^{\infty} \hat{\mathbf{g}}_m(-k_x, -k_y, z) \\
& \cdot \Big[k^2 + \hat{\nabla}\hat{\nabla}\cdot\Big]\, \hat{\underline{\underline{\mathbf{G}}}}_0^{AJ}(k_x, k_y, z, z') \cdot \hat{\mathbf{f}}_n(k_x, k_y, z')\, dk_x dk_y.
\end{aligned}
\tag{2.62}
$$

Note that it is assumed here the domain of the test function lies in the $x$-$y$ plane.
Similarly, the term $Z_{mn}^F$ is written as

$$
\begin{aligned}
\mathrm{Z}_{mn}^F = & -\frac{1}{4\pi^2 \varepsilon}\int_{-\infty}^{\infty}\int_{-\infty}^{\infty} \hat{\mathbf{g}}_m(-k_x, -k_y, z) \\
& \cdot \hat{\nabla} \times \hat{\underline{\underline{\mathbf{G}}}}_0^{FJ}(k_x, k_y, z, z') \cdot \hat{\mathbf{f}}_n(k_x, k_y, z')\, dk_x dk_y,
\end{aligned}
\tag{2.63}
$$

and the matrix element is evaluated as

$$
\begin{aligned}
\mathsf{Z}_{mn} &= \mathsf{Z}_{mn}^{A} + \mathsf{Z}_{mn}^{F} \\
&= -\frac{1}{4\pi^2} \int\limits_{-\infty}^{\infty}\int\limits_{-\infty}^{\infty} \hat{\mathbf{g}}_m(-k_x, -k_y, z) \cdot \left[ \frac{j\omega}{k^2}\left[ k^2 + \hat{\nabla}\hat{\nabla}\cdot \right] \underline{\hat{\underline{\mathbf{G}}}}_0^{AJ}(k_x, k_y, z, z') \right. \\
&\quad \left. + \frac{1}{\varepsilon}\hat{\nabla}\times \underline{\hat{\underline{\mathbf{G}}}}_0^{FJ}(k_x, k_y, z, z') \right] \cdot \hat{\mathbf{f}}_n(k_x, k_y, z')\, dk_x dk_y.
\end{aligned}
\tag{2.64}
$$

Here, both the test function and the expansion function are represented in the spectral domain. To obtain a more compact notation, we introduce

$$
\underline{\hat{\underline{\mathbb{L}}}}_0^{Q}(k_x, k_y, z, z') = \frac{j\omega}{k^2}\left[ k^2 + \hat{\nabla}\hat{\nabla}\cdot \right] \underline{\hat{\underline{\mathbf{G}}}}_0^{AQ}(k_x, k_y, z, z') + \frac{1}{\varepsilon}\hat{\nabla}\times\underline{\hat{\underline{\mathbf{G}}}}_0^{FQ}(k_x, k_y, z, z'), \tag{2.65}
$$

where $Q = \{J, M\}$. With the use of this relation, the matrix element can be written as

$$
\begin{aligned}
\mathsf{Z}_{mn} = -\frac{1}{4\pi^2} \int\limits_{-\infty}^{\infty}\int\limits_{-\infty}^{\infty} \hat{\mathbf{g}}_m(-k_x, -k_y, z)\cdot \\
\underline{\hat{\underline{\mathbb{L}}}}_0^{J}(k_x, k_y, z, z')\cdot \hat{\mathbf{f}}_n(k_x, k_y, z')\, dk_x dk_y.
\end{aligned}
\tag{2.66}
$$

To determine $\mathsf{Z}_{mn}$, only the integration over $k_x$ and $k_y$ has to be performed numerically, which is discussed in Section 2.6.2. Note that the assumption was made that the expansion function represents an electric-current density. In case a magnetic-current density is represented, the function $\underline{\hat{\underline{\mathbb{L}}}}_0^{J}$ in (2.66) is replaced by $\underline{\hat{\underline{\mathbb{L}}}}_0^{M}$ [see (2.65)].

A common choice for the test functions is the use of the same functions as the expansion functions, i.e. $\mathbf{g}_i(\mathbf{r}) = \mathbf{f}_i(\mathbf{r})$. This particular choice is known as Galerkin testing and it is generally a good way of testing the EFIE and MFIE. Moreover, it has the advantage that it introduces symmetry in the interaction matrix, such that only approximately half the matrix elements have to be evaluated.

## 2.6.2 Numerical evaluation of the integral terms

In the spectral-domain representation, two integrals need to be determined numerically to obtain the elements of the MoM matrix. To facilitate this integration, the spectral wavenumbers $k_x$, $k_y$ are transformed into cylindrical coordinates $k_\rho$, $\psi$ through the relation

$$
\begin{aligned}
k_x &= k_\rho \cos(\psi), \\
k_y &= k_\rho \sin(\psi).
\end{aligned}
\tag{2.67}
$$

In this way, a matrix term can be written as [see (2.66)]

$$
\mathsf{z}_{mn} = -\frac{1}{4\pi^2} \int\limits_0^\infty \int\limits_0^{2\pi} \hat{\mathbf{g}}_m(-k_\rho, \psi, z) \cdot
$$

$$
\hat{\underline{\underline{\mathbb{L}}}}_0^Q(k_\rho, \psi, z, z') \cdot \hat{\mathbf{f}}_n(k_\rho, \psi, z') \; k_\rho \; d\psi dk_\rho.
$$

(2.68)

The inner integration over the radial term $\psi$ can be performed by a straightforward numerical integration method like, for example, Romberg integration [24]. The integration over $k_\rho$ is more complicated, as we will show that $\hat{\underline{\underline{\mathbb{L}}}}_0^Q$ is a double-value function that contains singularities.

The function $\hat{\underline{\underline{\mathbb{L}}}}_0^Q$ is a double-value function because it contains the Green's functions $\hat{\underline{\underline{\mathbf{G}}}}^{AQ}$ and $\hat{\underline{\underline{\mathbf{G}}}}^{FQ}$ [see (2.65)] which, in turn, contain the terms $k_z^n$ [see e.g. (2.22), (2.23)]. Recall that these terms are represented as

$$
k_z^n = \sqrt{k_n^2 - k_\rho^2},
$$

(2.69)

which is a double-value function, since the square root function has two solutions. Normally, both $+k_z^n$ and $-k_z^n$ are present in the Green's function of layer $n$ and the Green's function has an unique value (see also [18, Section 2.7.1]). However, in the upper layer of the stratification ($n = 0$), only one term is present. In this layer, a component of the Green's dyadic function is written as [see (2.28)]

$$
\hat{G}_{zi}^{AQ,0} = K^0 e^{-jk_z^0(z-z^0)}.
$$

(2.70)

To satisfy the radiation condition in this region, it is required that $\mathsf{Im}\{k_z^0\} \le 0$, such that the field vanishes for $z \to +\infty$. This requirement determines the sign of the square root function in (2.69) and holds for every layer $n$.

The function $\hat{\underline{\underline{\mathbb{L}}}}_0^Q$ has singularities that are located on or near the real axis of the $k_\rho$ plane as shown in Fig. 2.6 and those singularities actually represent radiation and surface waves (see also Section 2.7). To avoid numerical problems with these singularities, the contour of the integral is deformed such that the integrand has no singularities on the path of integration and does not intersect with any of the branch cuts that are defined by $\mathsf{Im}\{k_z^n\} = 0$. The unbounded integral over $k_\rho$ can now be determined using an adaptive integration method (e.g. function D01AMF of the NAG library [25]).

## 2.7   Surface waves

An important aspect in the analysis of stratified media relates to the presence of surface waves. Surface waves are waves that are guided by the stratified medium and
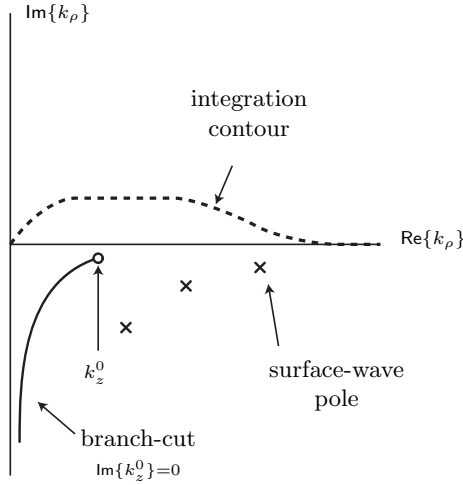
Figure 2.6: Branch-cut, surface-wave poles and integration contour of $\hat{\underline{\underline{\mathbb{L}}}}_0^Q$ in the $k_\rho$-plane.

that propagate in the lateral direction. Antenna structures that are embedded in stratified media, excite these surface waves and therefore less power is radiated into free space. As a result, the radiation efficiency is reduced. Moreover, in a practical application, the dielectric layers will always have a finite size and the surface waves scatter at the edges of the finite layers. This leads to unwanted radiation that can deteriorate the radiation pattern of the antenna. Therefore it is important to quantify this effect.

The complex source power that is generated by an electric-current density $\mathbf{J}$ is given as

$$P = -\int_S \mathbf{E}(\mathbf{r}) \cdot \mathbf{J}^*(\mathbf{r}) dS, \tag{2.71}$$

where $\mathbf{E}$ is the electric field that is generated by $\mathbf{J}$. Note that this expression is very similar to the obtained expression of a matrix element [see (2.42)], since we can write

$$
\begin{aligned}
P &= -\Big\langle \mathbf{J}^*(\mathbf{r}), \mathbf{E}(\mathbf{r}) \Big\rangle \\
&= -\Big\langle \mathbf{J}^*(\mathbf{r}), \mathbb{L}\{\mathbf{J}, \mathbf{0}\}(\mathbf{r}) \Big\rangle.
\end{aligned}
\tag{2.72}
$$

When the current-density is located in the $x$-$y$ plane, the complex source power can be written as

$$P = \frac{1}{4\pi^2} \int_0^\infty \int_0^{2\pi} \hat{\mathbf{J}}(k_\rho, \psi, z) \cdot \hat{\underline{\underline{\mathbb{L}}}}_0^J(k_\rho, \psi, z, z') \cdot \hat{\mathbf{J}}(k_\rho, \psi, z') \, k_\rho \, d\psi dk_\rho, \tag{2.73}$$

following the same approach as in Section 2.6. The amount of power that is radiated
into free space can be determined from (2.73). To show this, consider (2.70) again.
For $|k_\rho| \le k_0$, a wave propagates in the positive $z$-direction and therefore power
is radiated. For $|k_\rho| > k_0$, this wave decays exponentially, and therefore no power
is radiated. Consequently, the complex radiated power $P^{\mathrm{rad}}$ can be determined by
limiting the integral over $k_\rho$ in (2.73) to $0 < k_\rho < k_0$, viz,

$$P^{\mathrm{rad}} = \frac{1}{4\pi^2} \int\limits_0^{k_0} \int\limits_0^{2\pi} \hat{\mathbf{J}}(k_\rho, \psi, z) \cdot \underline{\hat{\underline{\mathbb{L}}}}_0^J(k_\rho, \psi, z, z') \cdot \hat{\mathbf{J}}(k_\rho, \psi, z') \ k_\rho \ d\psi dk_\rho. \tag{2.74}$$

Now, if the substrate is lossless, the surface-wave power $P^{\mathrm{sw}}$ can be determined as

$$P^{\mathrm{sw}} = P - P^{\mathrm{rad}}. \tag{2.75}$$

In case the substrate is lossy, the difference $P - P^{\mathrm{rad}}$ includes both the power that is
dissipated in the dielectric and the surface-wave power.

When the field problem is solved with the MoM, the currents are expanded in terms
of basis functions $\mathbf{f}_n$. In this case, the complex source power (2.73) can be expressed
as

$$P = \frac{1}{4\pi^2} \sum_m \sum_n \int\limits_0^\infty \int\limits_0^{2\pi} \kappa_m^* \hat{\mathbf{f}}_m(k_\rho, \psi, z) \cdot \underline{\hat{\underline{\mathbb{L}}}}_0^J(k_\rho, \psi, z, z') \cdot \kappa_n \hat{\mathbf{f}}_n(k_\rho, \psi, z') \ k_\rho \ d\psi dk_\rho.$$
$$\tag{2.76}$$

The complex source power can be written in terms of the interaction matrix $\mathtt{Z}$ and
the current coefficient vector $\mathtt{I}$ as

$$P = \mathtt{I}^H \mathtt{Z} \mathtt{I}, \tag{2.77}$$

where the superscript $H$ denotes the Hermitian (complex transpose) of the vector.
Similarly, the radiated power is determined as

$$P^{\mathrm{rad}} = \mathtt{I}^H \mathtt{Z}^{\mathrm{rad}} \mathtt{I}, \tag{2.78}$$

where the elements of the matrix $\mathtt{Z}^{\mathrm{rad}}$ are defined as [see (2.74)]

$$\mathtt{Z}_{mn}^{\mathrm{rad}} = \frac{1}{4\pi^2} \int\limits_0^{k_0} \int\limits_0^{2\pi} \hat{\mathbf{f}}_m(k_\rho, \psi, z) \cdot \underline{\hat{\underline{\mathbb{L}}}}_0^J(k_\rho, \psi, z, z') \cdot \hat{\mathbf{f}}_n(k_\rho, \psi, z') \ k_\rho \ d\psi dk_\rho. \tag{2.79}$$

Often, we are more interested in the time-averaged power instead of the complex
power. The time-averaged power $< P >$ is related to the complex power as [20,
Chapt. 4]

$$< P > = \frac{1}{2} \mathsf{Re}\{P\}. \tag{2.80}$$
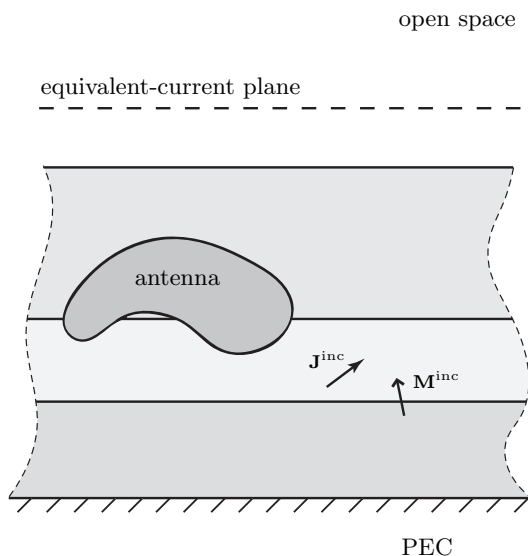
open space

equivalent-current plane



PEC

Figure 2.7: Equivalent-current plane for an embedded antenna.

## 2.8 Radiation

The radiation pattern of an antenna is one of its most important characteristics. In this section, it is explained how to obtain the radiation pattern of a planar antenna that is embedded in a stratified medium. The method that is applied here, relies on the application of the equivalence theorem that has been used in Section 2.5 to derive the MoM formulation. The presented method can also be found in [26].

Consider an antenna that is embedded in a stratified medium. The fields radiated into the upper region (layer 0) can be represented in terms of an equivalent problem, where equivalent electric-current and magnetic-current densities are introduced in the $x$-$y$ plane (Fig. 2.7). Above the plane that contains the equivalent current densities, the original field distribution is obtained, whereas below this plane no field is present outside the source regions. Since the field is absent, it is possible to replace the stratification with another medium. Now, replace the stratified medium with a PEC. In this way, the electric-current densities do not radiate and the radiation pattern is determined by the equivalent magnetic-current densities only. The fields resulting from a magnetic source $\mathbf{M}$ above a PEC can be obtained from yet another equivalent problem using Schelkunoff's equivalence principle [20, Chapt. 6]. Schelkunoff's equivalence principle states that these fields are identical to the fields of a magnetic source in a homogeneous medium if $\mathbf{M}$ is replaced by $2\mathbf{M}$. The electric field at $\mathbf{r}$ resulting

from these magnetic sources in a homogeneous medium can be obtained from

$$\mathbf{E}(\mathbf{r}) = -\nabla \times \int_{S'} 2\mathbf{M}(\mathbf{r}') \frac{1}{4\pi|\mathbf{r} - \mathbf{r}'|} e^{-jk_0|\mathbf{r} - \mathbf{r}'|} dx' dy'. \tag{2.81}$$

In the far-field region, this expression can be approximated since $|\mathbf{r} - \mathbf{r}'| \to |\mathbf{r}|$ and $\nabla \to \mathbf{u}_r \partial_r$, i.e.,

$$\mathbf{E}(\mathbf{r}) = \frac{jk_0}{2\pi|\mathbf{r}|} e^{-jk_0|\mathbf{r}|} \left[ \mathbf{u}_r \times \iint \mathbf{M}(\mathbf{r}') e^{jk_0 \mathbf{u}_r \cdot \mathbf{r}'} dx' dy' \right]. \tag{2.82}$$

Here $\mathbf{u}_r$ is a unit vector that is pointing towards $\mathbf{r}$. The vector $\mathbf{u}_r$ can be written in terms of spherical coordinates $\theta$, $\phi$ as

$$\mathbf{u}_r = \sin(\theta) \cos(\phi) \mathbf{u}_x + \sin(\theta) \sin(\phi) \mathbf{u}_y + \cos(\theta) \mathbf{u}_z. \tag{2.83}$$

Now introduce the spectral-domain coordinates

$$\begin{aligned} k_x &= k_0 \sin(\theta) \cos(\phi), \\ k_y &= k_0 \sin(\theta) \sin(\phi), \end{aligned} \tag{2.84}$$

and substitute (2.83), (2.84) in (2.82) to obtain

$$\begin{aligned} \mathbf{E}(\mathbf{r}) &= \frac{jk_0}{2\pi|\mathbf{r}|} e^{-jk_0|\mathbf{r}|} \Big[ \mathbf{u}_r \times \\ &\quad \iint \mathbf{M}(\mathbf{r}') e^{jk_0[x'\sin(\theta)\cos(\phi) + y'\sin(\theta)\sin(\phi) + z'\cos(\theta)]} dx' dy' \Big] \\ &= \frac{jk_0}{2\pi|\mathbf{r}|} e^{-jk_0[|\mathbf{r}| - z'\cos(\theta)]} \left[ \mathbf{u}_r \times \iint \mathbf{M}(\mathbf{r}') e^{jk_x x' + jk_y y'} dx' dy' \right] \end{aligned} \tag{2.85}$$

The last double integral of this equation can be interpreted as a Fourier integral and the equivalent magnetic source can be expressed in terms of the original field using (2.31) with $\mathbf{n} = \mathbf{u}_z$, viz,

$$\begin{aligned} \iint \mathbf{M}(\mathbf{r}') e^{jk_x x' + jk_y y'} dx' dy' &= -\mathbf{u}_z \times \iint \mathbf{E}(\mathbf{r}') e^{jk_x x' + jk_y y'} dx' dy' \\ &= -\mathbf{u}_z \times \hat{\mathbf{E}}(k_x, k_y, z'). \end{aligned} \tag{2.86}$$

The far field can now be expressed in closed-form as

$$\begin{aligned} \mathbf{E}(\mathbf{r}) &= -\frac{jk_0}{2\pi|\mathbf{r}|} e^{-jk_0[|\mathbf{r}| - z'\cos(\theta)]} \left[ \mathbf{u}_r \times \mathbf{u}_z \times \hat{\mathbf{E}}(k_x, k_y, z') \right] \\ &= \frac{jk_0}{2\pi|\mathbf{r}|} e^{-jk_0[|\mathbf{r}| - z'\cos(\theta)]} \cdot \\ &\quad \Big[ \{ \hat{\mathbf{E}}_y(k_x, k_y, z') \cos(\theta) \cos(\phi) - \hat{\mathbf{E}}_x(k_x, k_y, z') \cos(\theta) \sin(\phi) \} \mathbf{u}_\phi \\ &\quad - \{ \hat{\mathbf{E}}_x(k_x, k_y, z') \cos(\phi) + \hat{\mathbf{E}}_y(k_x, k_y, z') \sin(\phi) \} \mathbf{u}_\theta \Big]. \end{aligned} \tag{2.87}$$

From the radiation pattern it is possible to determine the gain and the directivity of the antenna as well. The directivity $D$ of an antenna is defined as the ratio of the radiation intensity in a specific direction and the average radiation intensity [10, Chapt. 1] and can be expressed as

$$D(\theta, \phi) = 4\pi \frac{|\mathbf{E}(\mathbf{r})|^2}{\int\limits_{-\pi}^{\pi} \int\limits_{0}^{\pi} |\mathbf{E}(\mathbf{r})|^2 \sin(\theta) d\phi d\theta}. \tag{2.88}$$

The gain $G$ of an antenna is defined as the ratio of radiation intensity per unit solid angle and power accepted by the antenna [10, Chapt. 1]. It can be expressed in terms of the antenna directivity as

$$G(\theta, \phi) = \eta D(\theta, \phi), \tag{2.89}$$

where $\eta$ is the radiation efficiency that accounts for the power losses in the antenna. The radiation efficiency can be determined as the ratio of radiated power $P^{\mathrm{rad}}$ and input power $P^{\mathrm{in}}$ that is accepted by the antenna, i.e.,

$$\eta = \frac{P^{\mathrm{rad}}}{P^{\mathrm{in}}}. \tag{2.90}$$

## 2.9 Excitation

To find an appropriate field solution, an accurate description of the sources in the considered EM problem is needed. In this work, two different source types are used, viz, a delta-gap voltage source (Section 2.9.1) and a travelling-wave current-density source (Section 2.9.2). The delta-gap voltage source is used for the excitation of dipole-like structures, whereas the travelling-wave current-density source is used for the excitation of transmission lines.

### 2.9.1 Delta-gap voltage source

The delta-gap voltage source impresses an electric field between two (planar) metal structures (see Fig. 2.8). The electric field in the gap region is assumed constant and is related to the port voltage $V^p$ as

$$V^p = -\int_{x_g - L/2}^{x_g + L/2} E_x^{\mathrm{inc}}(x, y_g, z_g) \, dx, \tag{2.91}$$

where $\mathbf{r}_g = (x_g, y_g, z_g)$ specifies the center of the rectangular gap and $L$ determines the length of the gap, respectively. In general, a delta-gap voltage is used in which
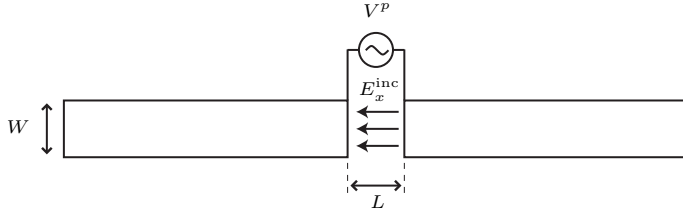
Figure 2.8: Example of a dipole with a delta-gap voltage source.

the length of the gap vanishes, i.e.,

$$V^p = -\lim_{L\downarrow 0} \int_{x_g-L/2}^{x_g+L/2} E_x^{\text{inc}}(x, y_g, z_g) \, dx. \tag{2.92}$$

Alternatively, this can be expressed as

$$E_x^{\text{inc}}(x, y_g, z_g) = -V^p \, \delta(x - x_g). \tag{2.93}$$

### 2.9.2   Travelling-wave current-density source

Another important excitation method is the use of the travelling-wave current-density source [27]. This method is used for the excitation of planar transmission lines, like microstrip lines. The current density on the transmission line is expanded into a travelling wave that is incident on the EM structure and a travelling wave that is reflected from the EM structure. In the region where the current distribution of the incident and reflected travelling wave is affected by EM structure, additional basis functions (e.g. rooftop basis functions) are placed to model the current-density distribution accurately.

The travelling-wave current-density on a $x$-directed microstrip line of infinite length and width $W$ can be expressed as

$$\mathbf{f}^{\text{tw}}(\mathbf{r}) = e^{-jk_e x} \, \mathbf{u}_x, \tag{2.94}$$

where $\mathbf{r} = (x, y, z)$, $|y| < W/2$, $z = z^{\text{tw}}$ and $k_e$ is the effective propagation constant of the travelling wave. In this formulation, only $x$-directed currents are present, which is a valid assumption for lines that are not too wide [28]. As a rule of thumb, the width $W$ should be less than $\lambda_d/10$, where $\lambda_d = 2\pi/k_e$ represents the effective wavelength.

The effective propagation constant $k_e$ can be found from the requirement that the tangential electric field on the microstrip line should vanish. This boundary condition

is enforced across the strip by integration over $y$, i.e.,

$$\int\limits_{y=-W/2}^{y=W/2} \mathbb{L}\{\mathbf{f}^{\text{tw}}, \mathbf{0}\}(\mathbf{r}) \cdot \mathbf{u}_x \, dy = 0, \qquad (2.95)$$

and should be valid for all $x$. In the spectral domain, $\hat{\mathbf{f}}^{\text{tw}}$ is given by

$$\hat{\mathbf{f}}^{\text{tw}}(k_x, k_y, z) = \hat{f}_y^{\text{tw}}(k_y)\delta(k_x - k_e)\,\mathbf{u}_x, \qquad (2.96)$$

with

$$\hat{f}_y^{\text{tw}}(k_y) = \frac{2\sin(k_y W/2)}{k_y}. \qquad (2.97)$$

This allows us to write (2.95) in the spectral domain as (see also [27])

$$\frac{1}{4\pi^2} \int\limits_{-\infty}^{\infty} \hat{f}_y^{\text{tw}}(-k_y)\mathbf{u}_x \cdot \hat{\underline{\underline{\mathbb{L}}}}_0^{J}(k_e, k_y, z^{\text{tw}}, z^{\text{tw}}) \cdot \hat{f}_y^{\text{tw}}(k_y)\mathbf{u}_x \, dk_y = 0. \qquad (2.98)$$

Note that $k_e$ lies in between $k_0$ and $k_0\sqrt{\varepsilon_r^{\text{max}}}$, where $\varepsilon_r^{\text{max}}$ is the maximum relative dielectric constant of the stratification. The value of $k_e$ that solves (2.98) can be found with a search technique like the bisection method.

Once the travelling-wave current-density for a microstrip line of infinite length has been determined, the solution is used to model the behaviour of a finite EM structure. For example, in case of an open-ended microstrip line (Fig. 2.9), the current on the line can be modelled by an incident and a reflected travelling-wave current-density functions and additional subdomain basis functions near the end of the line, where the current density is different from the travelling-wave solution.

## 2.10 Example: planar dipole

To verify the derived formulation and to demonstrate its use, a planar dipole is modelled. This dipole is located on top of a single-layer dielectric (see Fig. 2.10a). Equivalent electric-current densities are introduced to obtain an equivalent model that describes the fields in the exterior region (Fig. 2.10b). In case the metal thickness $t_m$ of the planar dipole is much smaller than the wavelength $\lambda$, the equivalent surface-current densities on the surface of the dipole can be approximated by equivalent surface-current densities that are located on an infinitely thin sheet (Fig. 2.10c). These current densities represent the sum of the original current densities $\mathbf{J}^{\text{eq},1}$, $\mathbf{J}^{\text{eq},2}$ that are located on the top and bottom of the dipole, i.e.,

$$\mathbf{J}^{\text{eq}} = \mathbf{J}^{\text{eq},1} + \mathbf{J}^{\text{eq},2}. \qquad (2.99)$$
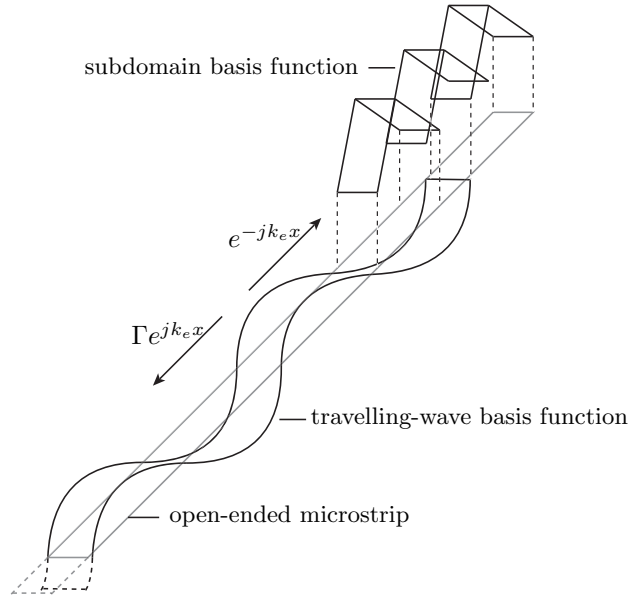
Figure 2.9: Example of an open-ended microstrip line with travelling-wave basis functions and subdomain basis functions.

The equivalent currents on this infinitely thin sheet are now expanded in terms of $N_d$ rooftop basis functions and the EFIE (2.32) is solved with the MoM. The rooftop basis functions are defined as

$$\mathbf{f}_n(\mathbf{r}) = 1 - \frac{|x - x_n|}{L}, \tag{2.100}$$

where $|x - x_n| < L$, $|y| < W/2$, $z = z^0$, $0 < n < N_d - 1$, and $x_n$ represents the center coordinate in the $x$ direction of the $n^{\text{th}}$ rooftop. The excitation of the dipole is realised by a delta-gap voltage source (see Section 2.9.1). The incident field is defined as

$$\mathbf{E}^{\text{inc}}(\mathbf{r}) = -V^p \delta(x) \mathbf{u}_x, \tag{2.101}$$

where $|y| < W/2$, $z = z^0$ and $V^p$ is the port voltage. Let us assume that we have an odd number $N_d$ of rooftop basis functions. In this case, the elements of the excitation vector can be determined as [see (2.42)]

$$\begin{aligned}
\mathtt{V}_m &= -\Big\langle \mathbf{g}_m(\mathbf{r}), \mathbf{E}^{\text{inc}}(\mathbf{r}) \Big\rangle \\
&= \begin{cases} W V^p & n = (N_d - 1)/2 \\ 0 & n \neq (N_d - 1)/2 \end{cases} .
\end{aligned} \tag{2.102}$$

The elements of the interaction matrix can be determined from (2.42) and (2.66), where the double integral is calculated through the approach described in Section 2.6.2.
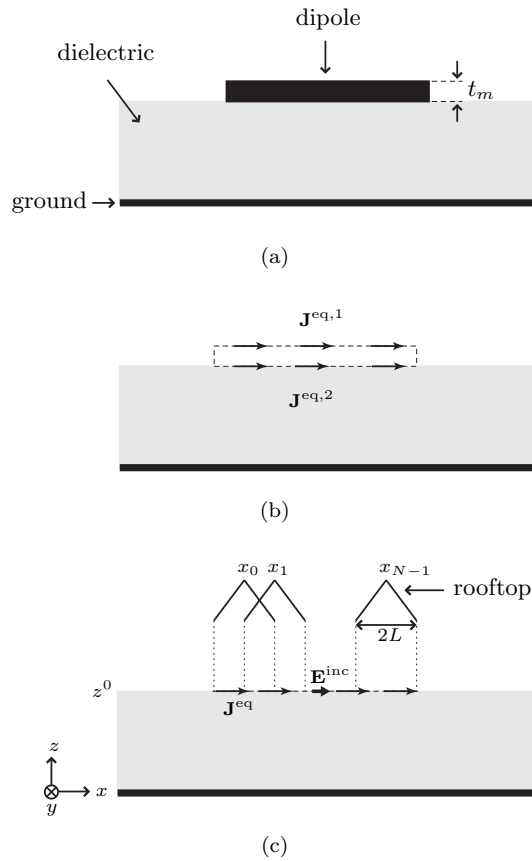
Figure 2.10: Modelling of a planar dipole on a dielectric substrate. (a) Geometry of the planar dipole. (b) Equivalent problem for the exterior region. (c) Equivalent problem with approximated equivalent currents and rooftop basis functions.
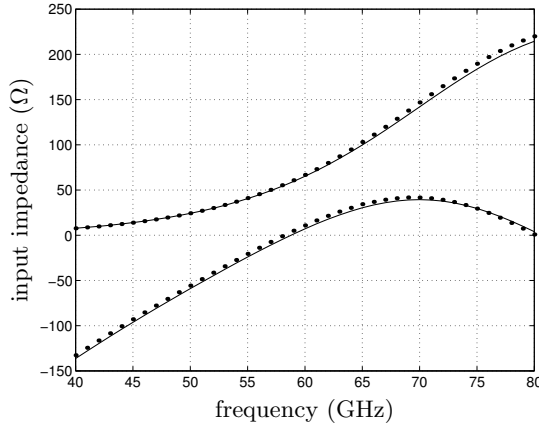
Figure 2.11: Input impedance half-wavelength dipole. Ansoft Designer (solid), Spark (dots). Length dipole: $l = 2.5/\sqrt{\varepsilon_r}$ mm, width dipole: $l/10$, thickness dielectric: 0.8 mm, relative permittivity dielectric: $\varepsilon_r = 2$.

Once the excitation vector and the interaction matrix have been determined, the equivalent currents on the dipole can be determined from (2.43). The input impedance of the dipole can be found by defining a port voltage $V^p$ and a port current $I^p$. The port voltage is specified in (2.101), whereas the port current is defined as the current that flows on the dipole through the plane $x = 0$, viz,

$$I^p = \int_{S_{\mathrm{gap}}} \mathbf{J}(\mathbf{r}) \cdot \mathbf{u}_x \; dydz \tag{2.103}$$
$$= \mathtt{I}_{(N_d-1)/2} W.$$

The input impedance is obtained from the ratio of the port voltage and the port current, i.e.,

$$Z_{\mathrm{in}} = -\frac{V^p}{I^p}. \tag{2.104}$$

Greens functions for stratified media and the required integration routines have been implemented in a software code that has been written in C++. This code is named Spark. To validate the software code, a number of simulations have been performed. For example, the input impedance of a half-wavelength planar dipole on top of a single-layer dielectric slab has been simulated (Fig. 2.11). The results have been compared with Ansoft Designer, a commercial planar electromagnetic simulator that employs a triangular mesh. Spark used $N_d = 11$ rooftop basis functions for this simulation, whereas Ansoft Designer employed 24 triangular mesh cells. It is observed that the agreement is very good.

The directivity and the gain of the dipole have been calculated as well (see Section 2.8). Again, the results are in good agreement with results obtained from Ansoft Designer.
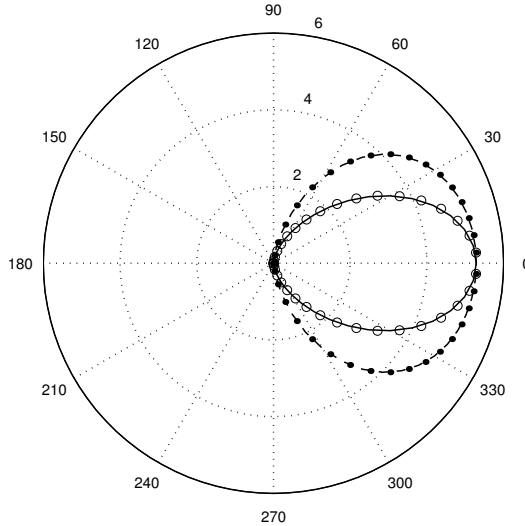
Figure 2.12: Radiation pattern half-wavelength dipole. Frequency $f = 60$ GHz. $\phi = 0°$ plane: Ansoft Designer (solid), Spark ($\circ$). $\phi = 90°$ plane: Ansoft Designer (dashed), Spark (dots). Dimensions as in Fig. 2.11.

The radiation patterns are compared at the frequency $f = 60$ GHz in Fig. 2.12. The radiation efficiency of the antenna is obtained as [see (2.90), (2.80), (2.77), (2.78)]

$$
\begin{aligned}
\eta &= \frac{P^{\mathrm{rad}}}{P^{\mathrm{in}}} \\
&= \frac{\mathrm{Re}\{\mathtt{I}^H \mathtt{Z}^{\mathrm{rad}} \mathtt{I}\}}{\mathrm{Re}\{\mathtt{I}^H \mathtt{Z} \mathtt{I}\}},
\end{aligned}
\tag{2.105}
$$

and is shown in Fig. 2.13.

## 2.11 Comparison of Spark with other EM modelling tools

In this work, several EM modelling tools are used in parallel. The EM modelling that is presented in this thesis is implemented in a software code named Spark. Spark is based on the theory that is described in this chapter. It has been extended for the optimisation of EM structures (see Chapter 5) and for the analysis of antenna arrays (see Chapter 6). In parallel, two other EM modelling tools are used as well, viz, Ansoft Designer [29] and CST Microwave Studio [30]. The differences between Spark and these tools are discussed below.
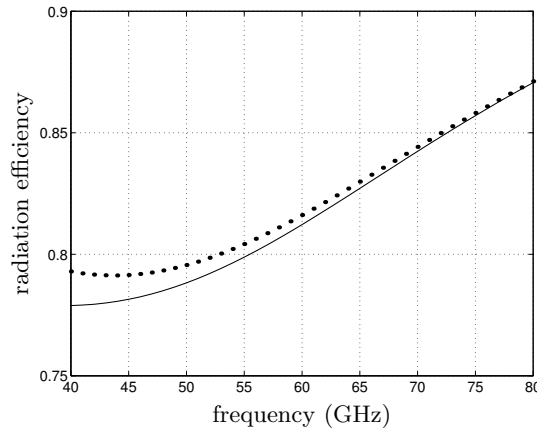
Figure 2.13: Radiation efficiency half-wavelength dipole. Ansoft Designer (solid), Spark (dots). Dimensions as in Fig. 2.11.

Ansoft Designer is a commercial planar electromagnetic simulator. It is similar to Spark in the sense that it assumes a stratified background medium that extends to infinity in the lateral direction. Therefore, it cannot predict edge effects due to the finite size of the dielectric layers in the lateral direction (neither can Spark). It is different from Spark for three important reasons. The first reason is associated to the choice of basis functions for the approximation of the surface-current densities. Ansoft Designer employs Rao-Wilton-Glisson (RWG) basis functions [31], which results in a set of sub-domain basis functions that is suited for almost every planar structure. However, Spark employs both entire-domain and sub-domain basis functions, which allows us to choose a set of basis functions that is tailored for the problem under consideration. As a result, the number of basis functions needed in Spark is significantly lower than the number of basis functions that are used by Ansoft Designer for the EM problems that are considered in this work. This implies that Spark is inherently more efficient in terms of computational resources. The second reason is the optimisation routine that is available in Spark. The optimisation method that is proposed in Chapter 5 enables an accurate and robust evaluation of the sensitivity of the EM problem under consideration. Therefore, it is noticed that Spark is able to optimise many EM problems within few iterations. For example, the antenna optimisation presented in Section 5.5 is optimised within 10 iterations, whereas Ansoft Designer is not able to find an optimum at all. On the other hand, an advantage of Ansoft Designer is its capability to analyse finite-thickness metal layers, whereas Spark is not. The third reason, is the ability of Spark to determine the radiation efficiency of the EM structure. Ansoft Designer can determine this efficiency only from the ratio of radiated power and input power at the circuit port, whereas Spark can explicitly determine the surface-wave power that is generated by any surface-current density source. This is more flexible, since Spark is therefore also able to determine the efficiency of separate regions within a stack (see e.g. Section 3.4).

| | Spark | Ansoft Designer | CST MWS |
|---|:---:|:---:|:---:|
| computational efficiency | ✓ | − | − |
| surface waves | ✓ | − | − |
| finite metal thickness | − | ✓ | − |
| optimisation | ✓ | − | − |
| edge effects | − | − | ✓ |

Table 2.1: Strong points of EM modelling tools for planar antenna applications.

CST Microwave Studio is based on the finite integration technique [32] that provides a discrete reformulation of Maxwell's equations in their integral form. It employs finite-volume discretisation and therefore it can handle three-dimensional geometries. As a result, it is able to account for the edge-effect of dielectric layers that have finite dimensions in the lateral direction. The drawback of CST Microwave Studio is that it is computationally much more demanding than both Ansoft Designer and Spark, because the complete volume of the computational domain needs to be meshed. Therefore it is especially employed in the final stage of the design and in the validation of the measured radiation pattern that includes the edge effects of the dielectric layers.

To summarise, the strong points of each EM modelling tool for our application are listed in Table 2.1. From this table, it is possible to derive for which purpose each tool is most suited in the analysis of planar antennas and antenna arrays. Note that this does not necessarily imply that the other tools are not suited at all.

## 2.12 Conclusions

In this chapter, an approach has been presented for the electromagnetic modelling of planar antenna structures. First, Green's functions for stratified media have been derived. These Green's functions describe the field that is generated by an electric or magnetic point source in the stratified medium. Integral equations have been formulated for the modelling of more complex objects and sources inside the stratification. The integral equations are expressed in terms of equivalent surface-current densities. A MoM approach has been described that solves the approximated surface-current densities numerically. In this work, the focus lies on the design of planar antennas. Since surface waves have an important effect on antenna performance, they are investigated as well. Obviously, also the radiation of planar EM structures is discussed. To excite the antenna structures, two commonly used excitation methods are presented. The proposed modelling methods have been implemented in a software code named Spark. An example has been given to clarify the proposed modelling methods and to verify the implementation of Spark.

The presented EM modelling will be employed throughout the thesis, especially in the next chapter, where the design of an antenna element is presented that is used for the realisation of the planar beam-forming antenna array. Moreover, the modelling is extended for the optimisation of planar EM structures in Chapter 5 and for the analysis of antenna arrays in Chapter 6.

# Balanced-fed aperture-coupled patch antenna

## 3.1 Introduction

The performance of planar antennas can be evaluated with the modelling method that is presented in previous chapter. To determine which antenna topology is most suited for the transceiver system, a number of requirements should be taken into account in the design. The most important requirements can be listed as follows:

- The antenna should have sufficient bandwidth to cover the available unlicensed frequency band at 60 GHz. The available bandwidth is regulated differently in Europe, United States (US) and Japan. However, 5 GHz of unlicensed bandwidth is available throughout the world.

- The antenna has to be integrated with active electronics and therefore the integration of the antenna and the radio-frequency integrated circuit (RFIC) should be given consideration. A balanced interconnect between antenna and RFIC improves the performance of the system, since this type of interconnect is less sensitive to ground inductance, has the ability to reject common-mode distur-

bances, and is easier to realise [33]. Therefore, an antenna with a balanced feed is required.

- Since it is difficult to realise sufficiently high transmit power, it is important that the antenna element has a high radiation efficiency such that losses are minimised.

- The transceiver should be low-cost and therefore a standard planar manufacturing technology needs to be used for the realisation of the antenna. A planar technology allows for a simple integration with the RFIC as well.

- To fulfill the link budget requirements for multiple gigabit-per-second (Gbps) transmission, front-ends with several power amplifiers are needed to generate the required transmit power at 60 GHz. Additionally, antennas are needed that have sufficient gain and that support beam-forming. To obtain sufficient gain and to realise beam-forming, antenna arrays are needed. Therefore the antenna element needs to be suited for integration in array configurations.

- The antenna should have a well-defined feed that is low-loss and does not influence the performance of the antenna element. Moreover, the antenna topology should support a feed network that is able to feed an antenna array as well.

To summarise, a balanced antenna is needed that has a high radiation efficiency and sufficient bandwidth. Moreover, this antenna needs to be suited to be placed in array configurations and has to be realised in a low-cost planar manufacturing technology.

The main challenge of antenna design in a planar technology is the trade-off between radiation efficiency and bandwidth. To obtain a large bandwidth, a relatively thick dielectric layer is needed [34]. However, a thicker dielectric layer introduces more losses due to surface-wave excitation in the dielectric. A lot of work has been done to improve the radiation efficiency of planar antennas while maintaining a large bandwidth [35, 36]. Particularly, the use of electromagnetic bandgap (EBG) materials that suppress the surface-wave excitation has received a lot of attention [37, 38, 39]. However, EBG materials are either difficult to manufacture, or too large to be used in planar array configurations. Another approach to improve the radiation efficiency is presented in [40], where a superstrate antenna is used. This solution shows good performance, but is more complicated to realise, since the superstrate antenna is a separate component that has to be placed partly on top of the integrated circuit.

As an alternative, a balanced antenna design is proposed here that is named balanced-fed aperture-coupled patch (BFACP) antenna. In this design, the antenna element itself cancels part of the surface-wave excitation. Because of the reduced surface-wave excitation, a radiation efficiency of over 80% is obtained throughout the band of operation. On top of that, an antenna bandwidth of more than 10% is realised by using two resonant elements. The resulting design is completely planar, and the use of vias is avoided. The width and length of the antenna is less than half a free-space

wavelength, such that the antenna can be readily used for the realisation of a planar beam-forming array.

The design of the BFACP antenna is discussed in detail in Section 3.2, whereas the modelling of the BFACP antenna element is discussed in Section 3.3. It relies on the modelling that is presented in the previous chapter. As mentioned, the antenna should have a high radiation efficiency and this is considered in Section 3.4. Another aspect that is of importance with aperture-coupled patch antennas is the front-to-back ratio which is investigated in Section 3.5. The radiation pattern is evaluated in Section 3.6. Here, the effect of a finite-sized dielectric on the radiation pattern is investigated as well. To simplify the modelling of the antenna, the effect of the metal thickness is not included in the model. The effects of this assumption are discussed in Section 3.7 and a method is proposed to improve the accuracy of the model. Finally, the extension of the BFACP antenna for dual polarisation is discussed in Section 3.8.

## 3.2 Antenna design

The antenna design is based on a balanced-fed aperture-coupled patch antenna [41], which is an aperture-coupled patch antenna with two apertures (slots) that couple to a balanced feed. Aperture-coupled patch antennas have the advantage that they can be integrated with active electronics easily since substrate properties of the feed line can be chosen independently from the substrate properties of the radiating patch [42].

A disadvantage of aperture-coupled patch antennas is the back radiation that is caused by the ground plane in which the slots lie. To reduce the back radiation, a microstrip antenna element is placed behind the slots. This element acts as a reflector [43] and can be placed at a distance from the slots that is much smaller than $\lambda_d/4$, with $\lambda_d$ the wavelength in the dielectric. Therefore, the thickness of the dielectric below the slots remains small in terms of wavelength and the excitation of surface-waves in this layer remains limited. To reduce the back radiation effectively, the size of the reflector element is adjusted [43]. The performance of the reflector element is analysed in Section 3.5.

The two slots play an important role in the antenna design. First, they are used to reduce the surface-wave excitation in the dielectric. The slots are positioned such that the surface waves that are generated by the slots and the patch interfere destructively and therefore the radiation efficiency of the antenna is improved. An analysis of the radiation efficiency of two distant slots is presented in [44]. In Section 3.4, the analysis is extended to the case in which both slots and a patch are present. Second, the slots are used to improve the antenna bandwidth. The slots can be resonant in the operation band of the antenna because the reflector element compensates for the back radiation. As a result, the bandwidth is increased significantly since the antenna
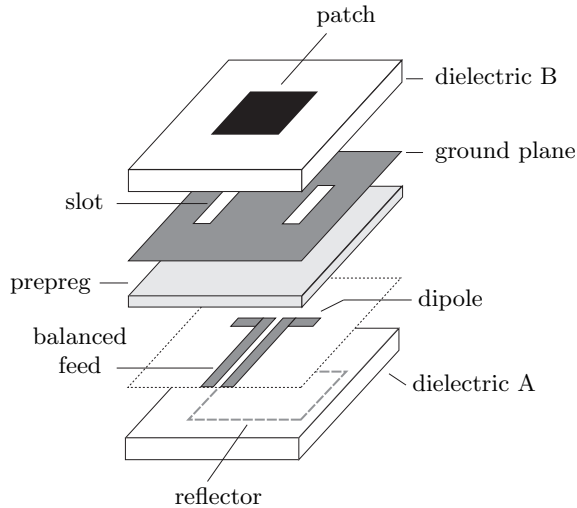
Figure 3.1: Geometry of the balanced-fed aperture-coupled patch with reflector element.

now has two resonant structures with slightly different resonance frequencies, i.e., the patch and both slots. An increase is observed from about 3% for the conventional single-element patch to more than 10% for this design.

The proposed antenna design combines the use of two separate slots with the use of the reflector element. The resulting design has a high radiation efficiency and a low back radiation. The geometry of the antenna element is shown in Fig. 3.1. The antenna can be realised from two PCB boards with metallization on both sides that are stacked with an adhesive (prepreg) in between. The important parameters in the design of the antenna are the length of the slots, the spacing between the slots, the length of the patch and the length of the dipole underneath the slots. The length of the slots and the length of the patch determine the operation bandwidth of the antenna. The spacing between the slots determines the radiation efficiency of the antenna and the coupling between the slots and the patch, as will be clarified in Section 3.4. The length of the dipole underneath the slots is important for the impedance matching of the antenna.

## 3.3   Modelling

The antenna is analysed with a method-of-moments approach (see Section 2.5). Both sub-domain and entire-domain basis functions are used to obtain a model with a limited number of unknowns. This reduces the computational effort that is needed to
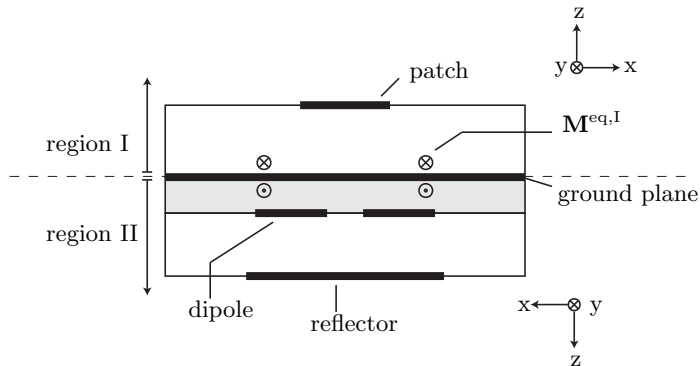
Figure 3.2: Equivalent problem of the balanced-fed aperture-coupled patch antenna.

analyse the performance of the antenna. The formulation relies on the Green's functions for layered media (Section 2.4) and does not include the effect of the finiteness of the dielectric layers. For normal board sizes, the finiteness of the dielectric does not affect the impedance matching of the antenna. At the edges of the finite dielectric, the surface waves scatter and distort the radiation pattern. As a result of this, a ripple will be superimposed on the radiation pattern [45]. This effect will be analysed separately and is discussed in Section 3.6.

The metal layers have been modelled as perfect electric conductors with zero thickness. This approximation reduces the complexity of the model since it treats the metal layers as two-dimensional structures. Therefore, less basis functions are needed to expand the current on these layers. The effect of finite conductivity and metal thickness is evaluated in Section 3.7.

The feed structure below the ground plane and the antenna structure above the ground plane can be analysed separately if Schelkunoff's equivalence principle is employed [20, Chapt. 6]. Equivalent magnetic-current densities $\mathbf{M}^{eq,i}$ are introduced to represent the aperture fields in region $i \in \{I, II\}$ [46]. The equivalent problem is shown in Fig. 3.2. Two local coordinate systems are introduced in region I and II such that both regions have the same coordinate system as the stratified medium that is introduced in Section 2.4.

The current densities on the metal layers are obtained from the electric field integral equation, whereas the equivalent magnetic-current densities are obtained from the magnetic field integral equation. Closed-form expressions for Green's functions in layered media have been derived in the spectral domain (Section 2.4) and these functions are employed to calculate the electric and magnetic fields in the two separate

regions. The boundary conditions for the BFACP antenna are formulated as

$$
\begin{aligned}
\mathbf{u}_z \times \mathbf{E}^{\mathrm{I}}(\mathbf{r}) &= 0 & \text{on patch,} \\
\mathbf{u}_z \times \mathbf{E}^{\mathrm{II}}(\mathbf{r}) &= 0 & \text{on dipole, reflector,} \\
\mathbf{u}_z \times \mathbf{H}^{\mathrm{I}}(\mathbf{r}) &= \mathbf{u}_z \times \mathbf{H}^{\mathrm{II}}(\mathbf{r}) & \text{on slots,} \\
\mathbf{u}_z \times \mathbf{E}^{\mathrm{I}}(\mathbf{r}) &= \mathbf{u}_z \times \mathbf{E}^{\mathrm{II}}(\mathbf{r}) & \text{on slots.}
\end{aligned}
\tag{3.1}
$$

The last boundary condition that imposes the continuity of the electric field in the slots can be solved directly in the equivalent problem of Fig. 3.2 by enforcing

$$
\mathbf{M}^{\mathrm{eq,I}}(\mathbf{r}) = -\mathbf{M}^{\mathrm{eq,II}}(\mathbf{r}) = \mathbf{M}^{\mathrm{eq}}(\mathbf{r}).
\tag{3.2}
$$

The other boundary conditions can be written in terms of the equivalent current densities on the slot and equivalent current densities on the patch (see Section 2.5). This can be expressed as

$$
\begin{aligned}
\mathbf{u}_z \times \mathbb{L}^{\mathrm{I}}\{\mathbf{J}^{\mathrm{eq,I}}, \mathbf{M}^{\mathrm{eq}}\}(\mathbf{r}) &= 0 & \text{on patch,} \\
\mathbf{u}_z \times \left[ \mathbf{E}^{\mathrm{inc}}(\mathbf{r}) + \mathbb{L}^{\mathrm{II}}\{\mathbf{J}^{\mathrm{eq,II}}, -\mathbf{M}^{\mathrm{eq}}\}(\mathbf{r}) \right] &= 0 & \text{on dipole, reflector,} \\
\mathbf{u}_z \times \mathbb{K}^{\mathrm{I}}\{\mathbf{J}^{\mathrm{eq,I}}, \mathbf{M}^{\mathrm{eq}}\}(\mathbf{r}) &= \mathbf{u}_z \times \mathbb{K}^{\mathrm{II}}\{\mathbf{J}^{\mathrm{eq,II}}, -\mathbf{M}^{\mathrm{eq}}\}(\mathbf{r}) & \text{on slots,}
\end{aligned}
\tag{3.3}
$$

Here $\mathbf{E}^{\mathrm{inc}}$ represents the incident field that is impressed on the dipole feed, $\mathbf{J}^{\mathrm{eq,I}}$ is the difference-current density [see (2.99)] on the patch, and $\mathbf{J}^{\mathrm{eq,II}}$ is the difference-current density on the dipole and the reflector. Again, the equivalent-current densities are approximated as

$$
\begin{aligned}
\mathbf{J}^{\mathrm{eq},i}(\mathbf{r}) &\approx \sum_{n=0}^{N^{J,i}-1} \kappa_n \mathbf{f}_n^i(\mathbf{r}), \\
\mathbf{M}^{\mathrm{eq}}(\mathbf{r}) &\approx \sum_{n=0}^{N^M-1} \varsigma_n \mathbf{h}_n(\mathbf{r}),
\end{aligned}
\tag{3.4}
$$

and the boundary conditions (3.3) are weighed with Galerkin testing functions. The resulting equations can be written in matrix notation as

$$
\begin{bmatrix}
\mathsf{Z}^{EJ,\mathrm{I}} & 0 & \mathsf{Z}^{EM,\mathrm{I}} \\
0 & \mathsf{Z}^{EJ,\mathrm{II}} & -\mathsf{Z}^{EM,\mathrm{II}} \\
\mathsf{Z}^{HJ,\mathrm{I}} & -\mathsf{Z}^{HJ,\mathrm{II}} & \mathsf{Z}^{HM,\mathrm{I}} + \mathsf{Z}^{HM,\mathrm{II}}
\end{bmatrix}
\begin{bmatrix}
\mathsf{I}^{J,\mathrm{I}} \\
\mathsf{I}^{J,\mathrm{II}} \\
\mathsf{I}^M
\end{bmatrix}
=
\begin{bmatrix}
0 \\
-\mathsf{V}^{\mathrm{II}} \\
0
\end{bmatrix},
\tag{3.5}
$$

where

$$
\begin{aligned}
\mathsf{V}_m^{\mathrm{II}} &= \left\langle \mathbf{f}_m^{\mathrm{II}}(\mathbf{r}), \mathbf{E}^{\mathrm{inc}}(\mathbf{r}) \right\rangle, \\
\mathsf{Z}_{mn}^{EJ,i} &= \left\langle \mathbf{f}_m^i(\mathbf{r}), \mathbb{L}^i\{\mathbf{f}_n^i, \mathbf{0}\}(\mathbf{r}) \right\rangle, \\
\mathsf{Z}_{mn}^{EM,i} &= \left\langle \mathbf{f}_m^i(\mathbf{r}), \mathbb{L}^i\{\mathbf{0}, \mathbf{h}_n\}(\mathbf{r}) \right\rangle, \\
\mathsf{Z}_{mn}^{HJ,i} &= \left\langle \mathbf{h}_m(\mathbf{r}), \mathbb{K}^i\{\mathbf{f}_n^i, \mathbf{0}\}(\mathbf{r}) \right\rangle, \\
\mathsf{Z}_{mn}^{HM,i} &= \left\langle \mathbf{h}_m(\mathbf{r}), \mathbb{K}^i\{\mathbf{0}, \mathbf{h}_n\}(\mathbf{r}) \right\rangle.
\end{aligned}
\tag{3.6}
$$

with $i \in \{\mathrm{I}, \mathrm{II}\}$.

The electric-current density on the patch and on the reflector element has been modelled with entire-domain expansion and testing functions, viz,

$$
\begin{aligned}
f_{n,x}^{\mathrm{ed}}(\mathbf{r}) &= \sin\Big(\frac{p(n)\pi}{l}[x + l/2]\Big) \cos\Big(\frac{q(n)\pi}{w}[y + w/2]\Big), \\
f_{n,y}^{\mathrm{ed}}(\mathbf{r}) &= \cos\Big(\frac{p(n)\pi}{l}[x + l/2]\Big) \sin\Big(\frac{q(n)\pi}{w}[y + w/2]\Big),
\end{aligned}
\tag{3.7}
$$

for $|x| < \frac{l}{2}$, $|y| < \frac{w}{2}$. Here, $l$ is the length of the patch/reflector, $w$ is the width of the patch/reflector, and $p$, $q$ are integer coefficients that determine the current distribution and depend on the index $n$. The basis functions for the $y$-directed equivalent magnetic currents are given by

$$
h_{n,y}(\mathbf{r}) = \cos\Big(\frac{p(n)\pi y}{l}\Big),
\tag{3.8}
$$

for $|y| < \frac{l}{2}$, $|\frac{s}{2} - |x|| < \frac{w}{2}$. Here, $l$ is the length of the slot, $w$ is the width of the slot, $s$ is the spacing between the two slots, and $p$ is an odd integer coefficient which determines the distribution of the magnetic current. The current on the dipole is modelled with rooftop basis functions, i.e.,

$$
f_{n,x}^{\mathrm{rt}}(\mathbf{r}) = 1 - \frac{1}{\Delta_x}|x - n\Delta_x|,
\tag{3.9}
$$

where $(n-1)\Delta_x < x < (n+1)\Delta_x$, $|y| < \frac{w}{2}$, and $\Delta_x = \frac{l}{N^{\mathrm{rt}}+1}$. Here, $l$ is the length of the dipole, $w$ is the width of the dipole, and $N^{\mathrm{rt}}$ is the number of rooftop functions on the dipole. Since the coplanar microstrip line that is connected to the dipole hardly contributes to the radiation of the structure it is not accounted for in the analysis. The dipole is excited with a delta-gap source in the middle, similar to the excitation of the dipole in the example of Section 2.10.

The derived model is used to analyze the antenna in detail and to investigate the radiation efficiency. To validate the model, a comparison has been made with commercial full-wave simulation software (Fig. 3.3). Our model uses 11 rooftop basis functions on the feed and 3 entire-domain basis functions per slot, 3 on the reflector and 3 on the patch, whereas the commercial software used 510 triangular basis functions. It is observed that the agreement is very good.

## 3.4 Radiation efficiency

As mentioned in the introduction of this chapter, the radiation efficiency of planar antennas is of concern. To evaluate the radiation efficiency, the different radiation mechanisms of aperture-coupled patch antennas should be considered. The dominant radiation mechanisms are shown in Fig. 3.4. The antenna radiates most of its power

| Element | Parameter | Value |
|---|---|---|
| dielectric A,B | $\varepsilon_r$ | 2.17 |
| | thickness | 0.25 mm |
| prepreg | $\varepsilon_r$ | 2.60 |
| | thickness | 0.11 mm |
| patch | length $l$ | 1.47 mm |
| | width $w$ | 1.45 mm |
| slots | length $l$ | 1.58 mm |
| | width $w$ | 0.23 mm |
| | spacing $s$ | 2.00 mm |
| reflector | length $l$ | 2.50 mm |
| | width $w$ | 1.80 mm |
| dipole | lenght $l$ | 2.31 mm |
| | width $w$ | 0.30 mm |

Table 3.1: Dimensions and dielectric properties of the antenna model.
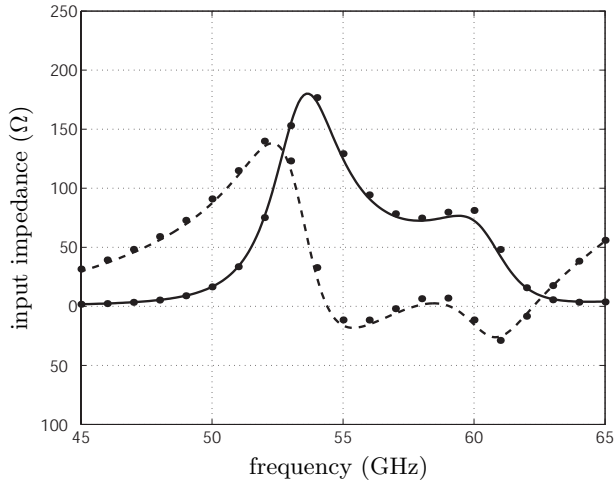


Figure 3.3:  Input impedance antenna.  Ansoft Designer:  $\mathsf{Re}\{Z_{\mathrm{in}}\}$ solid, $\mathsf{Im}\{Z_{\mathrm{in}}\}$ dashed. MoM model: dots. Dimensions in Table 3.1.
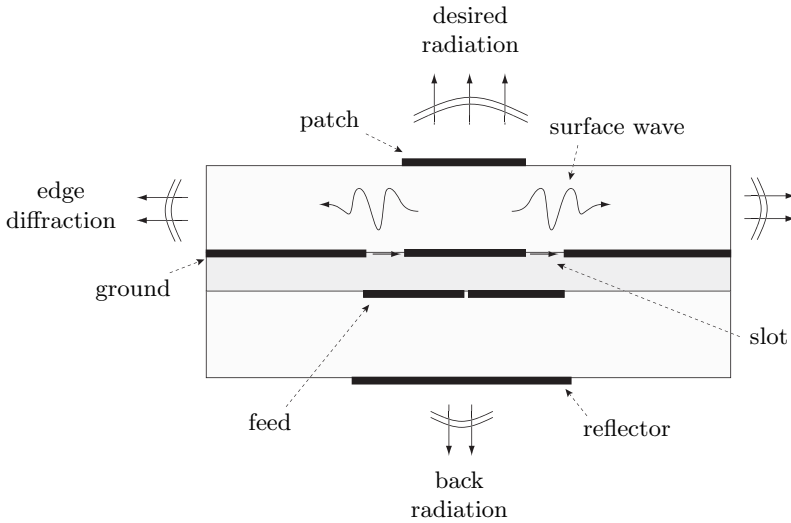
Figure 3.4: Radiation mechanisms of the balanced-fed aperture-coupled patch antenna.

in the upward direction. Next to this desired radiation, two important radiation contributions are present. First, the antenna radiates to the downward direction because slots are used to couple the feed with the antenna. These slots radiate both in the upward and downward direction. The downward radiation, or back radiation, is undesirable and should be minimised. Second, surface-waves are excited in the dielectric layers. The presence of surface waves can significantly reduce the radiation efficiency [34]. Moreover, these surface-wave scatter at the edges of the finite dielectric and this leads to unwanted radiation that could deteriorate the radiation pattern. Therefore, also the surface-wave excitation should be minimised.

The radiation efficiency and the surface-wave excitation is analyzed in region I (see Fig. 3.2), whereas the back radiation is considered in Section 3.5. The radiation efficiency is analysed for the case that the dielectric layers extend to infinity. In this analysis, the surface-waves do not scatter at the edges of the dielectric. However, it allows us to quantify the amount of power that is excited into surface waves. It is tried to minimise this amount such that the radiation efficiency is high and the effect of scattering from the edges of the dielectric is minimised. The effect of a finite dielectric on the radiation pattern is investigated separately in Section 3.6.

The amount of surface-wave power that is excited depends on the thickness and relative permittivity $\varepsilon_r$ of the dielectric [34]. For example, the radiation efficiency of an electric-current density source is shown in Fig. 3.5. Here, the radiation efficiency is represented versus dielectric thickness for two cases, i.e., $\varepsilon_r = 2$ and $\varepsilon_r = 4$. The $x$-directed electric-current density source is defined as an entire-domain basisfunction [(3.7); $p = 1, q = 0$] with length $l = \lambda_d/2$, width $w = \lambda_d/3$, and $\lambda_d = \lambda_0/\sqrt{\varepsilon_r}$, the wavelength in the dielectric. The current source is located on top of the dielectric
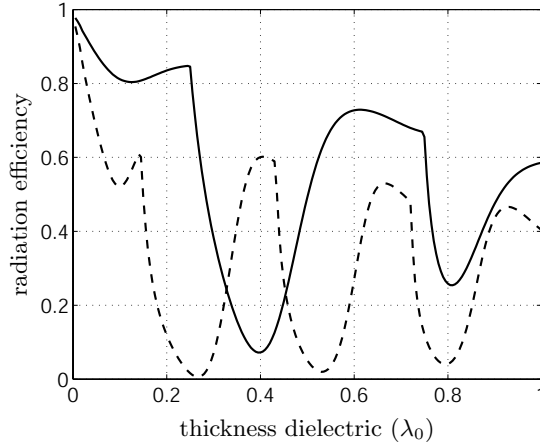
Figure 3.5: Radiation efficiency of an electric-current density source on top of a dielectric layer as a function of layer thickness. $\varepsilon_r = 2$ (solid), $\varepsilon_r = 4$ (dashed).

layer. The radiation efficiency is obtained from (2.73), (2.74), (2.90). Fig. 3.5 clearly shows the effect of increasing thickness on the radiation efficiency. For small dielectric thicknesses ($d < 0.05\lambda_0$) the surface-wave loss is proportional to the thickness and the radiation efficiency is the highest. This is the region of interest for the design of the BFACP antenna. For larger thicknesses (approx. $d > 0.25\lambda_d$), more surface-wave modes are excited and, as a result, the efficiency varies more rapidly. Fig. 3.5 also shows the effect of relative permittivity. The efficiency of the dielectric with $\varepsilon_r = 4$ is significantly lower than the efficiency of the dielectric with $\varepsilon_r = 2$. Therefore the BFACP antenna is designed on a dielectric substrate with a low dielectric constant, viz $\varepsilon_r = 2.2$.

The radiation efficiency of the BFACP antenna not only depends on the thickness and relative permittivity of the dielectric. The radiation efficiency of this antenna is also dependent on the slot spacing. To analyse this effect, the radiation efficiency in region I is considered. The equivalent magnetic current densities, that represent the aperture fields, are considered as the sources in region I. The current densities in both slots are equal owing to the fully symmetric antenna configuration. Consequently, the source power can be written as

$$
\begin{aligned}
P_s &= -\int_{S_s} \mathbf{M}^t(\mathbf{r}) \cdot \mathbf{H}^*(\mathbf{r}) \, dA \\
&= -\int_{S_s} \mathbf{M}^t(\mathbf{r}) \cdot \mathbf{H}^{t^*}(\mathbf{r}) \, dA - \int_{S_s} \mathbf{M}^t(\mathbf{r}) \cdot \mathbf{H}^{s^*}(\mathbf{r}) \, dA \\
&= P_s^{\text{slots}} + R_s^{\text{patch}},
\end{aligned}
\tag{3.10}
$$

with $S_s$ the surface area of the two slots, $\mathbf{M}^t$ the equivalent magnetic current of both

the slots, $\mathbf{H}^t$ the magnetic field resulting from the magnetic sources in absence of the patch and $\mathbf{H}^s$ the magnetic field resulting from the electric current on the patch. The power $P_s^{\text{slots}}$ can be interpreted as the power radiated by the two magnetic sources in absence of a patch element and $R_s^{\text{patch}}$ can be interpreted as the reaction (or coupling) between the magnetic sources and the scattered magnetic field $\mathbf{H}^s$ [47].

The magnetic fields $\mathbf{H}^t$ and $\mathbf{H}^s$ in (3.10) are found from the spectral Green's dyadics for multilayer dielectric substrates (Section 2.4). For example, the reaction between the magnetic source $\mathbf{M}^t$ and the electric current $\mathbf{J}^p$ on the patch is given by

$$R_s^{\text{patch}} = \frac{1}{4\pi^2} \int\limits_{k_\rho=0}^{\infty} \int\limits_{\psi=0}^{2\pi} \hat{\mathbf{M}}^t(-\mathbf{k}_t, z) \cdot$$
$$\left[\hat{\underline{\underline{\mathbf{G}}}}^{HJ}(\mathbf{k}_t, z, z_s) \cdot \hat{\mathbf{J}}^p(\mathbf{k}_t, z_s)\right]^* k_\rho d\psi dk_\rho. \tag{3.11}$$

It is observed that the terms that are needed to determine the source power have already been calculated in order to generate the interaction matrix that is needed for the method-of-moments analysis, owing to the use of Galerkin's method (see Section 3.3).

Part of the source power is dissipated in the dielectric, part is launched into surface waves and part is radiated. To determine the amount of power that is radiated ($P_s^{\text{rad}}$), the integral over $k_\rho$ in (3.11) is restricted to $k_\rho \in [0, k_0]$, with $k_0$ the propagation constant of free space (see Section 2.7). The power that is confined to the dielectric can now be determined as

$$P_s^{\text{diel}} = P_s - P_s^{\text{rad}}, \tag{3.12}$$

and the radiation efficiency in region I can be defined as

$$\eta^I = \frac{P_s^{\text{rad}}}{P_s}. \tag{3.13}$$

The radiation efficiency is a function of slot spacing since this spacing affects the amount of surface-wave power that is excited. The presence of the patch also has its influence on the total radiation efficiency. This is clarified in Fig. 3.6 that compares the radiation efficiency in region I to the case where the patch is absent as a function of slot spacing. In Fig. 3.6, the spacing is expressed in terms of the free-space wavelength ($\lambda_0$). The calculations have been performed with a single basis function on the slots ($p = 1$) and a single $x$-directed basis function on the patch ($p = 1, q = 0$). In Fig. 3.6 the dimensions of the slots and the patch are given in terms of the wavelength in the dielectric ($\lambda_d$). The radiation efficiency that is shown in Fig. 3.6 has an optimum around $s = \frac{\lambda_0}{2}$ because of the destructive interference of the surface waves that are excited by the slots. It is observed that the presence of the patch significantly increases the radiation efficiency for small slot spacings.

The spacing between the slots is also important for the operation bandwidth of the antenna. Both the slots and the patch should be used as radiating elements to increase the bandwidth. Hence, the spacing should be chosen such that both elements
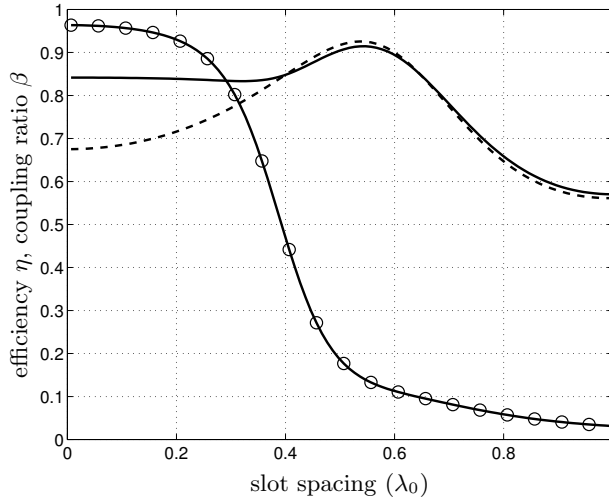
Figure 3.6: Efficiency of slots and patch (solid), efficiency of two slots (dash) and coupling ratio $\beta$ ($\circ$) as a function of slot spacing at 60 GHz.  Thickness dielectric $0.05\lambda_0$, $\varepsilon_r = 2.2$, $l = \lambda_d/2$, $w = \lambda_d/10$, $a = \lambda_d/2$, $b = \lambda_d/3$.

contribute to the radiated power.  To investigate the coupling between the slots and the patch the coupling ratio $\beta$, with reference to Eq. (3.10), is introduced as

$$\beta = \frac{R_s^{\text{patch}}}{P_s}. \tag{3.14}$$

The coupling ratio is shown as a function of slot spacing in Fig. 3.6 as well.  From the point of radiation efficiency, a slot spacing around $\frac{\lambda_0}{2}$ is optimal, but in that case the patch hardly contributes to the radiated power and the antenna bandwidth will not benefit from the patch element.  A slot spacing in the range from $0.3\lambda_0$ to $0.4\lambda_0$ has been used as a compromise between radiation efficiency and operation bandwidth.

## 3.5    Front-to-back ratio

As mentioned in Section 3.2, the front-to-back ratio should be given consideration in the design of aperture-coupled patch antennas.  Especially in this case, where resonating slots are used as radiating elements, the front-to-back ratio can become too low.  The front-to-back ratio $\kappa$ is defined as

$$\kappa = \frac{P^{\text{rad,I}}}{P^{\text{rad,II}}}, \tag{3.15}$$

where $P^{\text{rad},i}$ is the power that is radiated into region $i$ [see Section 2.7, (2.78)].  Note that in this definition the power in the upper and lower hemisphere is compared, instead of the ratio of the Poynting vector in the upward and downward direction.
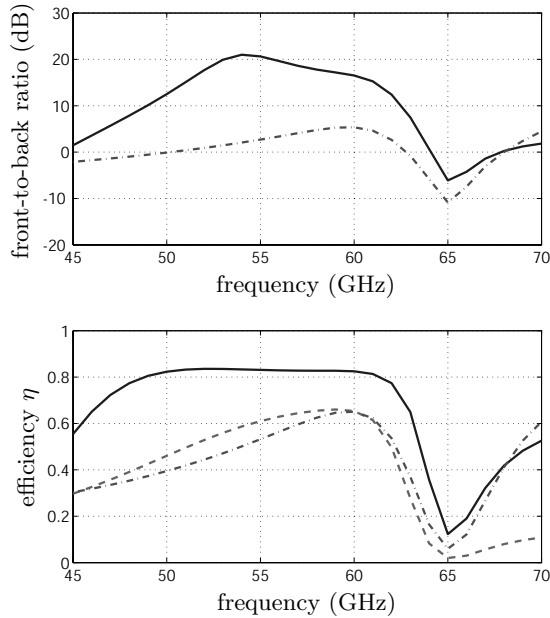
Figure 3.7: Front-to-back ratio and radiation efficiency of the antenna. Finite reflector element (solid), infinite reflector (dashed), no reflector (dash-dot). Dimensions as in Table 3.1.

For a practical design, a front-to-back ratio larger than 10 dB is required. To compensate for the back radiation of the slots, a reflecting metal plane at the back of the antenna can be added [48]. However, this will result in the excitation of a parallel-plate TEM mode between the metal plane and the ground plane and can seriously degrade the performance. Alternatively, a finite reflector element can be used [43], which is basically a large patch that covers the back of the two radiating slots. The reflector element can be placed at a distance much smaller than $\frac{\lambda_d}{4}$ from the slots, such that the losses in the lower dielectric are limited. In this section the performances of the infinite PEC plane and the finite reflector element are compared.

The overall efficiency $\eta$ of the antenna is defined as

$$\eta = \frac{P^{\mathrm{rad,I}}}{P^{\mathrm{I}} + P^{\mathrm{II}}}, \tag{3.16}$$

with $P^i$ the total power in region $i$ [see (2.77)]. The front-to-back ratio and the overall efficiency are compared for three cases, i.e., no reflector, an infinite reflector (infinite PEC plane) and a finite rectangular reflector. The front-to-back ratio of the infinite reflector is obviously infinite. The front-to-back ratio of the antenna with and without reflector element is shown in the upper graph of Fig. 3.7. The corresponding antenna
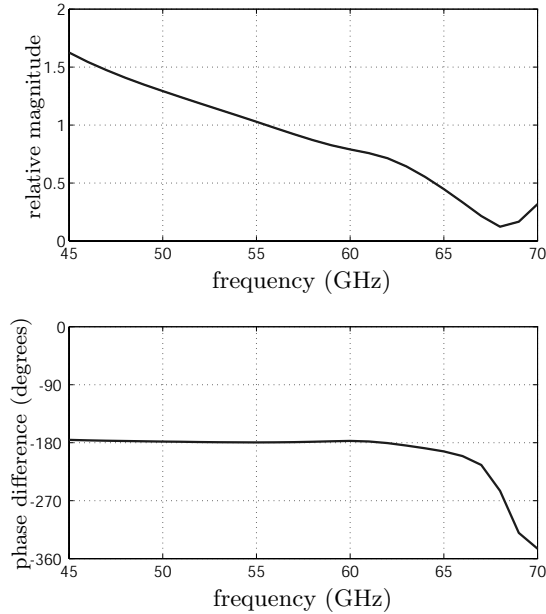
Figure 3.8: Relative magnitude and phase difference of the backward radiation of the reflector element. Dimensions as in Table 3.1.

dimensions are given in Table 3.1. The efficiency for all three setups is shown in the lower graph of Fig. 3.7. From this figure it is clearly seen that the reflector element gives a significant improvement in front-to-back ratio compared to the case where no reflector is present. More importantly, the radiation efficiency of the antenna with the finite reflector element is much larger than the radiation efficiency of the antenna with an infinite metal plane as reflector. If an infinite metal plane is used as reflector, parallel plate modes are supported in between the metal ground plane and the reflector plane. The power that is excited into these parallel plate modes significantly reduces the efficiency of the antenna.

The underlying physical principle of the finite reflector element is that it reradiates a field in the backward direction with the same magnitude, with 180 degrees phase difference compared to the fields that are radiated by the slots and the feed structure [43]. To clarify this effect, the magnitude and phase of the far-field contributions in the backward direction of the reflector have been plotted, relative to the magnitude and phase of the far field in the backward direction generated by the slots and feeding structure (Fig. 3.8). It is observed that the phase difference is indeed very close to the desired 180 degrees whereas the relative magnitude varies around one.
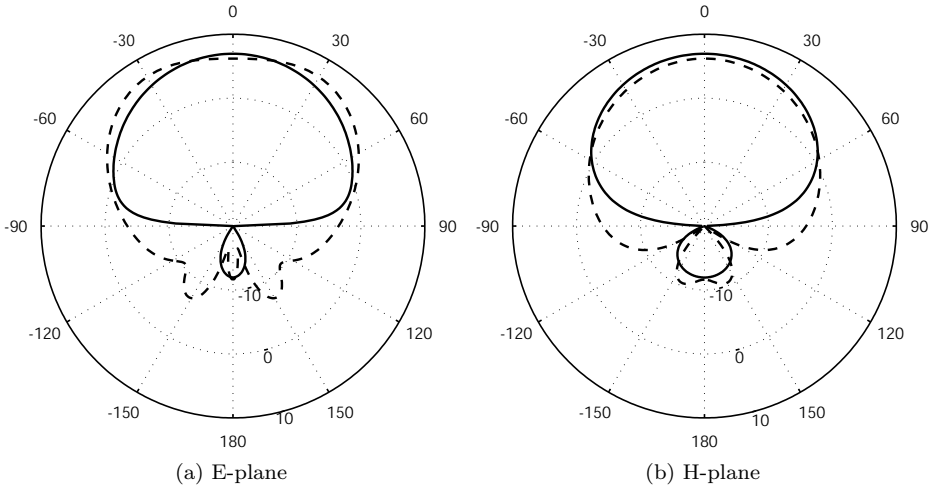
Figure 3.9: Gain of BFACP antenna in dBi. Frequency $f = 58$ GHz. Planar simulation [Spark] (solid), 3D simulation [CST Microwave Studio] (dashed).

## 3.6   Radiation pattern

The BFACP antenna has a radiation pattern that is very similar to other patch-type antennas. The main lobe has a cosine-shaped beam with a -3dB beam-width of approximately $\pm 45°$. Because of the aperture coupling and the antenna feed, there is some radiation to the back as well, although it is tried to minimise this radiation with the reflector element.

To investigate the effect of the surface-wave scattering at the edges of the dielectric, the simulated radiation patterns for an infinite and finite dielectric are compared. The radiation pattern for the infinite case has been analysed by our MoM implementation (Section 3.3), whereas the radiation pattern for the finite dielectric layers has been analysed with CST Microwave Studio. In Fig. 3.9, the radiation pattern is shown for the finite and infinite dielectric. Here, the size of the dielectric layers is chosen arbitrarily as $10 \times 10$ mm.

When the dielectric layers extend to infinity, no scattering of the surface waves occurs, whereas with a finite dielectric, the radiation pattern shows a ripple due to the contributions of the radiating edges of the dielectric [45]. In Fig. 3.9, the amplitude of this ripple is approximately 2 dB on the main lobe of the radiation pattern. The antenna on the finite dielectric also shows increased radiation at the backside and near the angles $\theta = \pm 90°$.

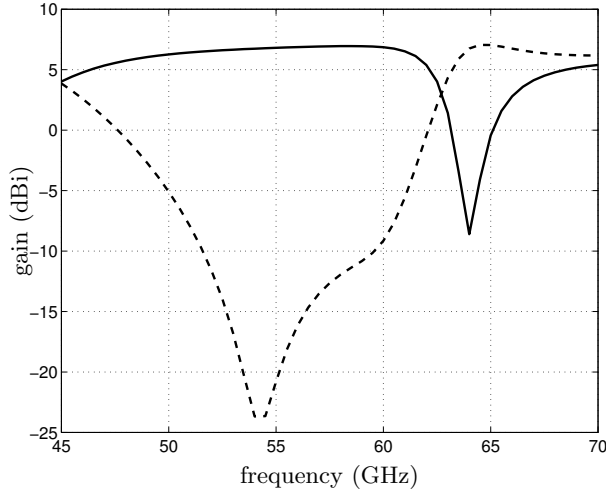The gain and directivity of the antenna as a function of frequency is shown in Fig. 3.10

Figure 3.10: Gain of BFACP antenna at $\theta = 0°$ (solid) and $\theta = 180°$ (dashed).

for both the upward ($\theta = 0$) and downward ($\theta = \pi$) direction. It is observed that the back radiation is less than -10 dBi in the frequency range from 52 to 59 GHz. In this region the broadside gain of the antenna is larger than 6.5 dBi. For higher frequencies, the reflector element starts to contribute to the back radiation and the dominant radiation is directed backwards. Therefore, this region of operation should be avoided.

## 3.7   Effect of finite conductivity and metal thickness

The model that is introduced in Section 3.3 assumes that the metal can be approximated as a perfect electric conductor with zero thickness. In this section, the effects of finite conductivity and metal thickness are analysed to verify the validity range of this assumption.

The antenna is modelled with copper in Ansoft Designer to investigate the effect of finite conductivity and these results are compared with the results of the PEC antenna. The input impedance, reflection coefficient, directivity and gain of both antennas were almost identical and therefore it is concluded that the effect of finite conductivity is not important as long as well-conducting materials are used like copper, silver or gold. Note that in this comparison, the balanced feed line of the antenna has not been incorporated. A long feed line with finite conductivity introduces additional losses that should be accounted for. However, the use of metal with a finite conductivity in the antenna itself does not affect the input impedance significantly.
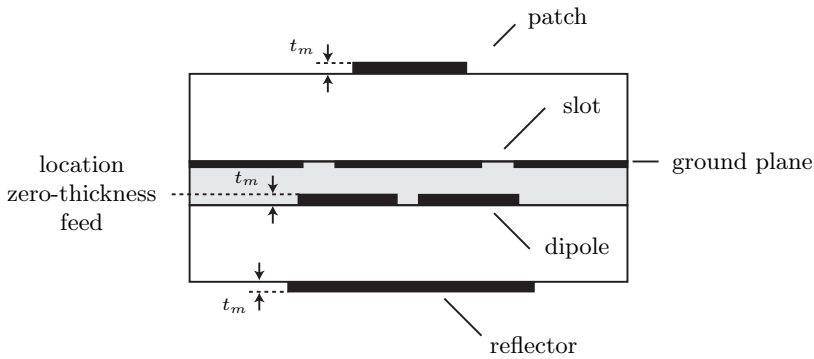
Figure 3.11: Layout of BFACP antenna including metal thickness.

The input impedance of the antenna is sensitive for changes in metal thickness $t_m$. Especially the thickness of the feed has an impact on the input impedance and therefore also on the reflection coefficient of the antenna. The reflection coefficient $S_{11}$ is related to the input impedance as

$$S_{11} = \frac{Z_{\text{in}} - Z_0}{Z_{\text{in}} + Z_0},\tag{3.17}$$

where $Z_0$ is the characteristic impedance of the transmission line that is connected to the antenna. Here, the balanced feed should be designed for a characteristic impedance $Z_0 = 100\ \Omega$. The reflection coefficient is compared for different thicknesses of the metal layers, where the thickness is defined in Fig. 3.11. To obtain a fair comparison, the thickness of the ground plane is not considered, since it is not incorporated in the models. Fig. 3.12 shows the results for metal thicknesses of 0, 9, and 25 $\mu$m. It is shown that the metal thickness affects the reflection coefficient and therefore the assumption that the metal can be modelled as if it has zero thickness is not always valid.

Close examination of the influence of metal thickness has shown that the thickness of the antenna feed has a dominant effect on the reflection coefficient. In comparison, the finite thicknesses of the reflector, ground plane, and patch do not affect the reflection coefficient much. From this observation, it is tried to improve the accuracy of the Spark model by positioning the zero-thickness feed layer of this model at the top of the actual feed (see Fig. 3.11). Since the field is mostly confined between the top of the feed and the bottom of the ground plane, the currents on the top of the feed are the strongest. Therefore, this feed position improves the accuracy of the model. The adjusted feed position is implemented in Spark and the results are compared with the finite-thickness results of Ansoft Designer in Fig. 3.12. It is observed that the adjusted feed position of the zero-thickness feed improves the accuracy of the Spark model indeed.
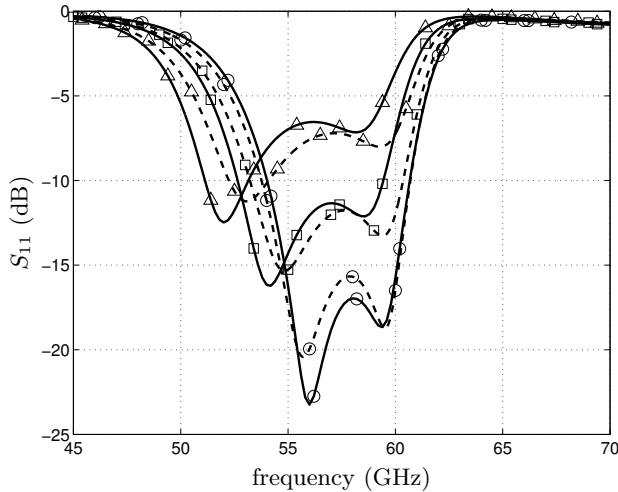
Figure 3.12: Reflection coefficient of the BFACP antenna for different metal thicknesses. Finite-thickness simulations [Ansoft Designer] (solid), zero-thickness simulation [Spark] (dashed). Thicknesses: 0 $\mu$m ($\circ$), 9 $\mu$m ($\square$), 25 $\mu$m ($\triangle$).

## 3.8   Polarisation diversity

The BFACP antenna can be extended to support dual polarisation or circular polarisation by adding two more slots (Fig. 3.13). In this way, the advantages of the linearly polarised antenna are maintained while the flexibility of polarisation diversity is added. However, the design of the feed network becomes more involved. The antenna now has four slots and opposite slots need to be excited simultaneously. Therefore it becomes complicated to design a feed network on a single metal layer. One could use more metal layers to design the feed network, but then the use of vias is required (see Fig. 3.13). Especially at millimeter-wave frequencies, the use of vias should be avoided since they introduce mismatch and additional losses. Therefore, an alternative feed network is designed that uses a single metal layer and that supports polarisation diversity.

The feed of the antenna is a coplanar microstrip line that supports two propagating modes, i.e., the odd and even mode. Both modes are used in the feed network in a way that each mode excites a specific polarisation. The coplanar microstrip line is split into two separate microstrip lines that are fed to branch-line couplers (Fig. 3.14) [49]. A branch-line coupler has two inputs and two outputs. The output signals can be controlled by the phase and amplitude of the input signals. When the input signals have a phase difference of 90 degrees and equal amplitude, only one output is active while the other output is isolated. This property is employed to obtain polarisation selectivity. In this setup, an RF source is needed that is able to generate both an even-mode and an odd-mode signal simultaneously.
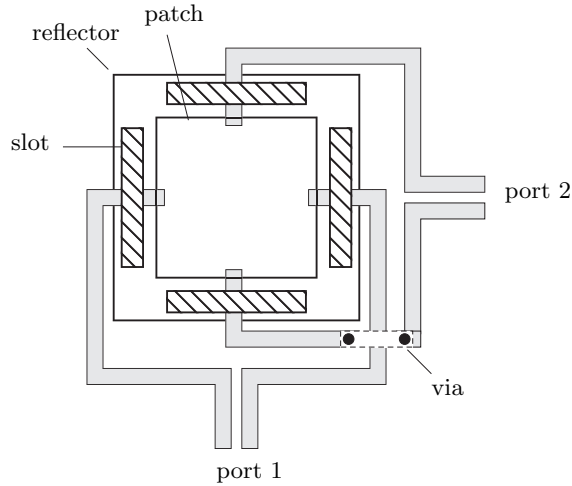
Figure 3.13: Top view of the dual-polarised BFACP antenna with two separate feed networks.

The feed network of the polarisation diversity antenna with branch-line couplers is shown in Fig. 3.15. It consists of two branch-line couplers that select which slots of the patch antenna are excited. The feed-line length from branch-line coupler to slot should be the same for opposite slots. If the antenna is operated in the even mode (Fig. 3.15), one linear polarisation is active while the other linear polarisation is active in the odd mode (Fig. 3.16). The polarisation selectivity is demonstrated in Fig. 3.17, which shows the co- and cross-polarisation of the dual-polarised antenna for even- and odd-mode excitation. These simulations have been performed with Ansoft Designer. It is observed that the cross-polarisation level is more than 20 dB lower that the co-polarisation level in the upper hemisphere. This demonstrates the ability of the antenna to switch polarisation, depending on the mode excitation.

The far-field of the antenna can be related to the mode excitation as

$$\begin{aligned} E_\nu &\sim \mathsf{Re}\{a^{\mathrm{even}}e^{j\omega t}\}, \\ E_\tau &\sim \mathsf{Re}\{a^{\mathrm{odd}}e^{j\omega t}\}, \end{aligned} \tag{3.18}$$

where $E_\nu$ is the $\nu$-directed far-field at broadside ($z$-direction), $E_\tau$ is the $\tau$-directed field at broadside, $a^{\mathrm{even}}$ is the amplitude of the even mode, $a^{\mathrm{odd}}$ is the amplitude of the odd mode, $\omega$ is the radial frequency and $t$ is the time variable. The $\nu$ and $\tau$ directions are indicated in Fig. 3.15.

The excitation of the even and odd mode simultaneously results in the excitation of the two port lines with a specific amplitude and phase-difference. These excitations are

$$\begin{aligned} s_1 &= \mathsf{Re}\{(a^{\mathrm{even}} + a^{\mathrm{odd}})e^{j\omega t}\}, \\ s_2 &= \mathsf{Re}\{(a^{\mathrm{even}} - a^{\mathrm{odd}})e^{j\omega t}\}. \end{aligned} \tag{3.19}$$
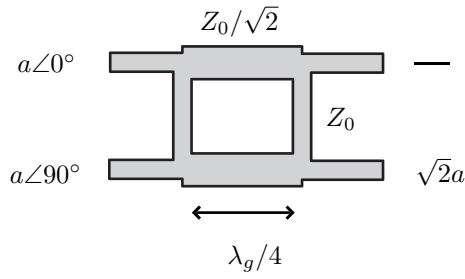
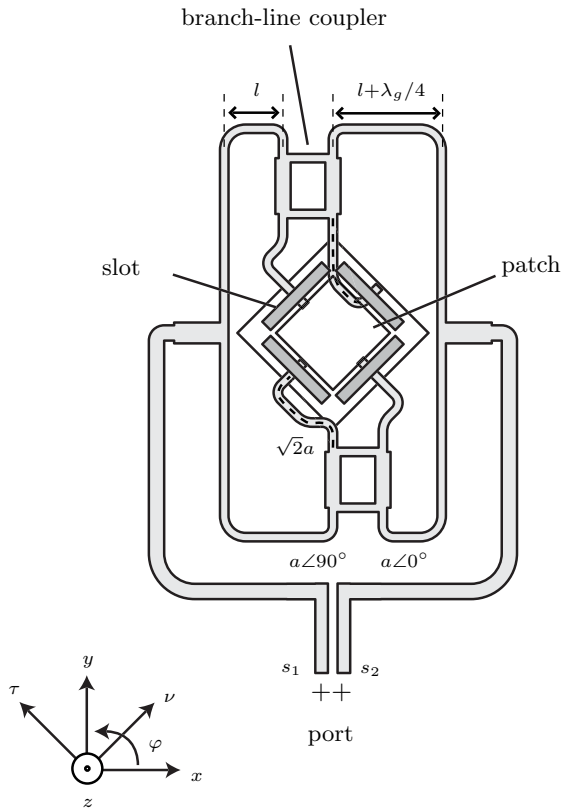Figure 3.14: Layout of a branch-line coupler.



Figure 3.15: Top view of the dual-polarised BFACP antenna with branch-line couplers in even-mode operation. The dashed lines indicate the active feed lines.
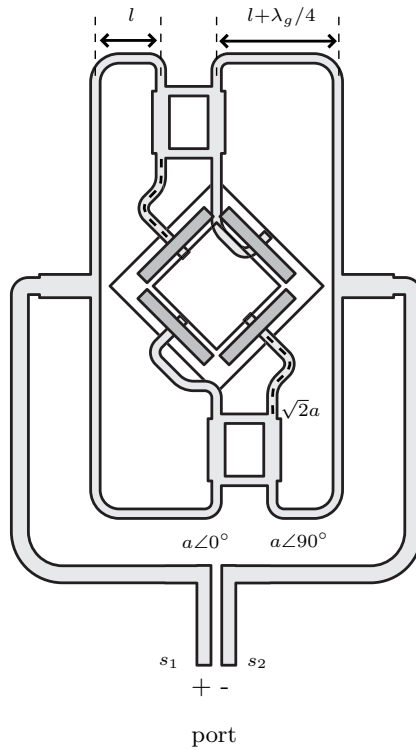
Figure 3.16: Top view of the dual-polarised BFACP antenna with branch-line couplers in odd-mode operation. The dashed lines indicate the active feed lines.
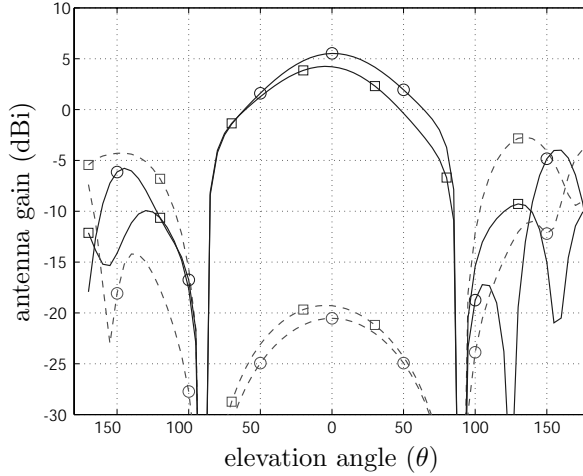
Figure 3.17: Co- (solid) and cross polarisation (dashed) of the dual-polarised antenna at $f = 60$ GHz. Even-mode excitation, $\varphi = 45°$ ($\square$), odd-mode excitation, $\varphi = 135°$ ($\circ$).

| even mode | odd mode | $s_1$ | $s_2$ | polarisation |
|:---:|:---:|:---:|:---:|:---:|
| $a\angle 0°$ | $0$ | $s\angle 0°$ | $s\angle 0°$ | linear, $\varphi = 45°$ |
| $0$ | $a\angle 0°$ | $s\angle 0°$ | $s\angle 180°$ | linear, $\varphi = 135°$ |
| $a\angle 0°$ | $a\angle 0°$ | $2s$ | $0$ | linear, $\varphi = 90°$ |
| $a\angle 0°$ | $a\angle 90°$ | $s\angle 0°$ | $s\angle 90°$ | right-hand circular |
| $a\angle 90°$ | $a\angle 0°$ | $s\angle 90°$ | $s\angle 0°$ | left-hand circular |

Table 3.2: Relation between mode excitation and polarisation.

An arbitrary linear polarisation can be realized by exciting both modes in phase simultaneously. Circular or elliptical polarisation can be obtained when both modes are excited with a phase difference of 90 degrees. Some examples for the relation between mode excitation and polarisation are listed in Table 3.2.

## 3.9  Conclusions

In this chapter, the requirements on the antenna element have been discussed and a BFACP antenna design has been proposed that is tailored for broadband millimeter-wave communication. It can be realised in low-cost PCB technology, has a high radiation efficiency and can be integrated with balanced RF electronics. It has been shown that the antenna can be efficiently modelled with a limited number of basis

functions. The influence of slot spacing on radiation efficiency has been analysed and the performance of the reflector element has been investigated. Moreover, an extension of the BFACP antenna has been presented to support dual polarisation and circular polarisation.

In the next chapter, the antenna designs will be validated through measurements. The operation bandwidth and the radiation pattern are measured to validate the performance of the BFACP antennas. Further optimisation of the antennas is discussed in Chapter 5. Hereafter, the optimised BFACP antenna elements are placed in array configurations that enable beam-forming (see Chapter 6).

# Measurement and verification

## 4.1 Introduction

The characterisation of antennas and RF structures at millimeter-wave frequencies is a delicate procedure. As the frequency increases, the size of the RF structures decreases and it becomes more difficult to characterise these structures without influencing the measurement with the measurement equipment itself. Additional effort is needed to create an interconnect that is reliable and that can be characterised properly. In this respect, also the repeatability of the measurement is important. In this chapter, a measurement procedure is described for the characterisation of planar antennas in the millimeter-wave frequency band. This procedure is used to characterise the antennas described in Chapter 3.

An approach is presented that allows for the accurate characterisation of the performance of planar antennas that operate in the millimeter-wave frequency band. In order to solve part of the interconnection problems, RF probes have been used such that a well-defined interconnection between the antenna under test (AUT) and the measurement setup can be realised. These RF probes are normally used for the characterisation of devices on a semiconductor wafer. Here, they are used to characterise antennas that can be realised in any planar manufacturing technology. RF probes have the advantage that they are reusable and that they can be calibrated very accurately.

patch layer

dielectric B

ground layer
prepreg
feed layer

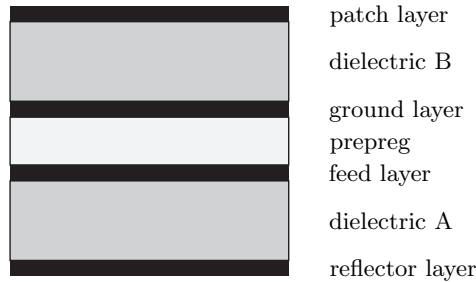dielectric A

reflector layer

Figure 4.1: PCB stack that is used for the AUT and the measurement setup.

A completely planar transition is designed to transform the coplanar waveguide transmission line that is required by the RF probe to a microstrip transmission line that is used by the antenna structure. It is shown that this transition can be de-embedded from the measurements. A measurement setup has been realised to measure the far-field radiation pattern as well. It is based on a measurement setup that was proposed by [50] and is optimised such that the setup does not affect the measured radiation pattern. It allows the measurement of the far-field radiation pattern in the whole upper hemisphere.

## 4.2   AUT and measurement setup

The antenna is realised in a standard printed circuit-board (PCB) manufacturing technology from two dielectric boards that are stacked with a prepreg layer in between (Fig. 4.1). The prepreg layer acts as adhesive between the two dielectric boards. The feed lines are embedded within the stack. Therefore an open cavity has been made such that the RF probe can be landed on the feed lines. The cavity has been realised by creating a hole in the upper dielectric board and in the prepreg board before the boards are laminated together.

A schematic layout of the AUT and the measurement setup is shown in Fig. 4.2. Since the antenna has a balanced feed whereas the RF probe is unbalanced, a balun is required which transforms the balanced coplanar microstrip line to an unbalanced microstrip line and vice versa. The RF probe has to land on a coplanar waveguide (CPW) transmission line. In order to connect to the balun, a transition from CPW to microstrip (MS) is needed. This transition is realised without the use of vias to avoid manufacturing uncertainties that are involved with the realisation of vias. Two quarter-wave stubs are attached to both ground lines of the CPW to provide a virtual ground at the end of the CPW line, following an idea by Raskin et al. [51].
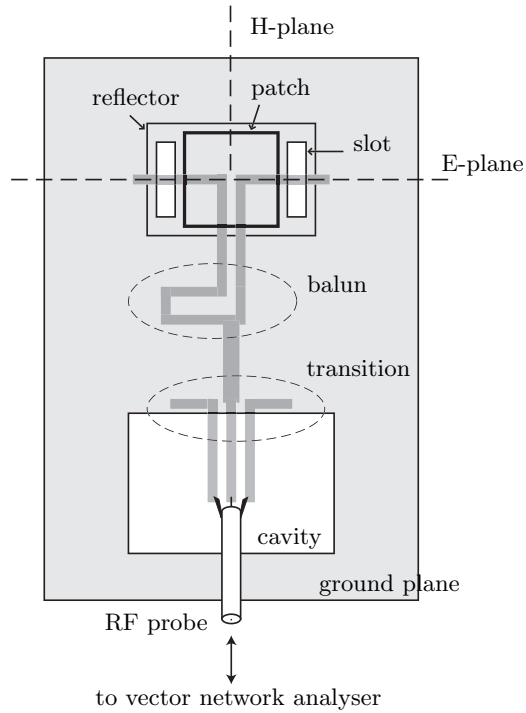
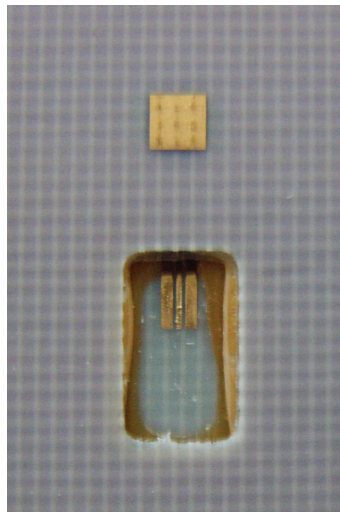Figure 4.2: Schematic layout of AUT and measurement setup.



Figure 4.3: Photograph of realised AUT and measurement setup. Dimensions of the PCB board are 9×13 mm.
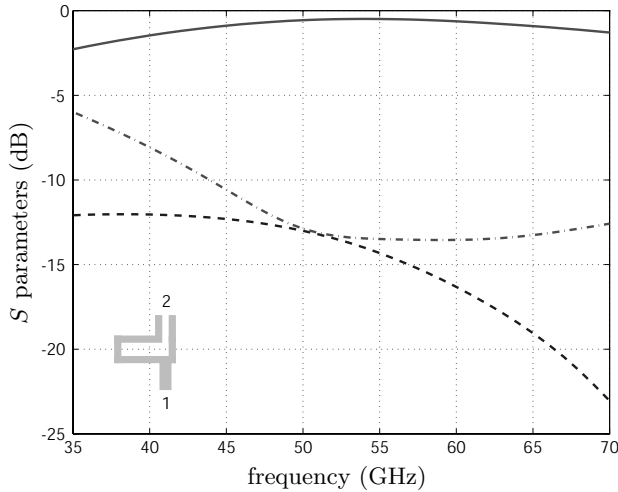
Figure 4.4: Simulated scattering parameters of the balun. $S_{11}$ MS (dashed), $S_{12}$ MS - CPS [odd mode] (solid), $S_{22}$ CPS [odd mode] (dash-dot).

### 4.2.1   Balun design

The balun design is quite straightforward. The microstrip line connects to two lines that have a length difference which corresponds to 180 degrees of phase difference at 60 GHz. These two lines are immediately connected to the coplanar microstrip (CPS) transmission line that is used to feed the antenna. The CPS transmission line can support two modes, viz, the odd mode and the even mode. The balun should excite the odd mode for the antenna to work properly. Simulation results shows that this is the case indeed and that the balun has a good performance over a wide frequency band (Fig. 4.4). These simulation results have been obtained with Ansoft Designer.

### 4.2.2   De-embedding of the CPW-MS transition

The transition from CPW to MS is designed in CST Microwave Studio (Fig. 4.5). The microstrip line is designed for a characteristic impedance of 50 Ω. However, the minimum track width and spacing of the used technology is 100 $\mu$m and therefore, it is not possible to design a CPW transmission line with a characteristic impedance of 50 Ω. Instead, a CPW transmission line is designed with a characteristic impedance of 100 Ω. The length of this transmission line is half a guided wavelength at 60 GHz such that, effectively, no impedance transform occurs. A challenge in the measurement of the reflection coefficient of the antenna is to de-embed the CPW to MS transition from the measurements. For this purpose, additional structures have been realised on the antenna board. Three different types of transitions in a back-to-back configuration
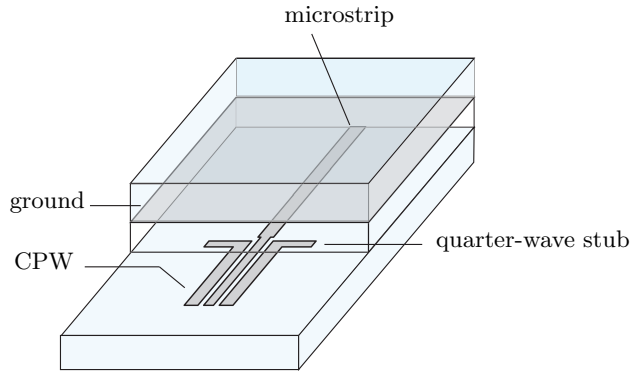
Figure 4.5: Layout of the CPW to MS transition.
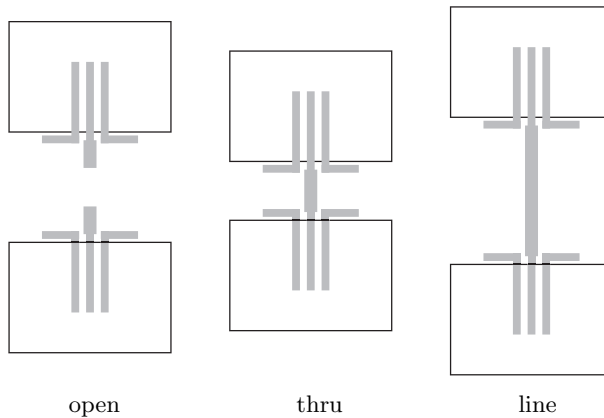


open      thru      line

Figure 4.6: Open, thru and line configurations for characterisation of the CPW to MS transition.

have been realised, i.e., an open, thru and line configuration (Fig. 4.6). In this way, all the S-parameters of the transition can be characterised following a thru-reflect-line (TRL) calibration procedure [49].

The measured and simulated performance of the transition is shown in Fig 4.7. The simulated results have been obtained with CST Microwave Studio. Some difference between the measured and simulated curves are observed. This is probably introduced by manufacturing discrepancies since the tolerance on the cavity size is approximately $\pm0.1$ mm. However, it is important to stress that although the transitions do not exactly have the expected performance, it is still possible to accurately de-embed the effect of the transition from the measurements, since the de-embedding procedure relies on the measured transition only.
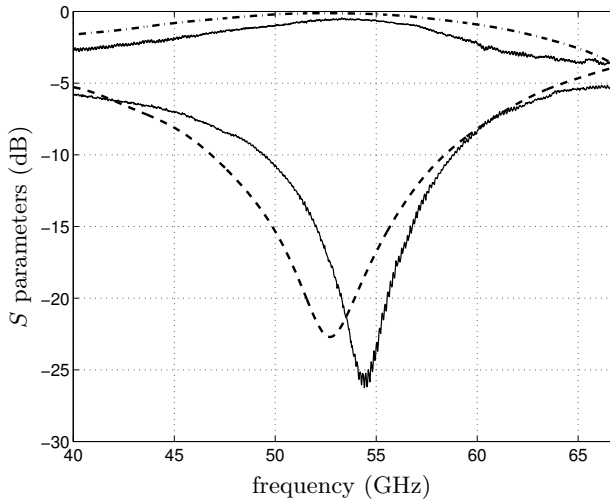
Figure 4.7: Scattering parameters of the de-embedded CPW-MS transition. Measurement (solid), simulation $S_{11}$ (dashed), simulation $S_{21}$ (dash-dot).

### 4.2.3   Reflection coefficient BFACP antenna and balun

The measured and simulated reflection coefficients of the BFACP antenna and balun after de-embedding are shown in Figure 4.8. For comparison, the antenna structure including balun is simulated with Spark and with Ansoft Designer. In Spark, the metal structures are modelled as PEC with zero thickness. In Ansoft Designer, the metal structures are modelled as copper with a conductivity $\sigma = 5.8e7$ S/m and a thickness $t_m = 9$ $\mu$m. Since it is difficult to accurately determine the loss tangent of the dielectric materials, dielectric losses are not accounted for. It is expected that this simplification does not influence the performance much since the teflon-based materials that have been used are known to have very little loss.

To obtain the reflection coefficient, the current-density distribution on the antenna feed and the balun is computed with Spark. For this computation, a rectangular mesh is employed with rooftop basis functions. A travelling-wave current-density source (see Section 2.9.2) is used for the excitation of the microstrip line of the balun. The mesh and the computed current is shown in Fig. 4.9.

Comparison of the measured and simulated reflection-coefficient curves in Fig. 4.8 shows reasonably good agreement. The resonances of the slots and the patch can be recognised in all curves. The simulated -10 dB bandwidth is 55.3-61.4 GHz (10.5%) in Spark, 53.5-60.5 GHz (12%) in Ansoft Designer and 51.7-60.0 GHz (15%) in the measurements. The simulated reflection-coefficient curves are shifted in frequency compared to the measured curve. This is partly because of the zero-thickness assumption of the metal feed layer that is employed in Spark (see also Section 3.7).
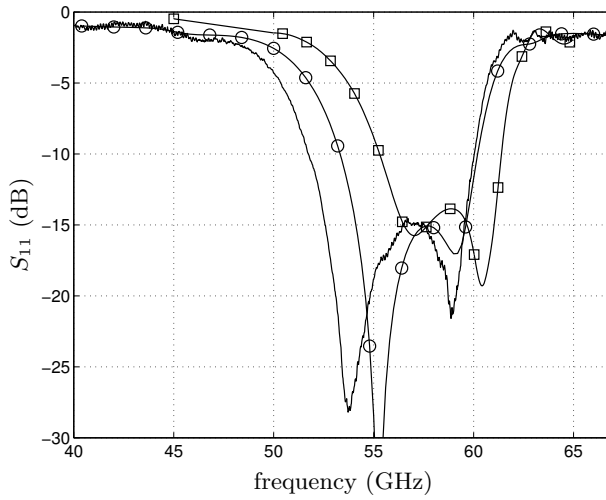
Figure 4.8: Reflection coefficient of the combined antenna and balun. Measurement (solid), Spark ($\square$), Ansoft Designer ($\circ$).
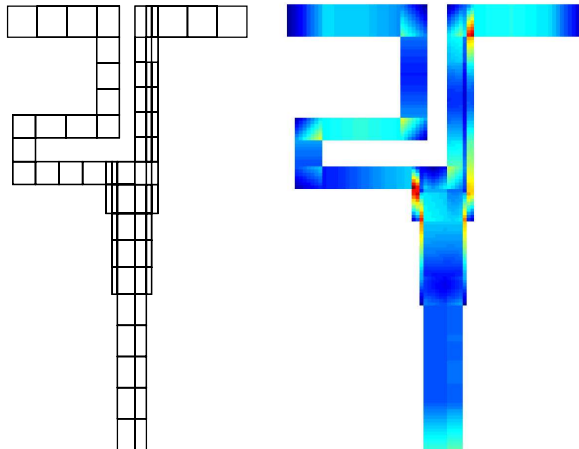


Figure 4.9: Mesh (left) and simulated current distribution (right) of antenna feed and balun. $f = 54$ GHz.

The metal thickness is accounted for in the simulations with Ansoft Designer and it is observed in Fig. 4.8 that this reduces the difference in frequency shift between the measured and simulated reflection-coefficient curve. However, some differences still remain. These differences are attributed to etching, alignment and material tolerances. The effects of these tolerances are analysed and discussed in Chapter 5 as well.

## 4.3    Radiation pattern

### 4.3.1    Measurement setup

To determine the radiation pattern of the antenna, a far-field measurement setup has been built (Figs. 4.10, 4.11). It is based on the setup that was proposed in [50], which measures the radiation pattern of patch antennas that operate in the frequency range around 24 GHz. In [50], the radiation pattern has been measured above a probe station, which can introduce a lot of unwanted scattering due to the metal structure of the probe station.

Our setup is tailored to the measurement of the radiation pattern of millimeter-wave antennas and antenna arrays. It is tried to minimise the scattering of the measurement setup itself. The measurement setup has a metal base which is covered with absorbing material. The antenna is placed on a perspex table and a rigid perspex arm is used that supports the measurement probe (see Fig. 4.10). This light-weight arm can be rotated in elevation by a stepper motor and can be placed at different azimuth angles to be able to measure the full hemisphere. An open-ended waveguide is attached to the end of the perspex arm to measure the far-field radiation. The antenna is connected with an RF probe. In order to land this RF probe on the contact pads of the antenna, a micro positioner is needed. This positioner is placed at the back of the metal base to reduce the scattering and has a perspex bar that moves through a hole in the metal base.

To position the center of the antenna in the rotational center of the measurement arm, a digital video camera is used that can be placed at a fixed position above the AUT. Since the camera has a fixed position, the rotational center of the measurement setup can be displayed on the camera view and the antenna under test can be moved such that its center and the rotational center of the measurement setup coincide.

The open-ended waveguide can be positioned in three different rotations (0, 45, 90 degrees) with respect to the perspex arm. In this way, the co- and cross-polar radiation patterns can be determined in the principle $E$ plane and $H$ plane and in the diagonal plane with a measurement of the magnitude of the radiated field only. For these measurements, no phase information is needed. To determine the radiated field in the
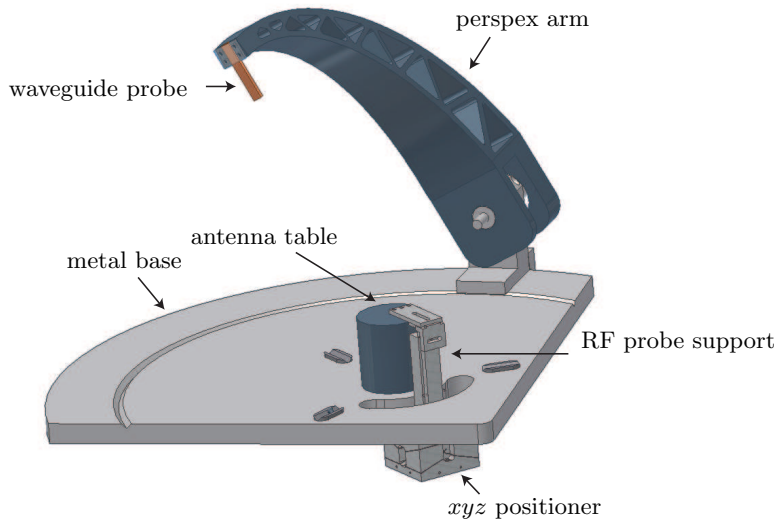
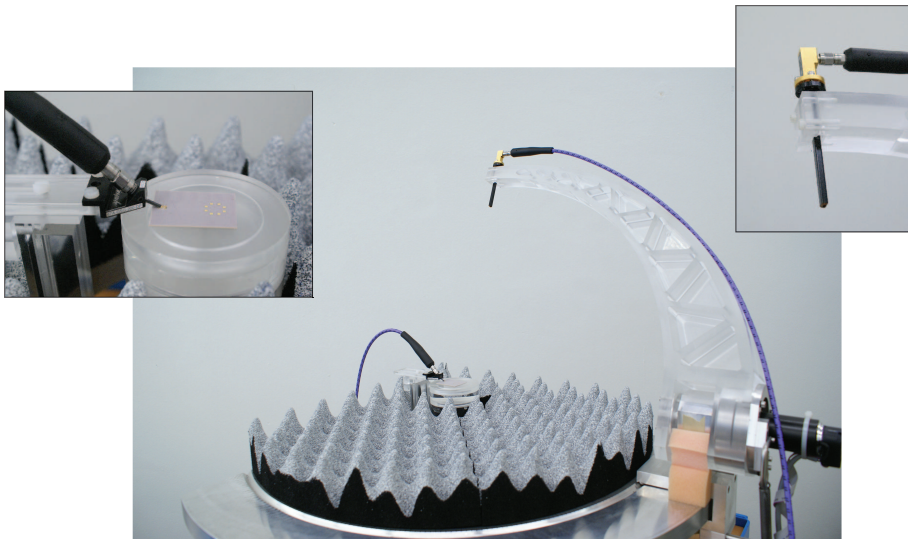Figure 4.10: Schematic layout of far-field radiation pattern measurement setup.



Figure 4.11: Photograph of far-field radiation pattern measurement setup. Left inset: antenna table with RF probe and AUT. Right inset: open-ended waveguide attached to the rotating perspex arm.

whole upper hemisphere, measurements of the magnitude and phase of the radiated field are required in two different polarisations.

The far-field distance $r_{\mathrm{ff}}$ can be estimated as (see e.g. [10])

$$r_{\mathrm{ff}} = \frac{2D^2}{\lambda},\tag{4.1}$$

with $D$ the largest dimension of the antenna and $\lambda$ the free-space wavelength. The far-field region of regular antennas in the millimeter-wave frequency bands starts at a distance in the order of tens of centimeters from the antenna. Therefore the setup that we propose is very much suited for such measurements, since it is possible to characterise the antenna with a setup which has a limited size and which allows for a simple interconnection with the antenna under test. In our setup, the open-ended waveguide is placed at a distance of about $r_{\mathrm{ff}} = 30$ cm from the AUT. This implies a maximum dimension of the AUT of about 27 mm for an operation frequency of 60 GHz [see (4.1)].

### 4.3.2   Gain calibration

A schematic layout of the measurement setup is shown in Fig. 4.12. To determine the gain of the AUT, the gain of the open-ended waveguide should be specified as well as the path loss between the AUT and the open-ended waveguide. Moreover, the losses in the coax cables, the RF probe, and the waveguide-to-coax transition need to be characterised.

The loss in coax 1 and in the RF probe can be determined by a back-to-back measurement of two coax cables and two RF probes. Assuming the loss in both coax cables and both RF probes is comparable, a through measurement is sufficient to characterise the loss in one cable and one probe. However, if this assumption cannot be made, a full two-port characterisation is required to determine the loss of coax 1 and the RF probe. The loss in the waveguide-to-coax transition and the loss in coax 2 can be determined similarly with a measurement of the cables and two waveguide-to-coax transitions.

If we compensate for the losses in the coax cables, the RF probe and the waveguide-to-coax transition, the ratio of received and transmitted power can be obtained from Friis' equation as

$$\frac{P_r}{P_t} = \frac{G_r G_t \lambda^2}{(4\pi |\mathbf{r}|)^2},\tag{4.2}$$

where $G_r$ is the gain of the receive antenna (open-ended waveguide), $G_t$ is the gain of the transmit antenna (AUT), $\lambda$ is the free-space wavelength, and $|\mathbf{r}|$ is the distance between the transmit and receive antenna. To determine the gain of the open-ended
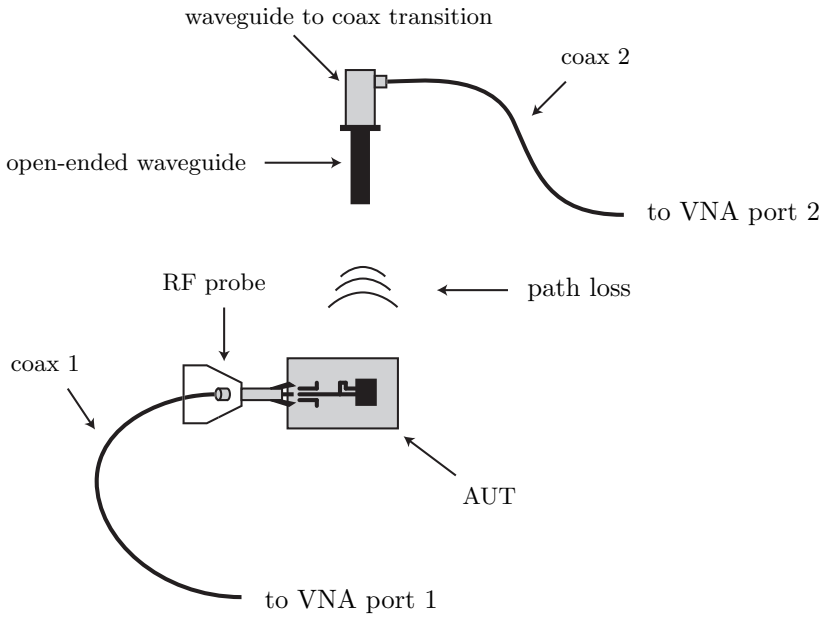
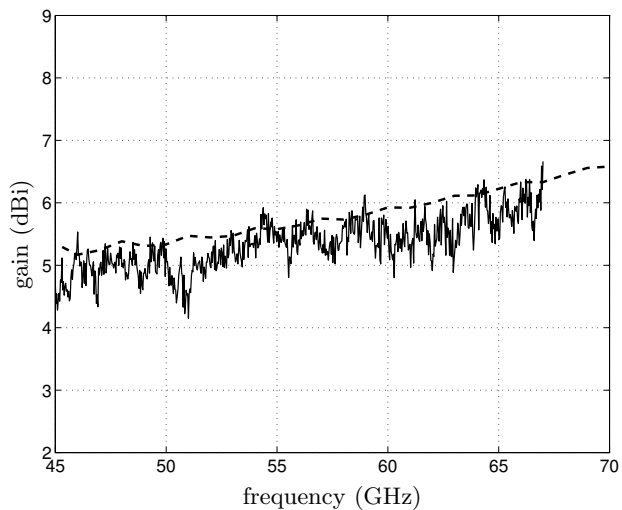Figure 4.12: Schematic layout of measurement setup.



Figure 4.13: Gain of open-ended waveguide as a function of frequency. Simulation (dashed), measurement (solid).

waveguide, the RF probe and the AUT are replaced with a waveguide-to-coax transition and an open-ended waveguide that is identical to the receive antenna. Since the gain of both these antennas are identical, (4.2) is written as

$$\frac{P_r}{P_t} = \frac{G_r^2 \lambda^2}{(4\pi |\mathbf{r}|)^2}. \tag{4.3}$$

In this way, only $G_r$ is unknown and therefore it can be obtained from measurements. The measured and simulated gain of the open-ended waveguide is shown in Fig. 4.13. Once the gain of the receive antenna and all the losses in the measurement system are known, the gain of the AUT can be determined as well.

### 4.3.3   Measurements BFACP antenna

The radiation pattern of the BFACP antenna has been measured in the frequency range from 50 to 60 GHz. A photograph of the AUT with RF probe is shown in Fig. 4.14. The antenna table has been covered with absorbing material and a polystyreen layer has been placed underneath the antenna. Polystyreen has a relative permittivity close to one and therefore it does not affect the performance of the antenna. Since the metal body of the RF probe can distort the radiation pattern, it has been covered with absorbing material as well.

The measurements have been conducted in a standard lab environment which implies that scattering of the radiated fields from the environment can occur. To analyse this effect, the measured signals have been transformed to the time-domain. In Figure 4.15 the time domain signal is shown as a function of elevation angle $\theta$. It is seen that the maximum of the power is received around $t = 2.5$ ns. Moreover, it is observed that there are some contributions which have a dependency on the elevation angle $\theta$. These contributions result from reflections of the environment. For example, the measured signals around $t = 14$ ns are caused by reflections from the ceiling of the laboratory. To reduce the effect of the environment, time-gating has been applied. The time-domain signals are filtered with a rectangular window from $t = 1.8$ ns to $t = 4.9$ ns and transformed to the frequency domain. The resulting radiation patterns in the E-plane and H-plane (see Fig. 4.14) are shown in Figures 4.16 and 4.17, respectively.

The measured radiation pattern is compared with two different simulations. The radiation pattern of the BFACP antenna is calculated with the Spark model of Section 2.8. In this model, the influence of the finite size of the dielectric layers is not accounted for. Another simulation is performed with CST Microwave Studio. In this simulation also the effect of the finiteness of the dielectric layers is included. The radiation from the edges of the dielectric causes dips in the radiation pattern around the elevation angles $\theta = -30, 0$ and 30 degrees. It is interesting to note that this effect can be accurately measured as well.

The difference in simulated and measured gain is approximately 2 dB. This loss is
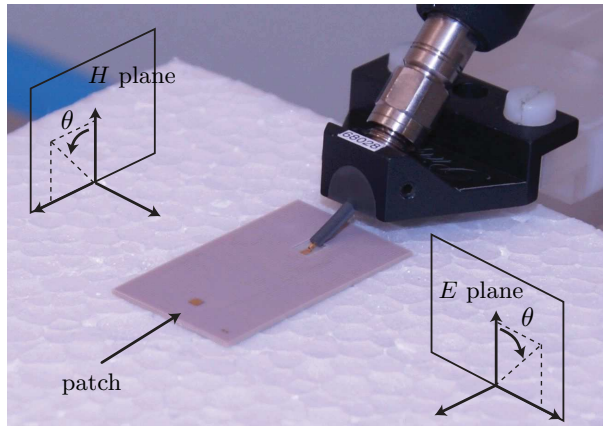
Figure 4.14: Photograph of antenna and RF probe. The E-plane, H-plane and elevation angle $\theta$ are indicated in the picture.
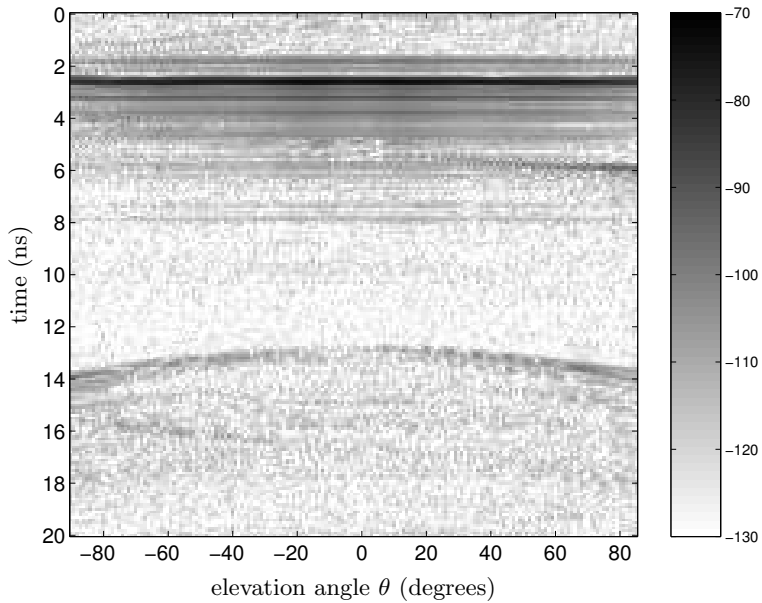


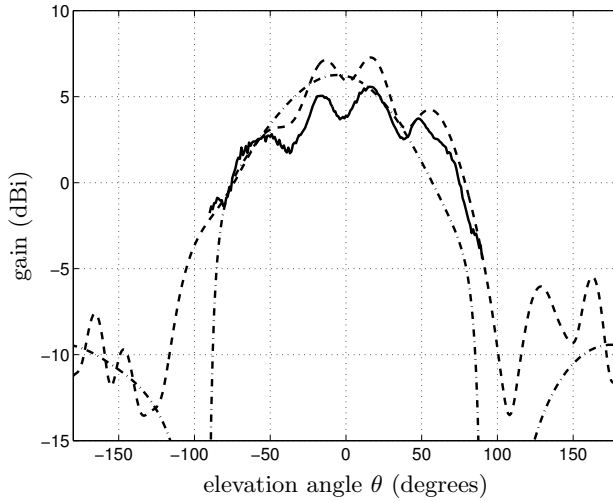Figure 4.15: Measured time-domain signals (dB) as a function of elevation angle.

Figure 4.16: Radiation pattern. E-plane, $f = 54.2$ GHz. Measurement (solid), CST Microwave Studio (dash), Spark (dash-dot).
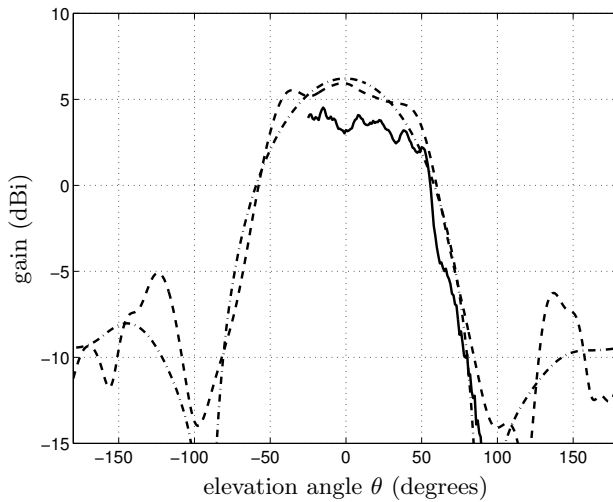


Figure 4.17: Radiation pattern. H-plane, $f = 54.2$ GHz. Measurement (solid), CST Microwave Studio (dash), Spark (dash-dot).

mainly caused by the feed line that connects the RF probe and the antenna. The total length from probe tip to antenna is 1.5 cm, which results in a feed-line loss of 2/1.5=1.3 dB/cm. Although this is a rough estimate since the feed line includes the CPW to MS transition and the balun, the value is comparable to simulated results that predicted a loss of about 1.2 dB/cm for a microstrip transmission line. In these simulations, a copper microstrip line with a metal thickness of 9 $\mu$m is considered. The back radiation is increased due to the presence of the feed network. Especially the balun introduces some additional back radiation. To verify this, the finite antenna with balanced feed is analysed in a 3D simulation. In this case, the back radiation remains well below $-10$ dBi.

### 4.3.4   Measurements dual-polarised BFACP antenna

To demonstrate the performance of the dual-polarised BFACP antenna (Section 3.8), two versions have been made. One with odd-mode excitation and one with even-mode excitation. Again, RF probes are used to connect to the antenna. Therefore, a transition from coplanar waveguide (CPW) to microstrip (MS) is designed and an open cavity is realized to be able to land the RF probe directly on the CPW feed. The feed network for the even-mode excitation is shown in Fig. 4.18.

A tee is used to split the MS line into the two branches of the balanced feed. The position of this tee is adjusted to select odd-mode or even-mode excitation. If the center of the tee is aligned with the center of the patch, the two outgoing microstrip lines of the tee are in phase and the antenna is excited similar to the even-mode excitation of Fig. 3.15. If the center of the tee is placed $\lambda_g/4$ out of the center-line, the effective phase difference between the two outgoing microstrip lines is 180 degrees, which is similar to the odd-mode excitation of Fig. 3.16. In this way, the even-mode and odd-mode excitations of the coplanar microstrip line are emulated.

The radiation pattern of the antenna is measured in the $\varphi = 0°$ plane (see Fig. 4.18). The co- and cross-polarization is simulated and measured for both antenna excitations (Figs. 4.19, 4.20). These simulations have been performed with CST Microwave Studio, and include the scattered radiation at the edges of the dielectric. It is observed that the antennas radiate a field with an orthogonal linear polarization. The measured gain is 1-2 dB lower than the simulated gain, which indicates that the dielectric and the feed network introduces some additional losses that are not accounted for in the simulation. In practice, the losses in the feed network can be reduced by designing a more compact feed network that is connected directly to a RF chip. The measured cross-polarization suppression level in the forward direction is 10-15 dB, which demonstrates that the antenna is able to select one specific linear polarization.
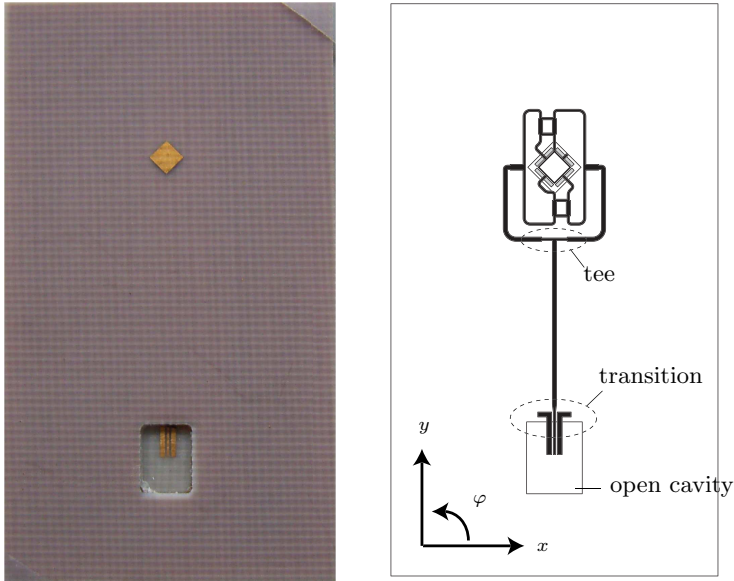
Figure 4.18: Dual-polarised antenna with even-mode excitation. Photograph (left), layout feed network (right).
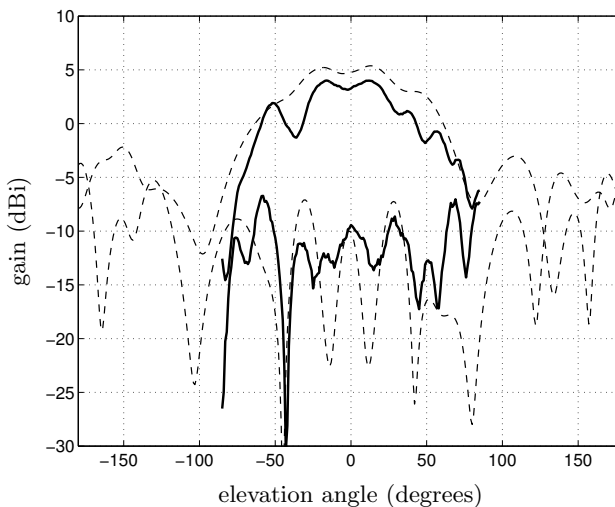


Figure 4.19: Co- and cross-polarised radiation pattern of dual-polarized antenna with even-mode excitation. Linear polarization, $\varphi = 45°$, frequency $f = 60$ GHz. Measurement (solid), simulation (dashed).
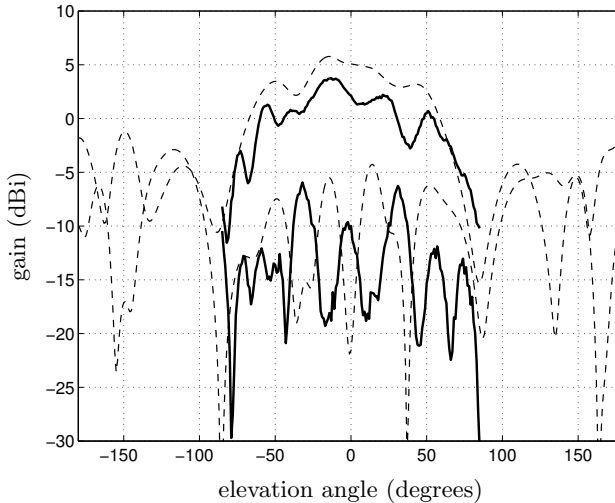
Figure 4.20: Co- and cross-polarised radiation pattern of dual-polarized antenna with odd-mode excitation. Linear polarization, $\varphi = 135°$, frequency $f = 60$ GHz. Measurement (solid), simulation (dashed).

## 4.4    Conclusions

In this chapter, measurement setups have been developed to characterise the performance of planar millimeter-wave antennas. These measurement setups have been used to validate the performance of the antenna designs that have been presented in Chapter 3.

It is important to create a well-defined interconnection between the measurement equipment and the AUT. Therefore, the use of RF probes has been employed to solve part of the interconnection problem. Additional CPW-MS transitions have been designed that realise the interconnection between the coplanar RF probe and the antenna under test. Moreover, a PCB balun design has been presented that enables the measurement of balanced antennas with single-ended measurement equipment. The radiation pattern of the AUT is measured with a far-field measurement setup that has been developed from scratch and that has been optimised for the measurement of millimeter-wave antennas and beam-forming antenna arrays. It has been shown that the measurement setups are capable of an accurate evaluation of the performance of the antennas under test.

The proposed measurement setups have been employed to validate the antenna designs that are presented in Chapter 3. It has been shown that these antenna concepts are valid since the predicted performances of the BFACP antennas are in good agreement with measured results. Therefore, the BFACP antenna design is optimised further

in Chapter 5 and beam-forming antenna arrays will be realised from the optimised BFACP antenna elements in Chapter 6.

# Sensitivity analysis and optimisation

## 5.1   Introduction

In previous chapters, the antenna element has been modelled, designed and measured. The antenna shows good performance regarding radiation efficiency and antenna bandwidth. However, before the antenna element is placed in an array configuration, it is important to investigate the effect of manufacturing tolerances on the performance. This is especially important since the antenna is realised in a standard, low-cost, planar manufacturing technology in which tolerances can be relatively large. Therefore, the sensitivity of the antenna structure for manufacturing tolerances is analysed in Section 5.2. To clarify the approach, an example is given in Section 5.3, where the sensitivity of the BFACP antenna for patch length is investigated.

Once the sensitivity of the structure is known, it is possible to use this information and improve the design. Gradient-based optimisation techniques use the sensitivity information to determine the direction in which an improved design can be obtained. These methods are discussed in Section 5.4. The sensitivity analysis and optimisation is combined in Section 5.5 for the analysis and optimisation of the BFACP antenna. It is shown that the presented methods result in an automated performance optimisation of the BFACP antenna that is computationally efficient as well.

## 5.2    Sensitivity analysis

The sensitivity analysis is used to investigate the influence of a small change in the design parameters of the EM structure on the performance of that structure. In this study, the design parameters can be either geometrical dimensions or material properties, whereas the performance of the structure is measured in terms of radiation efficiency, impedance bandwidth and/or radiation pattern.

### 5.2.1    Forward difference

A straightforward way of determining the sensitivity for a certain parameter vector $\mathtt{p}$ is to use a forward-difference method. In this method, the sensitivity of the objective function $\psi$ is approximated as (see e.g. [52, Chapt. 1])

$$\partial_{\mathtt{p}_i}\psi(\mathtt{p}) \approx \frac{\psi(\mathtt{p} + \tau\mathtt{u}_{\mathtt{p}_i}) - \psi(\mathtt{p})}{\tau}, \tag{5.1}$$

where $\mathtt{p}$ is the parameter vector, $\mathtt{u}_{\mathtt{p}_i}$ is a vector that is one in the $i^{\mathrm{th}}$ position and zero elsewhere, i.e., $|\mathtt{u}_{\mathtt{p}_i}| = 1$ and $\tau$ is a scalar that defines a small perturbation in $\mathtt{p}_i$. The advantage of this method is its simplicity. The disadvantage is that the method can become unstable for small values of $\tau$.

### 5.2.2    Direct differentiation

Alternatively, the direct differentiation method can be used [52]. Here, the function $\psi(\mathtt{p}, \bar{\mathtt{I}}(\mathtt{p}))$ is introduced as objective function. This function may have explicit dependence on the parameter vector $\mathtt{p}$, but it also depends on the solved current-coefficient vector $\bar{\mathtt{I}}$ that can be obtained from the MoM analysis of the EM problem. In a MoM formulation, the EM problem can be represented as [see e.g. Sections 2.5.2, 2.5.3, 3.3]

$$\mathtt{Z}(\mathtt{p})\mathtt{I} = \mathtt{V}(\mathtt{p}), \tag{5.2}$$

where $\mathtt{Z}$ is the interaction matrix that depends on the structure's geometry and material properties. In general, $\mathtt{Z}$ is dependent on the design parameters $\mathtt{p}$. The excitation vector $\mathtt{V}$ represents the sources in the EM problem. It may or may not depend on $\mathtt{p}$. From (5.2), the current-coefficient vector can be solved as

$$\bar{\mathtt{I}}(\mathtt{p}) = \mathtt{Z}^{-1}(\mathtt{p})\mathtt{V}(\mathtt{p}). \tag{5.3}$$

The sensitivity of the objective function with respect to the design parameters is written as

$$\partial_{\mathtt{p}_i}\psi(\mathtt{p}, \bar{\mathtt{I}}(\mathtt{p})) \quad \text{subject to} \quad \mathtt{Z}(\mathtt{p})\mathtt{I} = \mathtt{V}(\mathtt{p}). \tag{5.4}$$

This can be reformulated as

$$\partial_{\mathtt{p}_i}\psi(\mathbf{p}, \bar{\mathtt{I}}(\mathbf{p})) = \partial_{\mathtt{p}_i}^e \psi(\mathbf{p}, \bar{\mathtt{I}}(\mathbf{p})) + \left[\nabla_{\mathtt{I}}\psi(\mathbf{p}, \bar{\mathtt{I}}(\mathbf{p}))\right]^{\mathrm{T}} \cdot \partial_{\mathtt{p}_i}\bar{\mathtt{I}}(\mathbf{p}), \tag{5.5}$$

where the gradient vector $\nabla_{\mathtt{I}}$ is defined as

$$\nabla_{\mathtt{I}} = [\partial_{\mathtt{I}_1}\partial_{\mathtt{I}_2}\cdots\partial_{\mathtt{I}_N}]^{\mathrm{T}}. \tag{5.6}$$

The gradient $\partial_{\mathtt{p}_i}^e \psi$ acts on the first argument of $\psi(\mathbf{p}, \bar{\mathtt{I}}(\mathbf{p}))$ only. This term can be calculated analytically for well-defined objective functions. When the objective function does not depend explicitly on the parameter vector $\mathbf{p}$, this term will not even be present. It is recommended that $\psi$ is analytically differentiable with respect to $\bar{\mathtt{I}}$ as well, such that the term $\nabla_{\mathtt{I}}\psi$ can be evaluated.

The term $\partial_{\mathtt{p}_i}\bar{\mathtt{I}}$ can be obtained from

$$\begin{aligned}
\partial_{\mathtt{p}_i}\bar{\mathtt{I}} &= \partial_{\mathtt{p}_i}[\mathtt{Z}^{-1}\mathtt{V}] \\
&= [\partial_{\mathtt{p}_i}\mathtt{Z}^{-1}]\mathtt{V} + \mathtt{Z}^{-1}[\partial_{\mathtt{p}_i}\mathtt{V}] \\
&= -\mathtt{Z}^{-1}[\partial_{\mathtt{p}_i}\mathtt{Z}]\mathtt{Z}^{-1}\mathtt{V} + \mathtt{Z}^{-1}[\partial_{\mathtt{p}_i}\mathtt{V}] \\
&= \mathtt{Z}^{-1}\left(\partial_{\mathtt{p}_i}\mathtt{V} - [\partial_{\mathtt{p}_i}\mathtt{Z}]\bar{\mathtt{I}}\right),
\end{aligned} \tag{5.7}$$

where the relation $\partial_x[\mathtt{A}^{-1}] = -\mathtt{A}^{-1}[\partial_x\mathtt{A}]\mathtt{A}^{-1}$ has been employed. Note that in (5.7) the dependency of $\bar{\mathtt{I}}, \mathtt{Z}, \mathtt{V}$ on $\mathbf{p}$ has been suppressed.

To obtain the derivative $\partial_{\mathtt{p}_i}\bar{\mathtt{I}}$, the terms $\partial_{\mathtt{p}_i}\mathtt{V}$ and $\partial_{\mathtt{p}_i}\mathtt{Z}$ in (5.7) need to be determined. For example, in case of electric current-density expansion functions, the elements $\mathtt{V}_m$ and $\mathtt{Z}_{mn}$ have the form [see Section 2.5.2, Eq. (2.42)]

$$\begin{aligned}
\mathtt{V}_m(\mathbf{p}) &= -\Big\langle \mathbf{g}_m(\mathbf{p}, \mathbf{r}), \mathbf{E}^{\mathrm{inc}}(\mathbf{p}, \mathbf{r})\Big\rangle \\
&= -\int_S \mathbf{g}_m(\mathbf{p}, \mathbf{r}) \cdot \mathbf{E}^{\mathrm{inc}}(\mathbf{p}, \mathbf{r})\, dS, \\
\mathtt{Z}_{mn}(\mathbf{p}) &= \Big\langle \mathbf{g}_m(\mathbf{p}, \mathbf{r}), \mathbb{L}\{\mathbf{f}_n, \mathbf{0}\}(\mathbf{p}, \mathbf{r})\Big\rangle, \\
&= \int_S \mathbf{g}_m(\mathbf{p}, \mathbf{r}) \cdot \mathbb{L}\{\mathbf{f}_n, \mathbf{0}\}(\mathbf{p}, \mathbf{r})\, dS \\
&= -\int_S \mathbf{g}_m(\mathbf{p}, \mathbf{r}) \cdot \frac{j\omega}{k^2}\Big[k^2 + \nabla\nabla\cdot\Big]\int_{S'} \underline{\underline{\mathbf{G}}}^{AJ}(\mathbf{p}, \mathbf{r}, \mathbf{r}') \cdot \mathbf{f}_n(\mathbf{p}, \mathbf{r}')\, dS'\, dS
\end{aligned} \tag{5.8}$$

where $\mathbf{E}^{\mathrm{inc}}$ is the incident field that is imposed on the structure, $\mathbf{g}_m$ is a test function, $\mathbf{f}_n$ is an expansion function, $\mathbb{L}$ is an operator that relates the electric field at $\mathbf{r}$ to the source distribution that is defined by $\mathbf{f}_n$ and $\underline{\underline{\mathbf{G}}}^{AJ}$ is the dyadic Green's function for the magnetic vector potential.

Now, assume that the expansion and test functions are extended by zero on the domain $\mathbb{R}^2$. In this case, the integration limits are not a function of $\mathtt{p}_i$ and therefore, the partial derivative can be placed inside the integral. Resultantly, $\partial_{\mathtt{p}_i} \mathsf{V}_m$ and $\partial_{\mathtt{p}_i} \mathsf{Z}_{mn}$ can be determined as

$$
\begin{aligned}
\partial_{\mathtt{p}_i} \mathsf{V}_m(\mathtt{p}) = - \int\limits_{\mathbb{R}^2} & \partial_{\mathtt{p}_i} \tilde{\mathbf{g}}_m(\mathtt{p}, \mathbf{r}) \cdot \mathbf{E}^{\mathrm{inc}}(\mathtt{p}, \mathbf{r}) \\
& + \tilde{\mathbf{g}}_m(\mathtt{p}, \mathbf{r}) \cdot \partial_{\mathtt{p}_i} \mathbf{E}^{\mathrm{inc}}(\mathtt{p}, \mathbf{r}) \; dxdy, \\
\partial_{\mathtt{p}_i} \mathsf{Z}_{mn}(\mathtt{p}) = \int\limits_{\mathbb{R}^2} & \partial_{\mathtt{p}_i} \tilde{\mathbf{g}}_m(\mathtt{p}, \mathbf{r}) \cdot \mathbb{L}\{\tilde{\mathbf{f}}_n, \mathbf{0}\}(\mathtt{p}, \mathbf{r}) \\
& + \tilde{\mathbf{g}}_m(\mathtt{p}, \mathbf{r}) \cdot \partial_{\mathtt{p}_i} \mathbb{L}\{\tilde{\mathbf{f}}_n, \mathbf{0}\}(\mathtt{p}, \mathbf{r}) \; dxdy,
\end{aligned}
\tag{5.9}
$$

with,

$$
\begin{aligned}
\partial_{\mathtt{p}_i} \mathbb{L}\{\tilde{\mathbf{f}}_n, \mathbf{0}\}(\mathtt{p}, \mathbf{r}) = \frac{j\omega}{k^2} \Big[ k^2 + \nabla\nabla\cdot \Big] \Big[ & \int\limits_{\mathbb{R}^{2'}} \partial_{\mathtt{p}_i} \underline{\underline{\mathbf{G}}}^{AJ}(\mathtt{p}, \mathbf{r}, \mathbf{r}') \cdot \tilde{\mathbf{f}}_n(\mathtt{p}, \mathbf{r}') \\
& + \underline{\underline{\mathbf{G}}}^{AJ}(\mathtt{p}, \mathbf{r}, \mathbf{r}') \cdot \partial_{\mathtt{p}_i} \tilde{\mathbf{f}}_n(\mathtt{p}, \mathbf{r}') \; dx'dy' \Big].
\end{aligned}
\tag{5.10}
$$

where $\tilde{\mathbf{f}}_n$ is the function $\mathbf{f}_n$ extended to zero on the domain $\mathbb{R}^{2'}$ and $\tilde{\mathbf{g}}_m$ is the function $\mathbf{g}_m$ extended to zero on the domain $\mathbb{R}^2$.

The expressions in (5.9) can be written in the spectral domain representation following the approach described in Section 2.6.1 and can be evaluated numerically in that domain as well (see Section 2.6.2 and Section 5.3).

## 5.3 Example: Sensitivity of the input impedance of the BFACP antenna for patch length

The theory that was presented in previous section is now clarified with an example. For this example we consider the BFACP antenna that is presented in Chapter 3. We are interested in the sensitivity of the input impedance for a change in the length of the patch. In this case, the objective function is the input impedance that is defined as

$$
\psi(\mathtt{p}, \bar{\mathtt{I}}(\mathtt{p})) = \psi(\bar{\mathtt{I}}(p)) = -\frac{\mathsf{V}_k}{\mathtt{I}_k(p)},
\tag{5.11}
$$

where $p$ is a scalar that represents the length of the patch, $\mathsf{V}_k$ the (fixed) port voltage and $\mathtt{I}_k$ the port current of the antenna. The sensitivity of the objective function can be calculated according to (5.5). Since $\psi$ has no explicit dependence on $p$, it is found that $\partial_p^e \psi = 0$. The term $\nabla_{\mathtt{I}} \psi$ is defined as a column vector with elements

$$\partial_{I_n} \psi(\bar{\mathtt{I}}_k(p)) = \begin{cases} \frac{\mathtt{V}_k}{\mathtt{I}_k^2(p)} & n = k \\ 0 & n \neq k \end{cases}. \tag{5.12}$$

The term $\partial_p \bar{\mathtt{I}}$ is found from Eq. (5.7). Because the imposed field has no dependence on the parameter vector $\mathbf{p}$, the term $\partial_p \mathtt{V}$ vanishes, consequently,

$$\partial_p \bar{\mathtt{I}} = -\mathtt{Z}^{-1}[\partial_p \mathtt{Z}]\bar{\mathtt{I}}. \tag{5.13}$$

This leaves us with the problem of solving $\partial_p \mathtt{Z}$. Since the parameter does not affect the Green's function, the elements $\partial_p Z_{mn}$ can be calculated as [see (5.9), (5.10)]

$$\partial_p \mathtt{Z}_{mn}(p) = \int_{\mathbb{R}^2} \partial_p \tilde{\mathbf{g}}_m(p, \mathbf{r}) \cdot \mathbb{L}\{\tilde{\mathbf{f}}_n, \mathbf{0}\}(p, \mathbf{r}) \tag{5.14}$$
$$+ \tilde{\mathbf{g}}_m(p, \mathbf{r}) \cdot \mathbb{L}\{\partial_p \tilde{\mathbf{f}}_n, \mathbf{0}\}(p, \mathbf{r}) \, dx dy.$$

In the spectral-domain representation (see Section 2.6.1), (5.14) can be represented as

$$\partial_p \mathtt{Z}_{mn}(p) = -\frac{1}{4\pi^2} \int_{-\infty}^{\infty} \int_{-\infty}^{\infty} \hat{\mathbf{g}}'_m(p, -k_x, -k_y, z) \cdot \hat{\underline{\underline{\mathbb{L}}}}_0^J(k_x, k_y, z, z') \cdot \hat{\mathbf{f}}_n(p, k_x, k_y, z')$$
$$+ \hat{\mathbf{g}}_m(p, -k_x, -k_y, z) \cdot \hat{\underline{\underline{\mathbb{L}}}}_0^J(k_x, k_y, z, z') \cdot \hat{\mathbf{f}}'_n(p, k_x, k_y, z') \, dk_x dk_y. \tag{5.15}$$

where $\hat{\mathbf{f}}'(p, k_x, k_y, z)$ denotes the two-dimensional Fourier transform of $\partial_p \tilde{\mathbf{f}}(\mathbf{r})$.

Note that most terms $\mathtt{Z}_{mn}$ do not depend on the patch length. Only the terms that incorporate expansion and/or test functions on the patch do so. Therefore, the computational burden for the derivation of $\partial_p \mathtt{Z}$ is relatively low.

The input impedance and its sensitivity are shown in Figures 5.1 and 5.2, respectively. For comparison, the sensitivity of the input impedance is also calculated via a forward-difference approximation (Section 5.2.1).

## 5.4   Optimisation

The direct-differentiation method provides information about the derivative of the objective function with respect to a specified design parameter. This information can be used to analyse the effect of production tolerances on performance, but can also be used to optimise the design of the EM structure, for example, with a gradient-based optimisation technique. Gradient-based optimisation techniques have the advantage to be computationally efficient compared to stochastic optimisation techniques, especially in the case of large problems with many optimisation parameters. However,
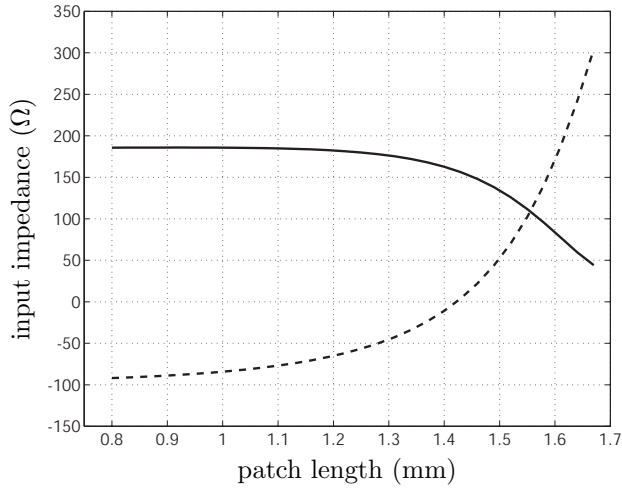
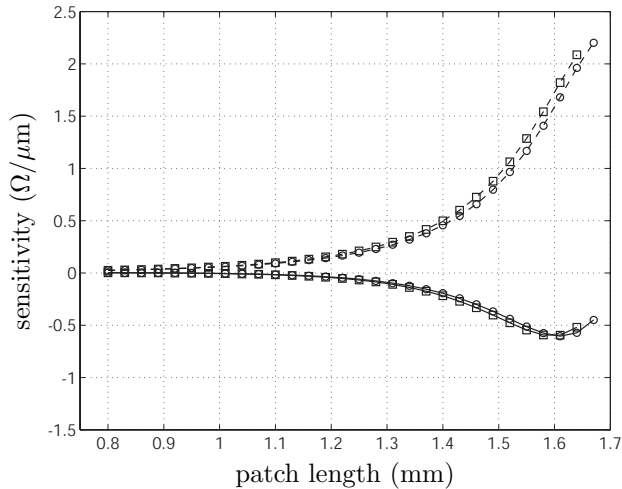Figure 5.1: Input impedance as a function of patch length.  Real part (solid), imaginary part (dashed).



Figure 5.2: Sensitivity of the input impedance as a function of patch length.  Real part (solid), imaginary part (dashed), direct differentiation method ($\circ$), forward difference approximation with step size $\tau = 0.03$ mm ($\square$).
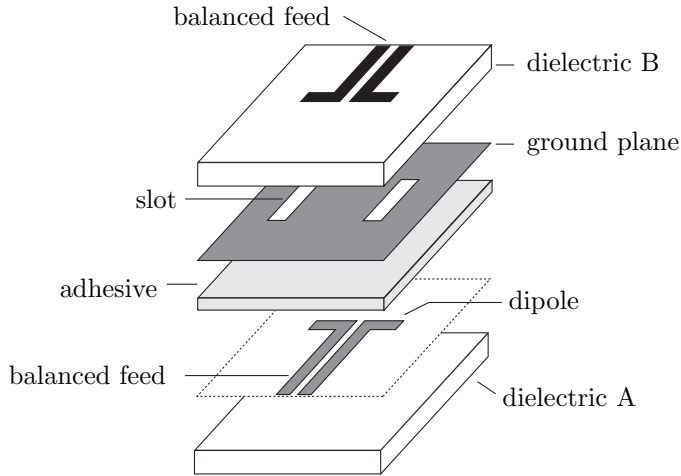
Figure 5.3: Geometry of the vertical layer transition.

with gradient-based optimisation one is only able to find a local optimum. Therefore, the objective function that has to be optimised should be chosen carefully, such that its derivatives can be calculated accurately and it should be verified that the optimisation routine does not converge to a local optimum that is not appropriate. In this respect, it is essential to have an adequate initial guess of the structure that has to be optimised.

### 5.4.1  Vertical layer transition

The optimisation algorithm is demonstrated with an example. In this example, a vertical layer transition is optimised. The layout of this transition is shown in Fig. 5.3. The transition is a two-port with two balanced feeds that are located on different layers and that are coupled via two slots in a ground plane. It can be used for signal transfer between adjacent layers without the use of vias. The vertical layer transition will be optimised for the transmission coefficient $\mathsf{S}_{12} = \mathsf{S}_{21}$ in the frequency band from 50 to 70 GHz. The transmission coefficient is defined as

$$\mathsf{S}_{12} = \frac{2\mathsf{Z}_{12}^{\mathrm{nw}}\sqrt{Z_{0,1}Z_{0,2}}}{(\mathsf{Z}_{11}^{\mathrm{nw}} + Z_{0,1})(\mathsf{Z}_{22}^{\mathrm{nw}} + Z_{0,2}) - \mathsf{Z}_{12}^{\mathrm{nw}}\mathsf{Z}_{21}^{\mathrm{nw}}}, \tag{5.16}$$

where $\mathsf{Z}_{uv}^{\mathrm{nw}}$, with $u \in \{1,2\}$, $v \in \{1,2\}$, represents an element of the $2 \times 2$ network impedance matrix (not to be mistaken with the interaction matrix $\mathsf{Z}$) and $Z_{0,u}$, with $u \in \{1,2\}$, represents the characteristic impedance of the $u^{\mathrm{th}}$ port. Note that in (5.16)

the dependency of $\mathtt{S}_{12}$ and $\mathtt{Z}^{\mathrm{nw}}_{uv}$ on $\omega$ and $\bar{\mathtt{I}}(\mathtt{p})$ has been suppressed. The accompanying objective function is given as

$$\psi(\bar{\mathtt{I}}(\mathtt{p})) = \frac{1}{\omega_1 - \omega_0} \int\limits_{\omega_0}^{\omega_1} |\mathtt{S}_{12}(\omega, \bar{\mathtt{I}}(\mathtt{p}))|^2 d\omega, \qquad (5.17)$$

where the design parameters are the length of the dipole in the lower layer, the length of the slots and the length of the dipole in the upper layer. In the optimisation routine, the integral over $\omega$ in Eq. (5.17) is approximated by a finite sum, i.e.,

$$\psi(\bar{\mathtt{I}}(\mathtt{p})) = \frac{1}{N} \sum_{n=0}^{N-1} |\mathtt{S}_{12}(\omega_0 + n\Delta_\omega, \bar{\mathtt{I}}(\mathtt{p}))|^2 d\omega. \qquad (5.18)$$

The vertical layer transition is modelled with equivalent magnetic currents that represent the slots, similar to the approach that has been used in Section 3.3. For simplicity, the balanced feeds are not modelled. Instead, the dipoles are excited with a delta-gap voltage source (Section 2.9.1), similar to the dipole in the example of Section 2.10. The currents on the dipoles are approximated with rooftop basis functions and the equivalent magnetic currents are modelled with entire-domain basis functions.

The network impedance matrix $\mathtt{Z}^{\mathrm{nw}}$ can be obtained from the interaction matrix $\mathtt{Z}$ [53]. First, the elements of the interaction matrix and the excitation vector are regrouped in sub-matrices, i.e.,

$$\begin{bmatrix} \mathtt{Z}^{tt} & \mathtt{Z}^{tc} \\ \mathtt{Z}^{ct} & \mathtt{Z}^{cc} \end{bmatrix} \begin{bmatrix} \mathtt{I}^t \\ \mathtt{I}^c \end{bmatrix} = \begin{bmatrix} \mathtt{V}^t \\ 0 \end{bmatrix}. \qquad (5.19)$$

Here, $\mathtt{V}^t$ is chosen such that it only contains the two nonzero elements that are associated with the rooftop basis functions that are located at the two ports (terminals). The elements of the interaction matrix are grouped accordingly. Second, the network impedance matrix is obtained as [53]

$$\mathtt{Z}^{\mathrm{nw}} = \mathtt{Z}^{tt} - \mathtt{Z}^{tc}\mathtt{Z}^{cc-1}\mathtt{Z}^{ct}. \qquad (5.20)$$

A gradient-based optimisation method is employed to optimise the transmission coefficient. In this example a modified Gauss-Newton algorithm is used (function E04DGF of the NAG library [25]), that is suitable for finding an unconstrained minimum of a sum of squares. The objective function uses N = 3 frequency points at $f$ = 50, 60 and 70 GHz. The value of the objective function is shown in Fig. 5.4 as a function of the number of iterations of the optimisation routine. It is observed that the optimisation routine converges within 10 iterations. The performance of the initial design and the optimised design is shown in Fig. 5.5. An initial guess was chosen that has a poor performance to show the robustness of the optimisation process. Moreover,
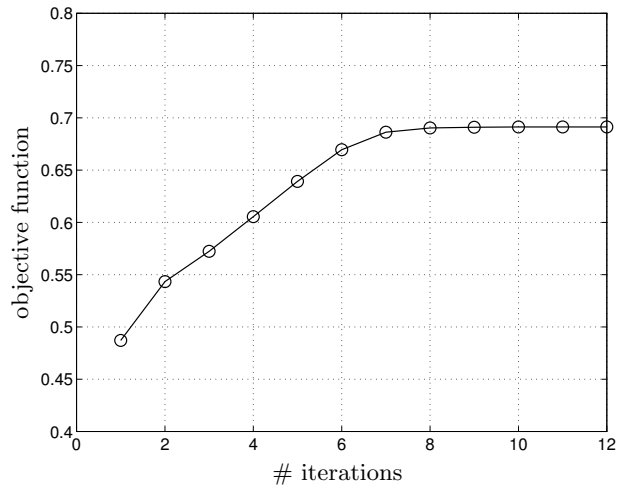
Figure 5.4: Convergence of the optimisation process of the vertical layer transition.
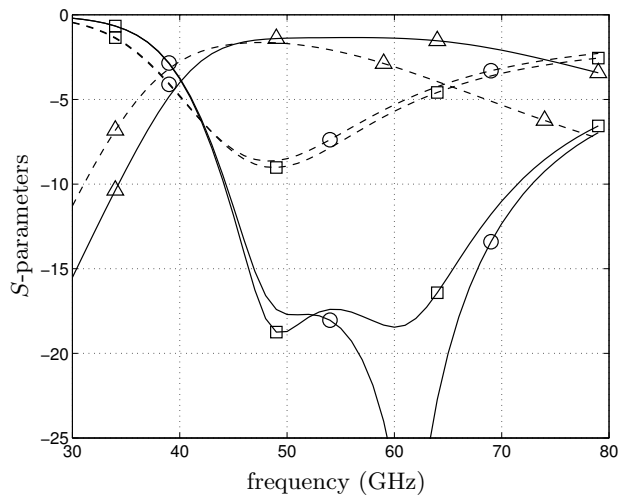


Figure 5.5: $S$-parameters vertical layer transition. Initial guess (dashed), optimised (solid). $S_{11}(\circ)$, $S_{12}(\triangle)$, $S_{22}(\square)$

several initial guesses have been tried to verify that the optimisation routine finds a single optimum. The optimised design shows a transmission loss of less than 2 dB in the frequency range from 44 to 69 GHz. As a consequence, the reflection coefficients $(\mathtt{S}_{11}, \mathtt{S}_{22})$ also improve significantly.

## 5.5   Optimisation and sensitivity analysis of the BFACP antenna

In the preceding sections, it has been shown that it is possible to determine the sensitivity of an EM structure and it has been shown that this information can be used for the optimisation of the response of the structure. In this section, this idea is used to analyse and optimise the BFACP antenna. In general, it is possible to find a good initial estimate for the dimensions of the antenna. For example, the patch length of a patch antenna can be estimated as $l_{\mathrm{patch}} = \frac{\lambda_d}{2}$, with $\lambda_d$ the wavelength in the dielectric. When it is possible to find an initial guess that lies close to an optimal one, a local optimization strategy can be used to optimise the antenna structure. Therefore, it is tried to give some simple design rules for the initial design and use this design in the optimisation routine.

In our case, the radiation efficiency and the reflection coefficient of the antenna need to be optimised simultaneously over a certain bandwidth $\omega_0 < \omega < \omega_1$. The proposed objective function is given as

$$\psi(\bar{\mathtt{I}}(\mathbf{p})) = \frac{1}{\omega_1 - \omega_0} \int\limits_{\omega_0}^{\omega_1} (1 - |\Gamma(\omega, \bar{\mathtt{I}}(\mathbf{p}))|^2)\eta(\omega, \bar{\mathtt{I}}(\mathbf{p}))d\omega. \tag{5.21}$$

The reflection coefficient $\Gamma$ is obtained from

$$\Gamma(\omega, \bar{\mathtt{I}}(\mathbf{p})) = \frac{Z_{\mathrm{in}}(\omega, \bar{\mathtt{I}}(\mathbf{p})) - Z_0}{Z_{\mathrm{in}}(\omega, \bar{\mathtt{I}}(\mathbf{p})) + Z_0}, \tag{5.22}$$

where $Z_0$ is the characteristic port impedance of the balanced feed. The radiation efficiency $\eta$ is found from Eq. (3.16). The sensitivity of the integrand of the objective function is written as

$$\begin{aligned}\nabla_{\mathbf{p}}&\big[(1 - |\Gamma(\omega, \bar{\mathtt{I}}(\mathbf{p}))|^2)\eta(\omega, \bar{\mathtt{I}}(\mathbf{p}))\big] \\ &= -2\mathrm{Re}\{\Gamma^*(\omega, \bar{\mathtt{I}}(\mathbf{p}))\nabla_{\mathbf{p}}\Gamma(\omega, \bar{\mathtt{I}}(\mathbf{p}))\}\eta(\omega, \bar{\mathtt{I}}(\mathbf{p})) \\ &\quad + (1 - |\Gamma(\omega, \bar{\mathtt{I}}(\mathbf{p}))|^2)\nabla_{\mathbf{p}}\eta(\omega, \bar{\mathtt{I}}(\mathbf{p})). \end{aligned} \tag{5.23}$$

It can be shown (see Appendix B) that $\nabla_{\mathbf{p}}\Gamma$ and $\nabla_{\mathbf{p}}\eta$ can be expressed in terms of $\nabla_{\mathbf{p}}\mathtt{V}$ and $\nabla_{\mathbf{p}}\mathtt{Z}$, which allows us to obtain the sensitivity of the objective function.

Once this sensitivity has been determined, an optimization routine can be used to optimise the objective function. The PCB stack that is used for the realisation of

| Element | Parameter | Initial value (mm) | Optimised value (mm) |
|---|---|---|---|
| patch | length | 1.59 | 1.38 |
| | width | 1.35 | - |
| slots | length | 1.57 | 1.49 |
| | width | 0.20 | - |
| | spacing | 1.74 | 1.76 |
| reflector | length | 2.30 | - |
| | width | 1.80 | - |
| dipole | length | 1.95 | 2.11 |
| | width | 0.25 | - |

Table 5.1: Dimensions of the optimised antenna.

the antenna is fixed since only a discrete set of materials and layer thicknesses are available. Therefore, only the geometrical parameters of the antenna are optimised. More specifically, the length of the patch, the length of the slots, the spacing of the slots, and the length of the dipole can be adjusted such that the reflection coefficient as well as the radiation efficiency is optimised in the frequency band from 57 to 64 GHz. Small variations in the dimensions of the reflector element affect the antenna behaviour very little because the reflector shows good performance over a wide frequency band. Therefore, the dimensions of the reflector have not been optimised.

As an initial estimate, the patch length has been chosen as $l_{\text{patch}} = \lambda_d^{\text{high}}/2$, with $\lambda_d^{\text{high}}$ the wavelength in the dielectric at the highest operating frequency (64 GHz). The initial slot length is $l_{\text{slot}} = \lambda_d^{\text{low}}/2$, with $\lambda_d^{\text{low}}$ the wavelength at the lowest operating frequency (57 GHz). This ensures that the patch and the slots resonate at slightly different frequencies such that the antenna bandwidth is improved. The initial slot spacing is chosen as $l_{\text{spacing}} = 0.35\,\lambda_0$, which is a compromise between radiation efficiency and coupling between the slots and the patch (see Section 3.4). The length of the dipole underneath the slots is chosen as $l_{\text{dip}} = l_{\text{spacing}} + w_{\text{slot}}$, with $w_{\text{slot}}$ the width of the slot. This ensures that the dipole has sufficient length to couple to the slots.

In the optimisation routine, the integral over $\omega$ in Eq. (5.21) is approximated by a finite sum. The objective function has been optimised through a conjugate gradient optimization algorithm (E04DGF [25]). The initial and optimised dimensions are shown in Table 5.1 and the convergence of the optimisation process is shown in Fig. 5.6. The reflection coefficient and radiation efficiency of the resulting antenna design are shown in Fig. 5.7. The accompanying sensitivity of the reflection coefficient for the optimisation parameters is shown in Fig. 5.8 as a function of frequency. It is observed that this algorithm is able to find an optimum within a few iterations. Moreover, it is shown that this antenna geometry is able to achieve a -10dB bandwidth of 15% with a radiation efficiency that is larger than 79% throughout the band of operation.
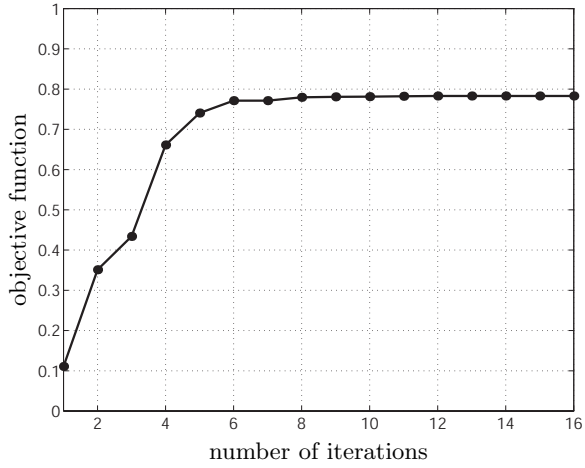
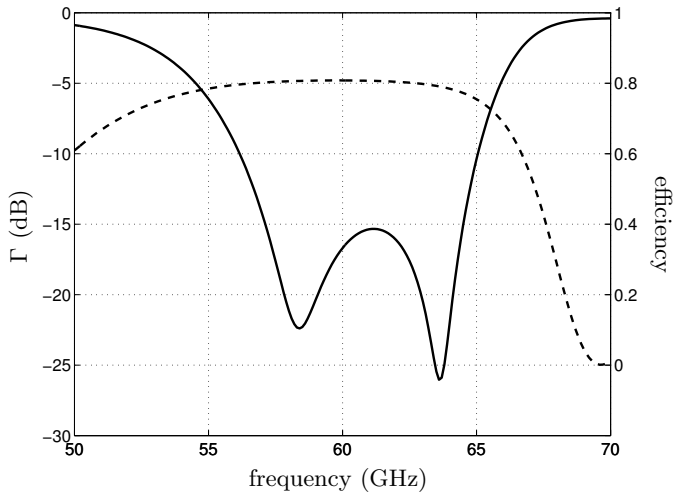Figure 5.6: Convergence of the objective function.



Figure 5.7: Reflection coefficient (solid) and radiation efficiency (dashed) of the optimised antenna. Dimensions in Table 5.1.
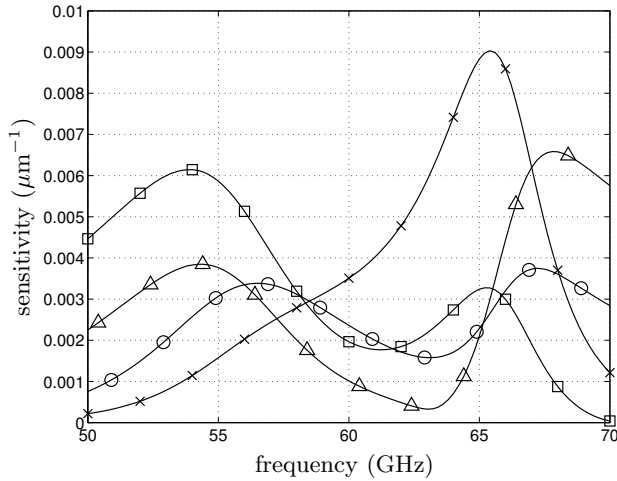
Figure 5.8: Absolute value of the sensitivity of the reflection coefficient $|\partial_{p_i}\Gamma|$ for the following optimisation parameters: dipole length ($\square$), slot length ($\triangle$), slot spacing ($\circ$), patch length ($\times$).
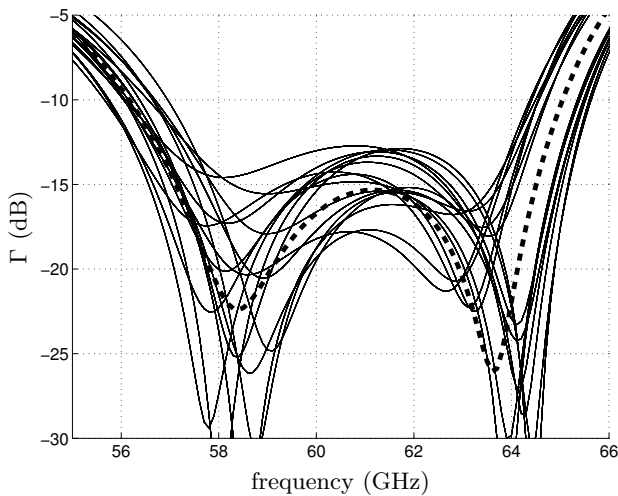


Figure 5.9: Tolerance analysis of the reflection coefficient. The patch length, dipole length, slot length and slot spacing are perturbed with $\delta_{\max} = \pm 15\mu$m. Nominal design (dashed), perturbed designs (solid).

A sensitivity analysis allows for a first-order analysis of the influence of production tolerances on the performance of the antenna. For example, the influence of tolerances on the reflection coefficient can be determined as

$$\Gamma(\omega, \mathbf{p} + \boldsymbol{\Delta}) \approx \Gamma(\omega, \mathbf{p}) + \nabla_{\mathbf{p}}\Gamma(\omega, \mathbf{p}) \cdot \boldsymbol{\Delta}, \tag{5.24}$$

where $\boldsymbol{\Delta}$ is a vector that determines the variation of each parameter. Structures in a manufacturing process can be realised with a certain metallisation tolerance $\delta_{\max}$. In PCB technology the metallisation tolerance is about $\delta_{\max} = 15\mu m$ both ways. The influence of such variations on the reflection coefficient of the optimised antenna is shown in Fig. 5.9, where all four parameters used in the optimisation have been perturbed by $\pm\delta_{\max}$. It is observed that the reflection coefficient remains well below $-10$ dB throughout the band of operation (57-64 GHz). The influence of parameter variations on the radiation efficiency is minimal, i.e., the radiation efficiency varies less than 2% within the band of operation.

Other types of tolerance, like registration tolerance and tolerance on the layer thickness can be determined as well. The sensitivity of antenna performance on these types of tolerances can be analysed with the presented method as well. However, it is noted that the metallisation tolerance is the dominant effect on antenna performance, for our case.


## 5.6   Conclusions


In this chapter, the sensitivity analysis and optimisation of planar EM structures have been investigated. First, the sensitivity has been determined through a direct differentiation method. This method has been applied to the EM modelling that has been derived in Chapter 2 and has been validated through comparison with an approximate forward-difference method. Hereafter, the sensitivity information has been used for the optimisation of planar EM structures. For this purpose, an objective function has been introduced that has been optimised following a gradient-based optimisation strategy. Finally, the sensitivity analysis and optimisation have been applied to the BFACP antenna. It has been shown that the antenna can be optimised within few iterations with the presented method. The optimisation method will be used for the design of the antennas in the antenna arrays that are presented in the next chapter.

# Array design

## 6.1 Introduction

In preceding chapters, the design, measurement and optimisation of the antenna element has been treated. In this chapter, the design is extended towards an array configuration of these elements to enable beam forming. Antenna arrays have been discussed extensively in literature [13], [54]. In earlier work, the rigorous analysis of large arrays has received much attention. It has been shown that the behaviour of these arrays can be approximated by the behaviour of infinite arrays, which simplifies the analysis [55], [56]. During this research, important concepts have been introduced, such as mutual coupling and scan blindness. Later on, as more computational resources became available, also finite-sized antenna arrays have been investigated through full-wave method-of-moments simulations [57]. This is the approach we will follow as well. The MoM formulation for the analysis of an antenna element is extended to the analysis of an antenna array in Section 6.2.

Hereafter, the performance of the BFACP antenna in array configurations is investigated in terms of gain, radiation efficiency, and bandwidth. It turns out that the performance of the antenna array is dependent on the scan angle of the antenna array. This effect is analysed and a circular array configuration is proposed (Section 6.3). The beam-forming performance of the circular array is demonstrated and validated through measurements in Section 6.4.

## 6.2   Antenna array modelling

### 6.2.1   MoM matrix equation

The modelling of an antenna array is very similar to the modelling of an antenna element. Basis functions are employed on all antenna elements to approximate the equivalent current-density on the structure. The interaction matrix $\mathtt{Z}$ is extended such that it contains the interaction of basis functions that are located on different antenna elements as well. Since each antenna of the array is excited separately, the excitation vector $\mathtt{V}$ accounts for the effect of multiple sources with accompanying phase and amplitude distribution. For example, in case of a 2-element array with antennas $a$ and $b$, the MoM matrix equation can be represented as

$$\left[ \begin{array}{cc} \mathtt{Z}^{aa} & \mathtt{Z}^{ab} \\ \mathtt{Z}^{ba} & \mathtt{Z}^{bb} \end{array} \right] \left[ \begin{array}{c} \mathtt{I}^{a} \\ \mathtt{I}^{b} \end{array} \right] = \left[ \begin{array}{c} \mathtt{V}^{a} \\ \mathtt{V}^{b} \end{array} \right], \tag{6.1}$$

where $\mathtt{Z}^{aa}$ is the interaction matrix of antenna $a$, $\mathtt{Z}^{bb}$ is the interaction matrix of antenna $b$, and $\mathtt{Z}^{ab}$, $\mathtt{Z}^{ba}$ are the interaction matrices that represents the mutual coupling between antennas $a$ and $b$. The excitation vector contains both excitation vectors of antenna $a$ and $b$.

### 6.2.2   Network impedance matrix

The antenna array can be treated as a multiport network that has an accompanying network impedance matrix. This network impedance matrix can be derived from the MoM matrix equation [53]. Let us assume that only delta-gap voltage sources are present for the excitation of the antenna array elements. In this case, the excitation vector simplifies to a column vector with only non-zero entries that are associated with test functions that are located at the antenna ports. The MoM matrix equation (6.1) can therefore be reorganised in the following form [53]:

$$\left[ \begin{array}{cc} \mathtt{Z}^{tt} & \mathtt{Z}^{tc} \\ \mathtt{Z}^{ct} & \mathtt{Z}^{cc} \end{array} \right] \left[ \begin{array}{c} \mathtt{I}^{t} \\ \mathtt{I}^{c} \end{array} \right] = \left[ \begin{array}{c} \mathtt{V}^{t} \\ \mathtt{0} \end{array} \right], \tag{6.2}$$

where the superscripts $t, c$ denote the distinction between elements that are related to the port (terminal) and to the rest of the circuit, respectively. The network impedance matrix can be obtained from (6.2) as

$$\mathtt{Z}^{\mathrm{nw}} = \mathtt{Z}^{tt} - \mathtt{Z}^{tc}\mathtt{Z}^{cc-1}\mathtt{Z}^{ct}. \tag{6.3}$$
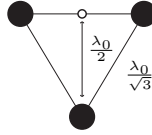
Figure 6.1: Inter-element distance of a hexagonal grid.

### 6.2.3 Active input impedance

The active input impedance is defined as the impedance at one port while all ports are active. The active input impedance is of importance since it describes the impedance of the array under working conditions, i.e., while all antennas are excited with a certain amplitude and phase distribution. The active input impedance can be determined from the network impedance matrix, viz,

$$Z_{\text{in},n}^a = \frac{\mathtt{V}_n^t}{\mathtt{I}_n^t}, \tag{6.4}$$

with

$$\mathtt{I}^t = [\mathtt{Z}^{\text{nw}} + \mathtt{Z}_0]^{-1}\mathtt{V}^t. \tag{6.5}$$

Here $\mathtt{Z}_0$ is a diagonal matrix with entries $Z_{0,n}$ on the diagonal that represent the source impedance of the $n^{\text{th}}$ port.

## 6.3 BFACP antenna array

### 6.3.1 Hexagonal 7-element array

For the planar array there are two main configurations, which are related to the positions of the antenna elements. The antenna elements can be positioned in a square grid or in a hexagonal grid. For the square grid, the distance between the antenna elements should be less than half a free-space wavelength ($\lambda_0$) to avoid grating lobes. For the hexagonal grid, this is slightly different, since the distance between the phase centers of the joint elements should be less than $\lambda_0/2$. As a result the elements in the hexagonal grid can be placed at a distance which is less than $\lambda_0/\sqrt{3}$ (Fig. 6.1).

The beam of the antenna array can be tilted by exciting each antenna element with the appropriate phase. The phase $\xi_n$ of each source can be determined as

$$\xi_n = -k_0 \mathbf{r}_{\text{scan}} \cdot \mathbf{r}_n, \tag{6.6}$$

where $\mathbf{r}_n$ denotes the position of the $n^{\text{th}}$ antenna and $\mathbf{r}_{\text{scan}}$ is a vector that points
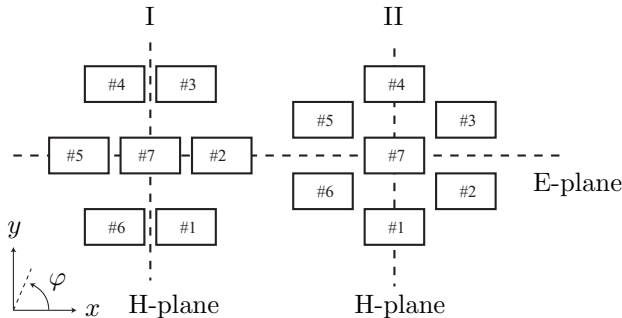
Figure 6.2: Two layouts for the 7-element hexagonal array.

towards the desired scan angle, i.e.,

$$\mathbf{r}_{\text{scan}} = \sin(\theta_0)\cos(\varphi_0)\mathbf{u}_x + \sin(\theta_0)\sin(\varphi_0)\mathbf{u}_y + \cos(\theta_0)\mathbf{u}_z, \qquad (6.7)$$

with $\theta_0, \varphi_0$ the desired scan angle in elevation and azimuth, respectively.

The effect of mutual coupling on the performance of the antenna array can be quite significant. In general, the mutual coupling between elements decreases when the distance between the elements is increased. From this point of view, the hexagonal grid is a better choice. Another advantage of the hexagonal grid is that, compared to the square grid, the directivity of the array is larger for the same number of elements. This is because the effective aperture of the hexagonal array is larger than the effective aperture of the square array since the distance between the elements is larger for the hexagonal grid. Note that this improvement in gain does not come for free; the side lobe level of the array on the hexagonal grid is higher than the side lobe level of the array on the square grid for the same number of elements.

The performance of the 7-element hexagonal array is investigated. Seven elements should be sufficient to acquire a broadside antenna gain that is larger than 10 dBi. Two possible layouts are shown in Fig. 6.2, where a rectangle is used to depict the approximate size of the antenna element. The radiation pattern of the antenna element is almost independent of azimuth angle $\varphi$. If mutual coupling between the elements is neglected, the performance of both layouts is equal. Still, both layouts show quite a different performance when the effect of mutual coupling is taken into account in a full-wave simulation.

The performance of the antenna array is modelled with a method-of-moments implementation which is based on the antenna model that is presented in Chapter 3. An extension of this model is implemented such that finite antenna arrays consisting of balanced-fed aperture-coupled patch antenna elements can be analysed (see Section 6.2). Antenna elements are used that have been optimised for the frequency band from 59 to 64 GHz following the approach presented in Section 5.5. The dimensions

| Element | Parameter | Value |
|---|---|---|
| patch | length | 1.37 mm |
| | width | 1.35 mm |
| slots | length | 1.43 mm |
| | width | 0.20 mm |
| | spacing | 1.77 mm |
| reflector | length | 2.30 mm |
| | width | 1.80 mm |
| dipole | length | 2.15 mm |
| | width | 0.25 mm |
| feed | width | 0.20 mm |
| | spacing | 0.15 mm |

Table 6.1: Dimensions of the optimised antenna for the frequency band 59-64 GHz.

of the optimised antenna elements are shown in Table 6.1. Each antenna element is fed with a delta-gap voltage source (Section 2.9.1) that is placed at the center of the dipole feed of the antenna.

Figure 6.3 shows the directivity, radiation efficiency and active reflection coefficients as a function of elevation scan angle $\theta$ of array I in Fig. 6.2 for $\varphi = 0°$ (E-plane) and $\varphi = 90°$ (H-plane), respectively. The radiation efficiency $\eta$ is defined as the ratio between radiated power in the whole upper hemisphere and accepted power at the antenna feeds [see also (3.16)]. The radiation efficiency of the single-element antenna is about 80% (see Fig 5.7). Most of the remaining 20% of power is excited into surface waves. In an array configuration, neighbouring elements excite surface waves that interfere and reduce or increase the total amount of surface-wave power depending on the phase distribution of the antenna elements. Therefore the radiation efficiency is a function of scan angle.

The active reflection coefficient is an important parameter to analyse the behaviour of each antenna element under actual operation conditions, where each element is excited. The active reflection coefficient is calculated as

$$\Gamma_n = 10 \log_{10} \left| \frac{Z_{\text{in},n}^a - Z_0}{Z_{\text{in},n}^a + Z_0} \right|^2, \tag{6.8}$$

where $Z_{\text{in},n}^a$ is the active input impedance of the $n^{\text{th}}$ element and $Z_0 = 100\Omega$ is the characteristic impedance of the feed.

It has been observed that the directivity as a function of scan angle is comparable in both planes. However, the difference in radiation efficiency is remarkable. This can be explained by examining the effect of the interacting surface waves in the array configuration. The surface waves are excited mostly in the $\varphi = 0°$ direction. Therefore, elements in this direction couple stronger than elements in the $\varphi = 90°$
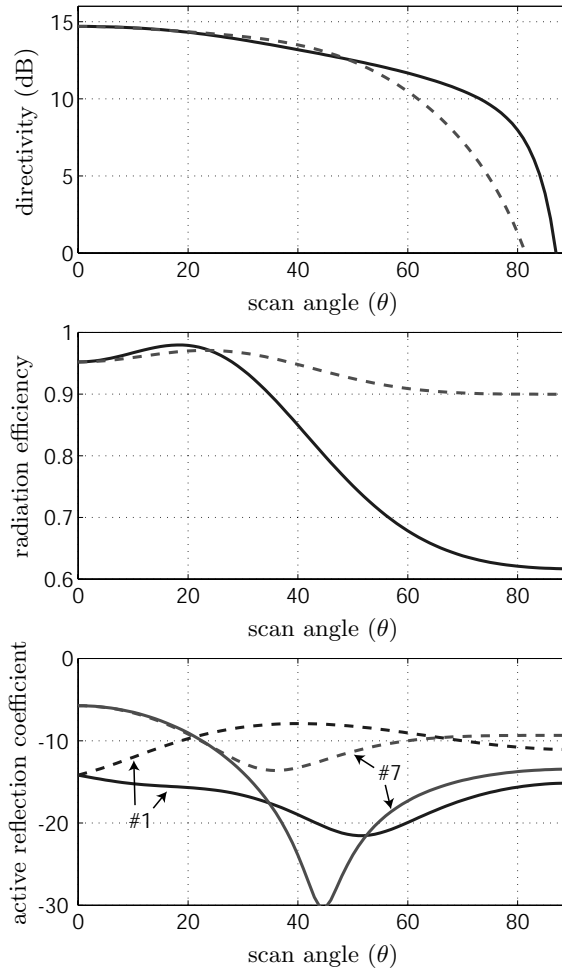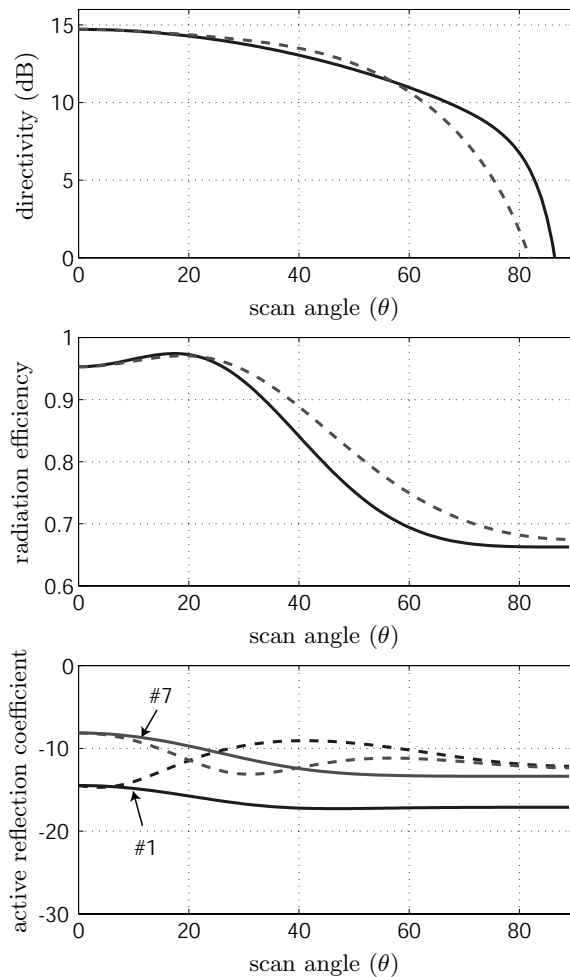
Figure 6.3: Hexagonal 7-element array, layout I. Directivity, radiation efficiency and active reflection coefficient for a scan in the $\varphi = 0°$ (solid lines) and $\varphi = 90°$ (dashed lines) plane. The active reflection coefficient is shown for a typical element and for the element with the worst performance.

Figure 6.4: Hexagonal 7-element array, layout II. Directivity, radiation efficiency and active reflection coefficient for a scan in the $\varphi = 0°$ (solid lines) and $\varphi = 90°$ (dashed lines) plane. The active reflection coefficient is shown for a typical element and for the element with the worst performance.

direction. At broadside radiation, the elements are excited in phase and the inter-element distance is such that the surface waves are suppressed significantly. This results in a high radiation efficiency. When the beam is scanned in the $\varphi = 0°$ plane, the phases of the elements in this direction are adjusted accordingly. Since this affects the suppression of the surface waves, this introduces a significant impact on the radiation efficiency as well as on the active input impedance. A scan in the $\varphi = 90°$ plane will not affect the surface-wave suppression much, and therefore the radiation efficiency remains high for the entire scan range.

The active reflection coefficient should remain low for the entire scan range. In Fig. 6.3 it is observed that especially the centre element can have a high active reflection co-efficient for some scan angles. This is undesirable, since it introduces additional reflection losses in the transceiver system. The performance of layout I can be im-proved by changing to layout II. In this layout the inter-element distance is as large as possible in the $\varphi = 0°$ plane. Therefore the elements couple less and the performance of the array is more symmetric in both planes (Fig. 6.4). Also the active reflection coefficient shows some better performance because of the reduced coupling between the elements.

## 6.3.2   Circular 6-element array

To further reduce the mutual coupling within the array, the middle element in layout II of the hexagonal 7-element array is removed. The resulting layout is a circular 6-element array. The performance of the circular array is shown in Fig. 6.5 and it is observed that its performance is superior to the performance of the hexagonal array although only 6 elements are used. The reason for this is that the aperture area of the antenna array remains the same while the mutual coupling within the array is reduced. Because the array has no center element, the aperture area is not illuminated homogenously. Therefore a slight decrease in directivity is observed for larger scan angles compared to the 7-element array. However, the advantage of this layout is that the active reflection coefficient remains below -10 dB throughout the whole scan range for each antenna element.

Another advantage of the circular configuration is that it simplifies the realisation of the feed network since it is complicated to feed the center antenna element of the hexagonal 7-element array. In the circular configuration, all elements can be connected directly from outside the array and no feed lines are needed that run between other antenna elements.
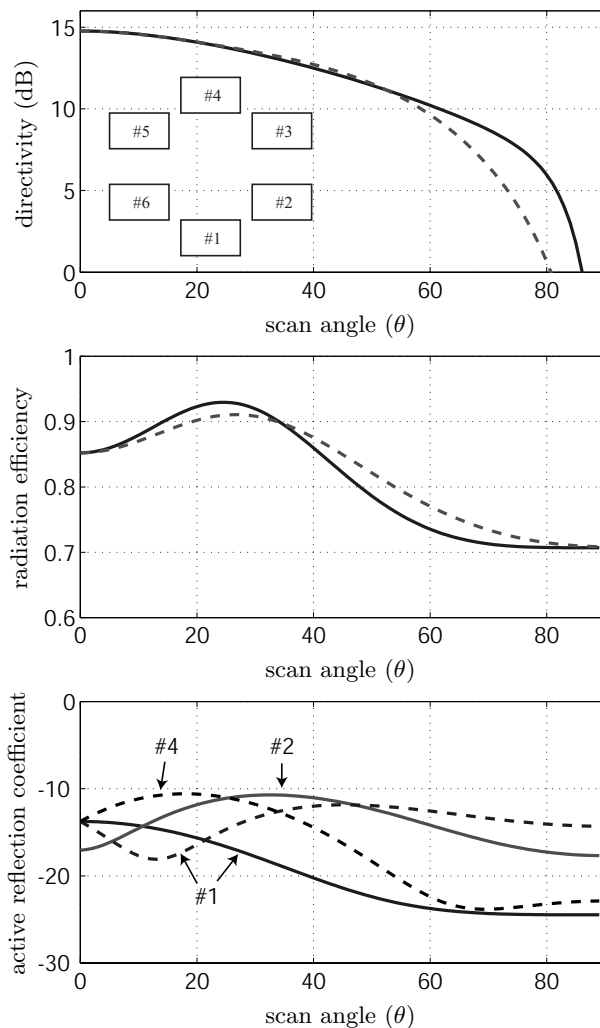
Figure 6.5: Circular 6-element array. Directivity, radiation efficiency and active reflection coefficient for a scan in the $\varphi = 0°$ (solid lines) and $\varphi = 90°$ (dashed lines) plane. The active reflection coefficient is shown for a typical element and for the element with the worst performance.

## 6.4    Demonstration of beam-forming

In a millimeter-wave transceiver, an antenna array consisting of BFACP antenna elements will be connected to a transceiver chip, which has balanced interconnections to each antenna element. As long as the active electronics are located close to the antenna, the feed-line loss is limited and the antenna efficiency will be close to the estimated efficiency of 80%. To validate the performance of the antenna element in an array configuration, a 6-element circular array with a fixed feed network has been designed (Fig. 6.6). The feed network for this array consists of microstrip transmission lines and baluns are used to implement the conversion from microstrip to coplanar microstrip at each antenna element. This approach is similar to the measurement setup that has been used for the single element antenna. For the power division, Bagley power dividers [58] and reactive T-junctions are used. The capabilities of beam-forming with the circular array is demonstrated by using separate feed networks that provide each antenna element with the correct phase for a specific fixed scan angle. The circular antenna array and accompanying feed network for beam-forming is shown in Fig. 6.6. Here, the feed network is designed such that the main lobe points to $\theta = 30°$ and $\phi = 0°$.

Feed networks have been designed for scan angles in the E-plane, H-plane and diagonal (D) plane. The scan angles that have been selected in each plane are 0, 30, 45 and 60 degrees. The performance of each antenna board is verified with the developed MoM model (Spark) and a full-wave finite-volume simulation tool (CST Microwave Studio). The effect of the feed network and the effect of the diffraction at the edges of the board is not accounted for in Spark, whereas CST Microwave Studio incorporates all these effects. In Fig. 6.7, the difference in radiation patterns between the two models is observed. Both models predict a similar main lobe, but CST predicts a higher side lobe level due to the diffraction at the edges of the board and more back radiation due to the radiation of the feed network.

## 6.5    Measurements

### 6.5.1    Antenna element

The optimised antenna element that is used for the antenna arrays is measured following the approach described in Chapter 4. Again, a balun is implemented on the PCB as well as a transition from CPW to MS that is de-embedded from the measurements. The measured and simulated reflection coefficient is shown Fig. 6.8. In this figure, the measured performance is compared with a planar simulation that includes the balun and the metal thickness of the feed. Additionally, the simulated performance of the antenna without balun and zero metal thickness is indicated in the figure as
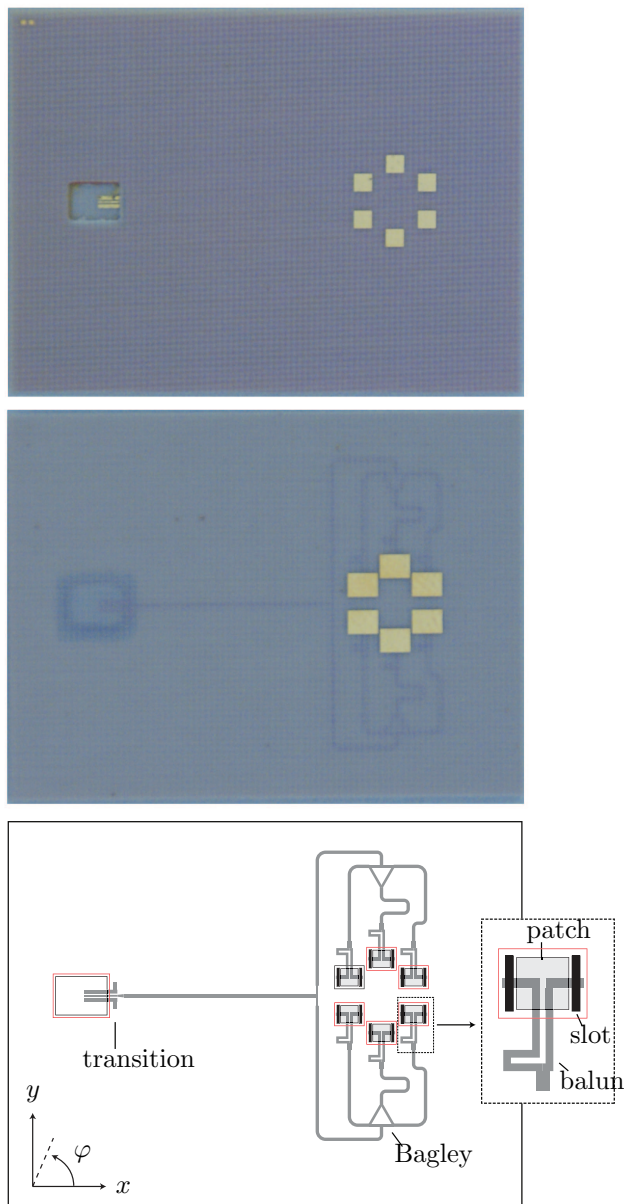
Figure 6.6: Photographs and layout of the circular 6-element array with beam-forming network for 30° scan in $\varphi = 0°$ plane. Top: photograph of the front-side of the antenna array, middle: photograph of the back-side of the antenna array, bottom: layout of the antenna array [inset: geometry of the antenna element and balun].
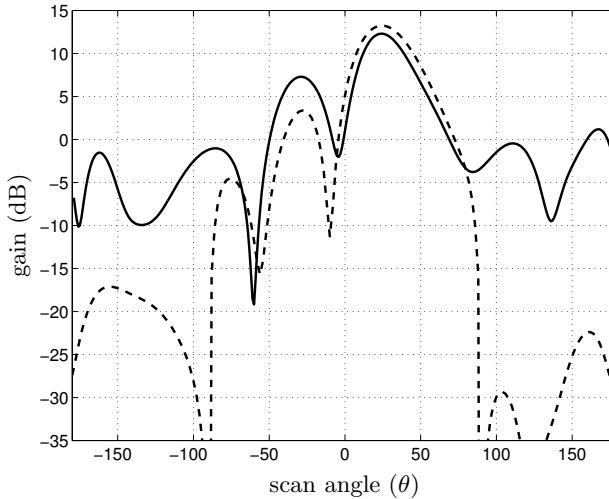
Figure 6.7:  Gain of circular array for $\theta = 30°$ scan in the $\varphi = 0°$ plane.  CST Microwave Studio (solid), Spark (dashed).

well.  Good agreement is observed between the measurement and simulation of the combined antenna and balun.  The resonances of the slots and the patch can be recognized in the measured and simulated curves.  It is observed that the balun introduces some additional mismatch since the simulated reflection coefficient of the antenna without balun remains well below -10 dB (see Fig. 6.8).  Since the simulations and the measurements of the antenna including balun are in good agreement, it is plausible that the performance of the optimised antenna alone is also in good agreement with simulations.  For comparison, the performance of the antenna alone is shown in Fig. 6.8 as well.  It is noted that both Spark and Ansoft Designer predict similar performance for the optimised antenna element (see e.g. Fig. 3.3).

The radiation pattern of the antenna has been measured in the frequency range from 40 to 67 GHz.  The measurements have been conducted in a standard lab environment. To reduce the influence of the environment, time-gating has been applied (see Section 4.3).  The resulting radiation pattern in the E-plane (see also Fig. 4.14) is shown in Fig. 6.9, and is compared with 2 simulations, i.e., a planar simulation (Spark) and a 3-dimensional (3D) simulation (CST microwave studio).  In the 3D simulations, the influence of the finite size of the dielectric layers has been included.

From Fig. 6.9 two important observations can be made.  First, the difference between the simulated patterns clearly shows the effect of the finite size of the dielectric on the radiation pattern.  Due to the scattered surface waves at the edges of the dielectric, a ripple is superimposed on the radiation pattern resulting from the planar simulation. Second, it is shown that the agreement of the measurement and the 3D simulation is rather good.  The radiation pattern shows some asymmetry, which is introduced by the balun.  Because of the balun, the slots are not excited exactly in phase.  Therefore,
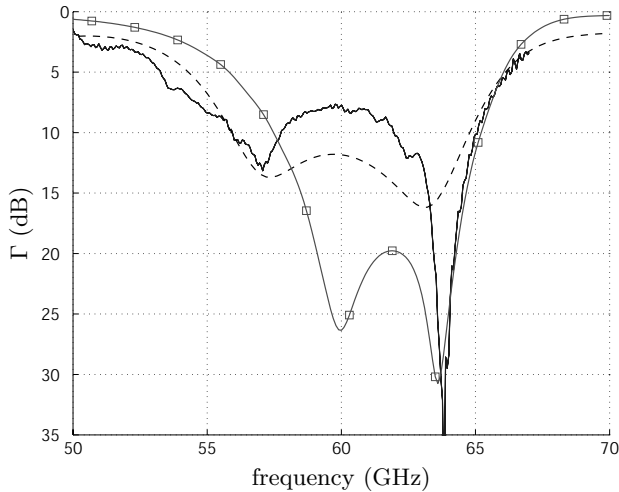
Figure 6.8: Reflection coefficient of the antenna in combination with the balun. Measurement antenna and balun (solid), simulation antenna and balun [Ansoft Designer] (dashed), simulation optimised antenna element [Spark] ($\square$).

the main lobe of the antenna is tilted towards $\theta \approx -20°$ in the E-plane. The ripple that is caused by the radiation from the edges of the dielectric results in the dips in the radiation pattern at $\theta = -40$ and 0 degrees. Fig. 6.9 shows that this effect can be measured as well.

The difference in simulated and measured gain is approximately 2 dB. This is mainly caused by the loss of the feed line that connects the RF probe and the antenna. The total length from probe tip to antenna is 1.5 cm, which results in a feed-line loss of $2/1.5=1.3$ dB/cm. Note that although the feed line is included in the simulations, the feed-line loss could not be accounted for completely. A significant amount of these losses are attributed to the surface roughness of the feed. There is no detailed information about the surface roughness of the realised feed network and therefore this is not included in the simulations. Alternatively, the feed network is simulated as a perfect electric conductor and the feed-line loss is estimated from measurements as 1.3 dB/cm. The H-plane radiation pattern is shown in Fig. 6.10. The measurement in this plane could not be performed all the way up to $\theta = -90$ degrees since the RF probe blocks the radiation in that region (see Fig. 4.14). However, good agreement is observed in the measurement region.

## 6.5.2 Beam-forming antenna arrays

The radiation patterns of the beam-forming antenna arrays are shown in Figs. 6.12-6.14. These figures show the radiation patterns of the circular 6-element antenna
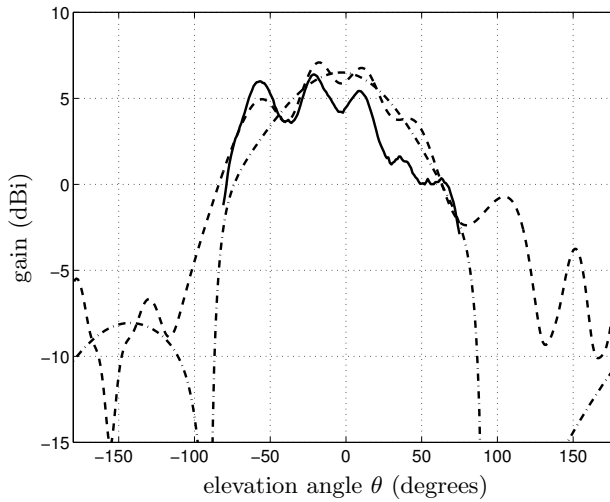
Figure 6.9: Radiation pattern of the combined antenna and balun. E-plane, $f = 60$ GHz. Measurement (solid), CST Microwave Studio (dash), Spark (dash-dot).
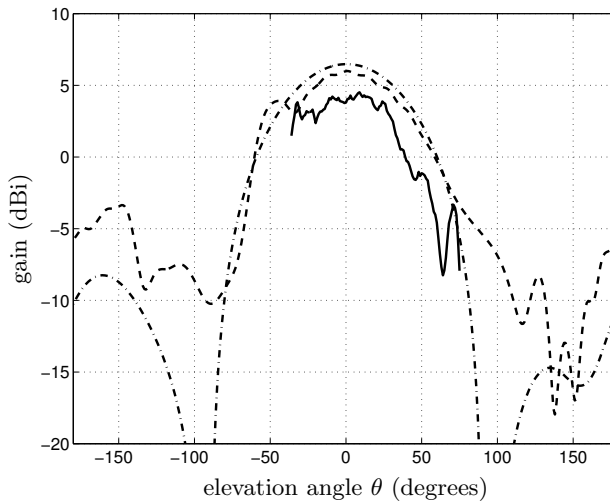


Figure 6.10: Radiation pattern of the combined antenna and balun. H-plane, $f = 60$ GHz. Measurement (solid), CST Microwave Studio (dash), Spark (dash-dot).
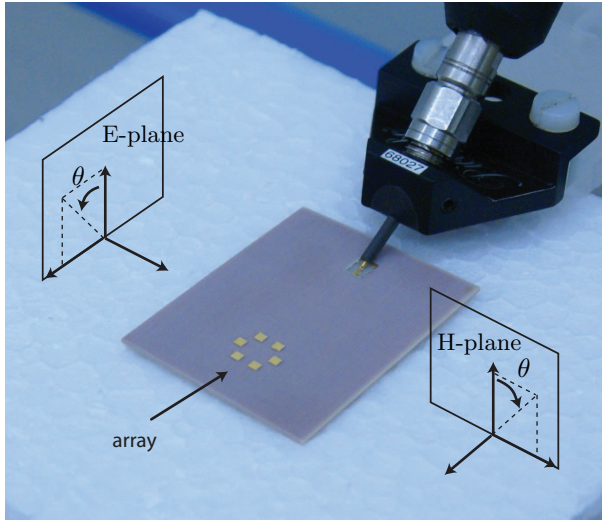
Figure 6.11: Photograph of antenna array and RF probe. The E-plane, H-plane and elevation angle $\theta$ are indicated in the picture.

arrays which scan in elevation angle to $\theta_0 = 0, 30$ and 60 degrees in the H-plane of the array (see Fig. 6.11). The losses in the feed network are not included in the gain measurement to be able to compare the antenna gain with the simulated gain. The loss in the feed network from probe tip to antenna element has been estimated as 4.5 cm times 1.3 dB/cm, which is 5.9 dB. The estimated feed-line loss of 1.3 dB/cm is obtained from the single-element antenna measurement.

The measured radiation patterns are compared with two simulation results. The first comparison is made with the calculated radiation patterns that are obtained with Spark simulations. In these simulations, each antenna element is excited with a delta-gap voltage source that is positioned at dipole feed underneath the antenna element. Therefore these simulations do not incorporate the effect of the feed network. Moreover, it is noted that the finiteness of the dielectric layers is not accounted for as well. The second comparison is made with CST microwave studio. In these simulations, the complete feed network is accounted for as well as the finiteness of the dielectric boards. Although these simulations are computationally intensive, they should give the most reliable results.

If we consider the broadside array (Fig. 6.12), it is observed that both simulations predict a radiation pattern that is very similar to the measured pattern. The measured gain is 11.8 dBi, whereas 12.6 dBi is simulated in the CST simulation and 14.1 dBi is simulated in the Spark simulation. Moreover, the measured and simulated beamwidths differ very little and the side-lobe levels are in good agreement as well. As the scan angle increases (Fig. 6.13, 6.14), the radiation patterns that are simulated with CST remain in good agreement with the measured radiation patterns.
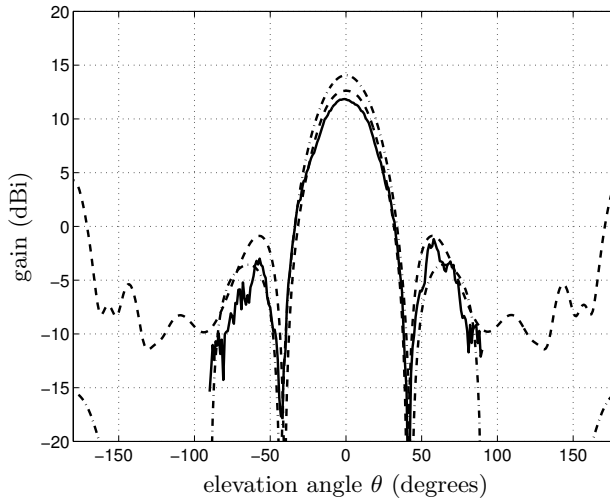
Figure 6.12: Radiation pattern of the circular 6-element array with broadside orientation. H-plane, $f = 60.0$ GHz. Measurement (solid), CST Microwave Studio (dash), Spark (dash-dot).
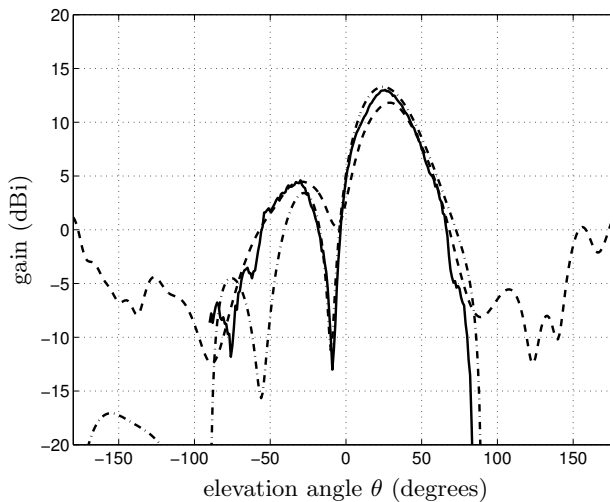


Figure 6.13: Radiation pattern of the circular 6-element array with $\theta_0 = 30°$. H-plane, $f = 60.0$ GHz. Measurement (solid), CST Microwave Studio (dash), Spark (dash-dot).
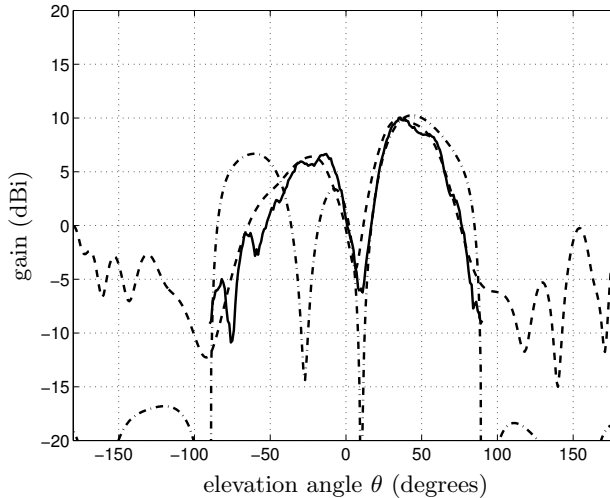
Figure 6.14: Radiation pattern of the circular 6-element array with $\theta_0 = 60°$. H-plane, $f = 60.0$ GHz. Measurement (solid), CST Microwave Studio (dash), Spark (dash-dot).

It is observed that Spark gives a good estimate for the main lobe of the radiation pattern, but some differences are introduced for the side-lobe predictions. This can be explained by noting that the finite size of the dielectric boards is not accounted for in Spark. Because of the scattered field at the edges of the board, the predicted radiation patterns for larger elevation angles become less reliable.

## 6.6   Conclusions

In this chapter, the BFACP antenna has been deployed in an array configuration to improve antenna gain and to enable beam forming. First, the MoM model (Spark) is extended for the analysis of antenna arrays. Hereafter, Spark has been used to compare the performance of several array configurations. From this comparison, a circular 6-element BFACP antenna array has been proposed. The antenna elements in this array have little mutual coupling and the antenna array has a radiation efficiency that is larger than 80% and a directivity that is larger than 12 dBi for a scan range from $\theta = -45°$ to $\theta = +45°$. To demonstrate the performance of the beam-forming antenna array, several antenna arrays have been designed with separate feed networks that provide each antenna element with an RF signal that has the correct phase for a specific scan angle. Beam forming has been successfully demonstrated for discrete scan angles $\theta = 0$, 30 and 60 degrees. Therefore, it is concluded that the BFACP antenna can be successfully employed in beam-forming antenna arrays.

In the transceiver system, the antenna array is connected directly to the active electronics. Instead of using a fixed feed network, active phase shifters are used to provide each antenna element with an RF signal that has an appropriate phase. The integration of the antenna and the active electronics into a single package will be discussed in the next chapter.

# Packaging

## 7.1   Introduction

In the previous chapter it is demonstrated that it is possible to realise beam-forming antenna arrays in PCB technology for the 60-GHz frequency band.  To realise an adaptive beam-forming transceiver, this array should be integrated with active electronics into a single package.  Actually, this is an important issue for the succes of low-cost 60-GHz applications. Packages are needed that integrate all RF components such that the manufacturers of applications do not have to cope with the specialised design challenges that are associated with millimeter-wave RF integration.

In this chapter, it is shown that commonly applied PCB technology can be employed to create a complete package, that supports the transceiver ICs and embeds the antenna array, feed network, passive components and the required control circuitry. At these relatively high frequencies, the integration between IC and antenna needs to be treated carefully to obtain a well-defined interconnection and to avoid undesired losses.  Therefore, flip-chip technology is used to realise the interconnection between IC and PCB. To demonstrate the proposed packaging topology, a power amplifier is integrated with a BFACP antenna element.

## 7.2    Package requirements and topologies

The challenge in package design is the trade-off between a large number of require-
ments that originate from different performance aspects of the transceiver. Obviously,
the transceiver package should have a good RF performance, but other aspects, such
as mechanical rigidity, temperature resistance and moisture protection are important
as well. Different topologies are possible that try to exploit the technical capabilities
of PCB technology to meet these requirements.

### 7.2.1    Package requirements

The most important requirements for the package are listed below (see also [59], [14]):

- The dielectric of the package should be well-suited for antenna performance.
  This implies the use of a dielectric materials with a low dielectric constant to
  improve the bandwidth and radiation efficiency of the antenna. Moreover, the
  dielectric materials should be low-loss to minimise dissipative losses.

- The RF feed network should also be supported by the package. The accuracy
  of the manufacturing process is especially important for the RF feed since, in
  general, the smallest features are used in the RF feed. Tolerances on the width of
  the RF feed directly correspond to changes in the characteristic impedance of the
  RF feed and this results in undesired reflections and mismatch. The dielectric
  material and thickness should be selected carefully to obtain an RF feed network
  with a well-defined impedance and low radiation losses. It is advantageous to
  have a ground plane at a well-defined distance that is relatively close, in terms
  of wavelength, to the RF feed. In this way the radiation losses of the feed are
  minimised. Moreover, the package should be designed such that the feed-line
  interconnections are as short as possible to minimise the associated losses.

- Another aspect that is of importance is the rigidity of the materials and the
  package as a whole. When the ICs are flip-chipped onto the package, the package
  is heated and a certain pressure is applied. The materials should be able to
  withstand these temperatures and pressures without deforming.

- Although the realisation of vias is relatively straightforward in PCB technology,
  it has a significant influence on the RF performance of the package. Vias are
  realised by creating a hole in the dielectric, followed by a metallisation step.
  In this metallisation step, the planar metal parts of the PCB are metallised as
  well and the the copper thickness of the planar structures increases. Even when
  vias are not used in the RF feed network, the RF feed is still affected since
  the copper thickness will increase and the deviations on the realised structure
  become larger. This should be accounted for in the design of the RF feed.

- It is common practice to create an open cavity into a package that is used to recess an IC into. The materials and adhesives should support the realisation of these cavities. For example, the adhesive should not flow into the cavity when the PCB is laminated.

### 7.2.2 Package topologies

**Superstrate topologies**

As already mentioned, the layer underneath the radiating element should feature a low dielectric constant. Therefore, antenna concepts have been introduced that employ an air layer underneath the radiating element [40, 60]. Such antennas are considered as superstrate antennas and this topology can be used to realise high-gain antennas, but can also be optimised for radiation efficiency. For example, consider an aperture-coupled patch antenna that is realised on an air-dielectric substrate configuration (see Fig. 7.1). The radiation efficiency in the upper region (i.e., above the ground plane), depends on the thickness of the dielectric layers. This dependence is shown in Fig. 7.2, where the radiation efficiency is shown for varying thickness of the air layer. It is observed that this efficiency can be as high as 98%.

Although the performance of this topology is very good, the embedding of such an antenna (array) in a package is quite involved. In [40] the antenna has been realised as a separate component that has been placed partly on the transmitter/receiver IC. The extension of this concept to an antenna array is difficult, since the RF feed network is not shielded from the dipole antennas and will therefore distort the performance of the array. In [60] a low-temperature co-fired ceramics (LTCC) manufacturing process has been used. Air cavities have been created underneath the patch antennas to realise the superstrate topology. Although this can be a promising solution, it is very
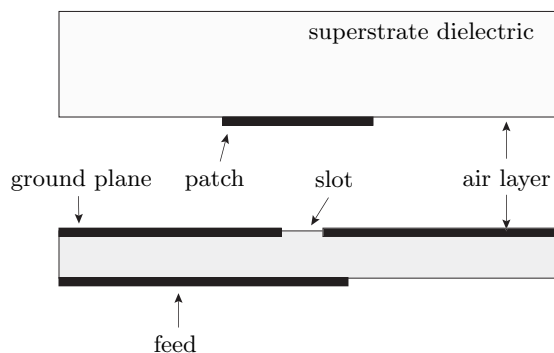


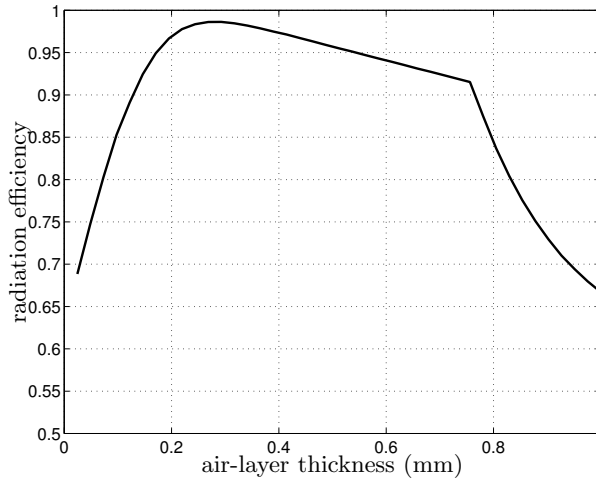Figure 7.1: Aperture coupled patch antenna in superstrate topology.

Figure 7.2: Radiation efficiency of the superstrate aperture-coupled patch antenna for varying air-layer thickness. Simulation with Spark. Frequency = 60 GHz. Superstrate dielectric: $\varepsilon_r = 4$, thickness = 250 $\mu m$. Patch: length = 1.5 cm, width = 1.5 cm. Slot: length = 1.5 cm, width = 0.1 cm.

difficult to create well-defined closed air cavities in a mass-production technology.

Alternatively, the air layer underneath the antenna can be realised by placing solder balls that as a spacer between the radiating patch and the ground plane. In this way, no closed cavities need to be realised. A schematic layout of a possible package is shown in Fig. 7.3. Accurate alignment between the upper and lower dielectrics is needed, although these requirements can be alleviated for broadband antenna designs. The package can be realised from two separate parts that are spaced with solder balls. The lower half of the package can be used to embed the RF feed, IC and control signals, whereas the upper half contains the patch antennas. Vias and pads can be realised to connect to the data and control signals from the outside of the package.

**BFACP antenna package topology**

In a superstrate topology, the package consists of two parts with an air layer in between. These two parts need to be combined in a separate manufacturing step. To avoid this step and further simplify the topology, it is tried to realise a complete package based on a single PCB stack. For this purpose, the BFACP antenna is very well suited. In the prototypes of the BFACP antennas, the dielectric layers have been realised from teflon-based materials (NY9217 [61], $\varepsilon_r = 2.17$). The low dielectric constant of this material and the inherent surface-wave suppression of the antenna element provides a high radiation efficiency and avoids the need for a separate air
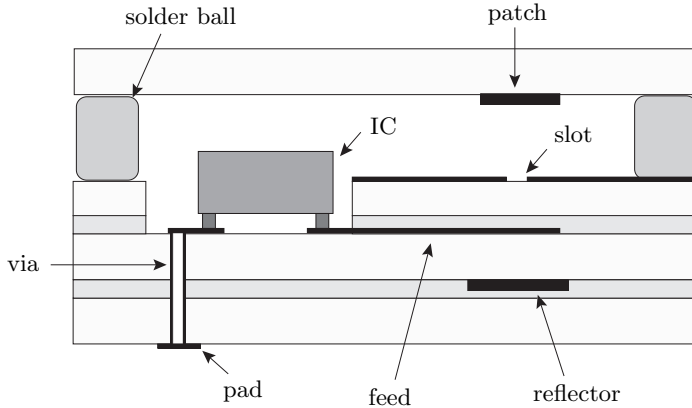
Figure 7.3: Schematic layout of a superstrate antenna package with solder ball spacers.
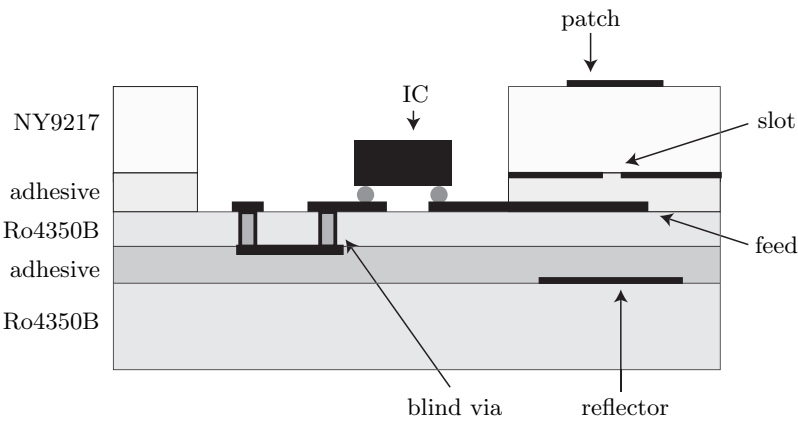


Figure 7.4: Schematic layout of PCB package with integrated IC and antenna.

layer within the PCB stack.

Although teflon-based materials have good RF performance, they cannot be employed to create a complete package. The disadvantages of teflon-based materials are that they are not very rigid and that they have a large thermal expansion coefficient. Therefore, it is difficult to use this material for the realisation of a rigid package and the realisation of vias can be difficult because of the relatively large thermal expansion. An improved PCB stack that can function as a package is shown in Fig. 7.4. The upper layer of this package is realised from teflon-based material to ensure good RF performance. The lower layers are realised from a glass-reinforced hydrocarbon/ceramic material (Ro4350B [62]). This material is much more rigid compared to teflon-based materials and has low dissipative losses as well. The dielectric constant of this material is approximately 3.66 (specified at 10 GHz). The lowest dielectric

layer of the package is used to provide the package with its mechanical rigidity. The middle layer is a thin layer that is used to create a well-defined RF feed. This layer also allows the realisation of vias, such that the routing of control signals can be simplified. The dielectric layers are laminated together with adhesive layers in between that are tailored for adhesion with these materials.

## 7.3    Material characterisation

The electrical properties of teflon-based materials are well-established owing to their stability over a wide frequency band (up to 100 GHz) [63]. The same needs to be investigated for the Rogers Ro4350B material that is used in the package since the available datasheet specifies its properties up to 10 GHz only. For this purpose, a two-port ring resonator has been designed (Fig. 7.5). The resonance frequency of the ring resonator is directly related to the material properties of the dielectric [64], since the resonance frequency of the $n^{\text{th}}$ parallel resonance of the unloaded ring resonator is given by

$$f_{0,n} = \frac{cn}{L\sqrt{\varepsilon_{\text{eff}}}}, \tag{7.1}$$

where $c$ is the speed of light in vacuum, $L$ is the length of the ring resonator and $\varepsilon_{\text{eff}}$ is the effective dielectric constant of the transmission line. From the effective dielectric constant, the dielectric constant can be determined as well [49] through the relation

$$\varepsilon_{\text{eff}} = \frac{\varepsilon_r + 1}{2} + \frac{\varepsilon_r - 1}{2\sqrt{1 + 12\frac{d}{w}}}, \tag{7.2}$$

where $d$ is the thickness of the dielectric and $w$ is the width of the microstrip line. The resonances of the ring can be recognised in the transmission measurement of the two-port structure that peaks near these frequencies. The attenuation constant $\alpha_n$ of the microstrip line can be determined from the quality factor of the transmission peak [64], viz,

$$\alpha_n = \frac{\pi n}{Q_{0,n}L}, \tag{7.3}$$

where $Q_{0,n}$ is the quality factor of $n^{\text{th}}$ resonance of the unloaded ring resonator. The unloaded quality factor is related to the measured (loaded) quality factor $Q_{l,n}$ as

$$Q_{0,n} = \frac{Q_{l,n}}{1 - |S_{21}(f_{0,n})|}. \tag{7.4}$$

Here $S_{21}(f_{0,n})$ represents the transmission at the resonance frequency $f_{0,n}$. Finally, the loaded quality factor is obtained from the double-sided 3 dB bandwidth of the transmission peak, i.e.,

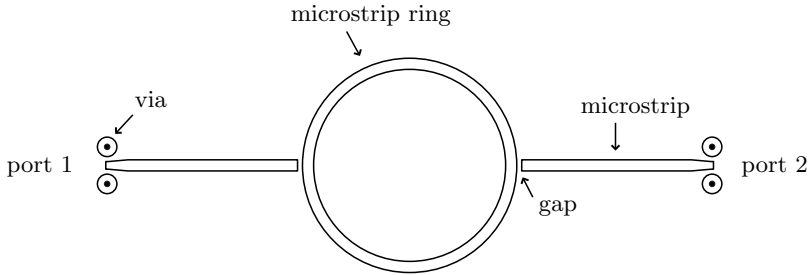$$Q_{l,n} = \frac{f_{0,n}}{B_{\text{3dB},n}}, \tag{7.5}$$

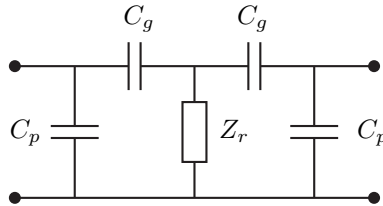Figure 7.5: Layout of microstrip ring resonator.



Figure 7.6: Circuit model of microstrip ring resonator.

where $B_{3\text{dB},n}$ is the double-sided 3 dB bandwidth.

A circuit model of the ring resonator structure can be used to relate the dielectric constant of the dielectric and the transmission peaks of the ring resonator [see [64] and Fig. 7.6]. The transmission peaks do not exactly correspond to the resonance frequency of the unloaded ring resonator since the ring is loaded by the microstrip transmission lines. In the circuit model, this effect is accounted for. The gap between the microstrip transmission line and the ring resonator is modelled as a network with a gap capacitance $C_g$ and parasitic capacitance $C_p$. The values of these capacitances can be determined with a planar simulation of the gap [64]. The impedance of the ring resonator is modelled as

$$Z_r = \frac{Z_0}{2} \coth\left(\frac{\gamma L}{2}\right), \tag{7.6}$$

where $\gamma$ is the complex propagation constant of the microstrip line and $Z_0$ is the characteristic impedance of the microstrip line. The transmission peaks of the circuit model vary with the effective dielectric constant and can be compared with the measured transmission peaks. In this way the dielectric constant of the ring resonator can be determined.

The ring resonator has been designed on a Ro4350B dielectric with a thickness of 101 $\mu$m (4 mil). The length of the ring has been chosen such that the 4$^{\text{th}}$ resonance of the ring lies close to 60 GHz ($L = 11.65$ mm). The width of the microstrip line is 203 $\mu$m, and the metal thickness is 25 $\mu$m. This results in a characteristic
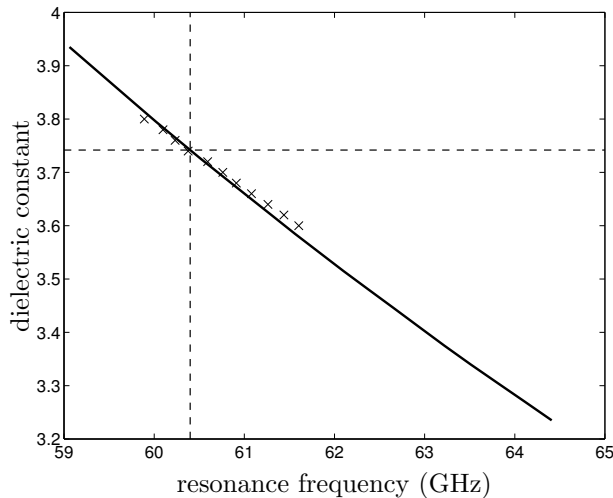
Figure 7.7: Dielectric constant as a function of resonance frequency (4$^{\text{th}}$ resonance). Circuit model (solid), CST Microwave Studio (crosses). The measured value is depicted in the figure with the dashed lines.

impedance of $Z_0 = 50\ \Omega$. The width of the gap between the microstrip transmission line and the ring is 90 $\mu$m, which is the minimum spacing of the PCB manufacturing process. The ring resonator is connected with ground-signal-ground (GSG) RF probes and is measured with a two-port measurement. The transition from GSG probe to microstrip is de-embedded from the measurements (see also Section 4.2.2). For this purpose, through, reflect and line structures have been realised and measured as well.

From the circuit model, the dielectric constant can be obtained as a function of resonance frequency. This relation is shown in Fig 7.7 for the 4$^{\text{th}}$ resonance. To validate the circuit model, the obtained results are compared with full-wave simulations that have been performed with CST Microwave Studio. The discrepancy between the dielectric constants that are predicted by both models lies within 1%. The measured resonance frequency is 60.42 GHz, which implies a dielectric constant of 3.74. As mentioned before, the attenuation can be determined from the 3 dB bandwidth of the transmission peak. This bandwidth is 1.3 GHz, which implies an attenuation constant $\alpha = 23$ Np/m. The corresponding attenuation of the microstrip line is 1.0 dB/cm. A similar analysis has been performed for the other (lower) resonance frequencies as well. These results are listed in Table 7.1. Note that the specified dielectric constant at 10 GHz is 3.66, which implies that the dielectric constant is increased significantly at 60 GHz and therefore the material characterisation is very important.

| n | $f_{0,n}$ [GHz] | $B_{3\text{dB},n}$ [GHz] | $\varepsilon_r$ | attenuation [dB/cm] |
|---|---|---|---|---|
| 1 | 15.24 | 0.49 | 3.67 | 0.38 |
| 2 | 30.46 | 0.69 | 3.66 | 0.53 |
| 3 | 45.55 | 1.0 | 3.69 | 0.77 |
| 4 | 60.42 | 1.3 | 3.74 | 1.0 |

Table 7.1: Measured resonance frequency and 3 dB bandwidth with accompanying dielectric constant and attenuation up to the 4th resonance of the ring resonator.

| Element | Parameter | Value |
|---|---|---|
| patch | length | 1.37 mm |
|  | width | 1.60 mm |
| slots | length | 1.44 mm |
|  | width | 0.20 mm |
|  | spacing | 1.63 mm |
| reflector | length | 2.13 mm |
|  | width | 1.00 mm |
| dipole | length | 2.09 mm |
|  | width | 0.15 mm |
| feed | width | 0.10 mm |
|  | spacing | 0.12 mm |

Table 7.2: Dimensions of the optimised antenna.

## 7.4   BFACP antenna package

To investigate the difficulties that are associated with the implementation of a transceiver package that embeds antennas and electronics, a prototype is built. This prototype embeds a power amplifier (PA) and a BFACP antenna into one package. A schematic layout of the package is shown in Fig. 7.4. The antenna is optimised for this stack following the approach presented in Section 5.5. The frequency band of the optimised antenna ranges from 56 to 65 GHz and the radiation efficiency in this band is larger than 75 % (see Fig. 7.8). The PA is realised in 65 nm CMOS technology and is initially characterised with RF probes that connect directly to the chip. The maximum gain of the PA is about 5-8 dB and the 3 dB gain bandwidth ranges from 54 to 66 GHz.

### 7.4.1   Flip-chip interconnect

To integrate the IC with the antenna, a reliable interconnection needs to be realised. Traditionally, the interconnection between IC and PCB is realised through wire-bonding, but the performance of this type of interconnect decreases rapidly for higher frequencies, because of the large wire inductance that is associated with the
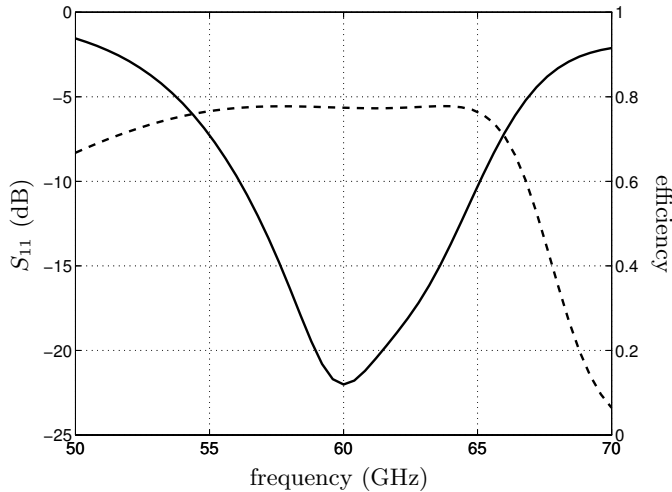
Figure 7.8: Reflection coefficient (solid) and radiation efficiency (dashed) of the optimised antenna. Dimensions in Table 7.2.

wire-bond (see e.g. [65]). Alternatively, flip-chip technologies can be employed to provide a better interconnection, since flip-chip interconnections have lower and more predictable parasitic inductances [15, 59]. In flip-chip technology the metallic pads on the IC are connected to a corresponding set of pads on the PCB using an array of balls or bumps. These balls or bumps can be realised from solder or metal like gold and copper [59]. In this demonstrator, gold stud bumps have been used in combination with an anisotropic conductive adhesive [66]. First, the gold bumps are placed on the pads of the IC. Second, the IC is flipped and pushed onto the PCB (Fig. 7.9). In between the IC and the PCB, an adhesive is placed that contains silver particles. Because of the applied pressure, these particles form a conducting path in between the stud bumps and the PCB pads. A microscopic photograph of the cross-section of such a flip-chip interconnection is shown in Fig. 7.10

## 7.4.2   Chip mount

The layout of the chip mount is shown in Fig. 7.11. This chip mount is designed such that the pads on the PCB correspond with the pads of the PA. The input signal of the PA can be provided through the ground-signal-signal-ground (GSSG) connection on the PCB. Vias have been used to connect al the grounds to a large metal plane underneath the chip mount. The DC supply and bias voltages can be applied to the PA from the PCB as well. RF stubs have been employed to suppress the RF signals on the DC supplies. The output of the PA is connected directly to the differential feed of the antenna.
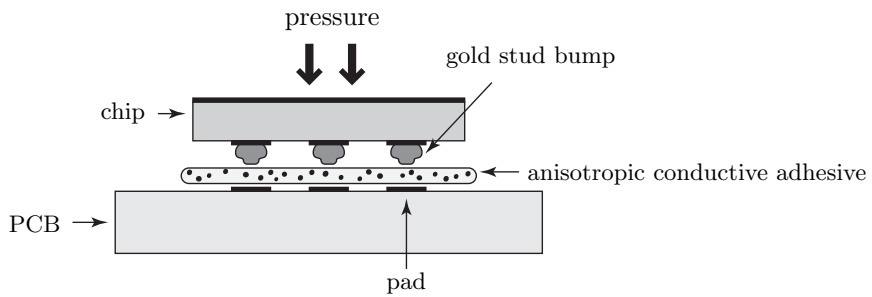
Figure 7.9: Schematic layout of the flip-chip process with gold stud bumps and anisotropic conductive adhesive.
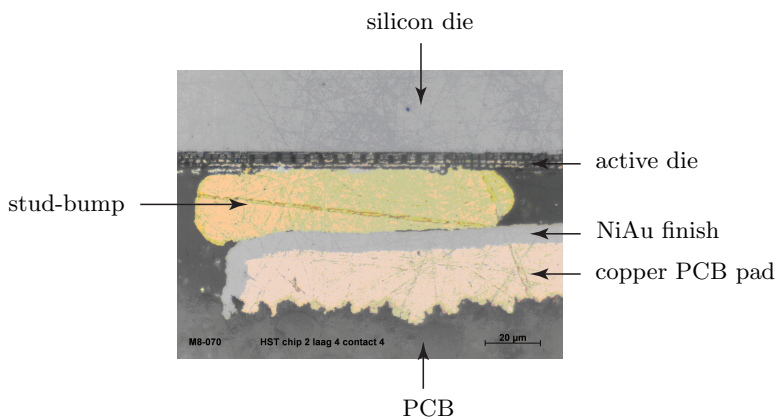


Figure 7.10: Microscopic photograph of the cross-section of a flip-chip interconnection.
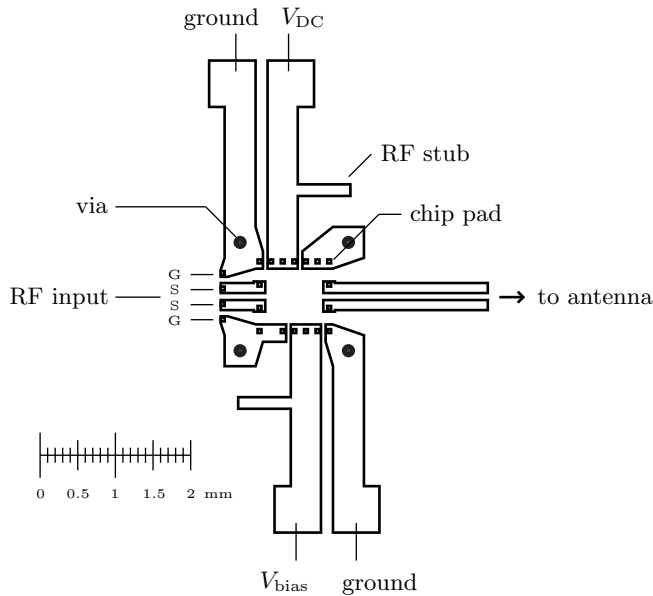
Figure 7.11: Layout of PA chip mount.

| layer | type | name | $\varepsilon_r$ | thickness |
|-------|------|------|------|-----------|
| 1 | teflon-based | NY9217 | 2.17 | 254 $\mu$m |
| 2 | adhesive | SpeedBoard C | 2.6 | 112 $\mu$m |
| 3 | ceramic-based | Ro4350B | 3.74 | 102 $\mu$m |
| 4 | adhesive | Ro4403 | 3.17 | 102 $\mu$m |
| 5 | ceramic-based | Ro4350B | 3.74 | 254 $\mu$m |

Table 7.3: Stack build-up of BFACP antenna package. The layers are numbered from top to bottom.

### 7.4.3 Package

The complete package is depicted in Fig. 7.12. Here, the layout of each layer can be easily identified. The width and length of the package is 18 × 28 mm, whereas the total thickness is 0.82 mm. The used material layers and the corresponding thicknesses are shown in Table 7.3. The CPS feed that connects the PA and the antenna is constructed such that it has a ground plane underneath it near the PA and above it near the antenna. In this way, the characteristic impedance of the differential feed is close to 100 Ω everywhere.
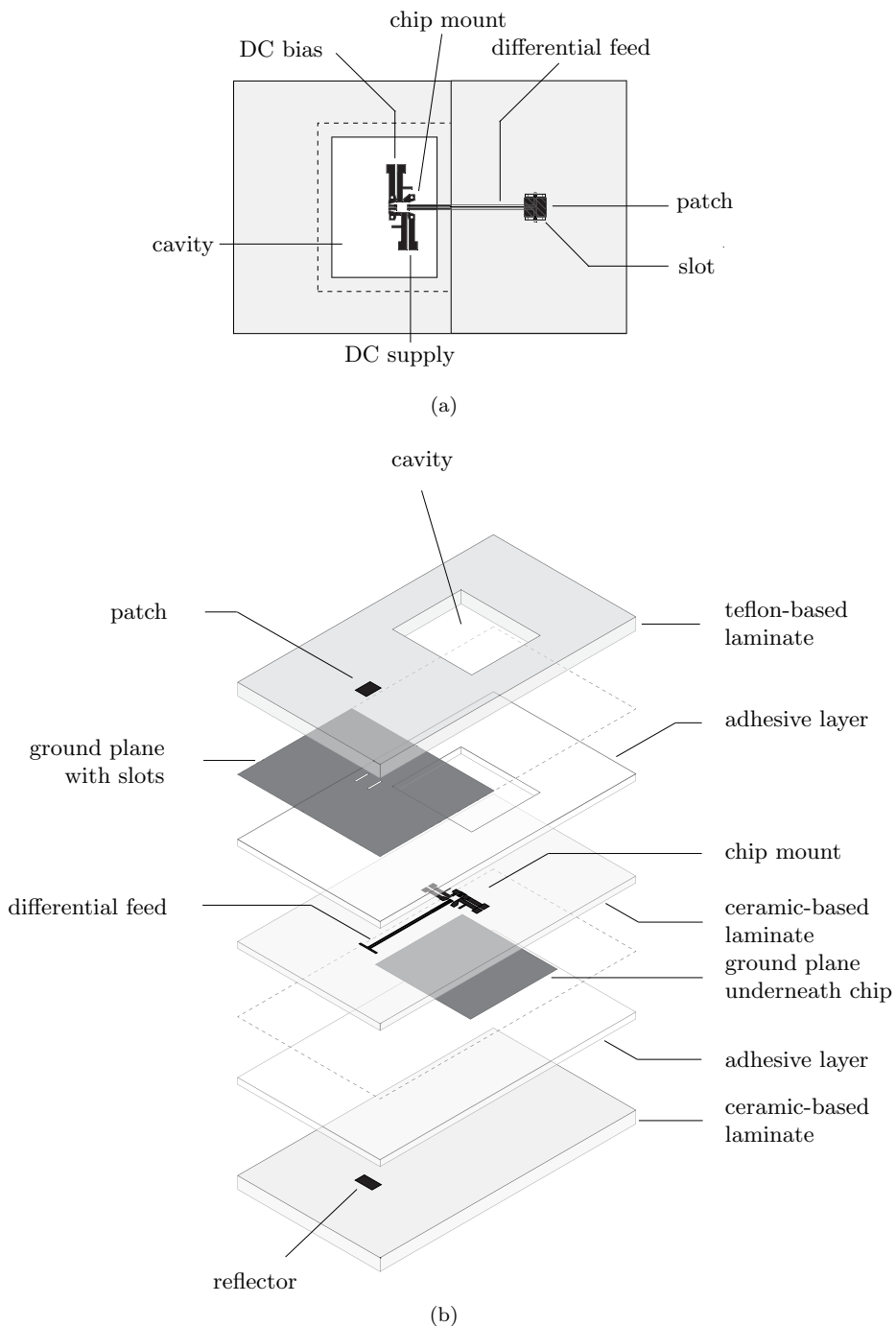
(a)



(b)

Figure 7.12: Layout of BFACP antenna package. (a) Top view of package. (b) Explored view of package.

## 7.4.4 Measurements

To characterise the performance of the packaged PA and antenna (Fig. 7.13), the performance of the antenna is evaluated first. Since the antenna has a differential feed, GSSG RF probes have been used in combination with an external balun to provide the balanced input signal. The RF probe has been calibrated with a one-port load-reflect-match (LRM) calibration. The measured and simulated reflection coefficients are shown in Fig. 7.14. It is observed that the matching of the antenna is below -10 dB in the frequency range from 57.7 to 65.0 GHz. This corresponds well with the gain bandwidth of the PA that ranges from 54 to 66 GHz.

The performance of the packaged PA and antenna has been investigated as well. The operation of this package has been tested on a probe station first (see Fig. 7.15). A GSSG RF probe has been used to connect the RF input signal to the PA. The DC supply and bias voltages have been applied with DC probes. Once the operation of the packages has been verified, the gain of the combined PA and antenna is compared with the gain of the antenna alone (i.e., without PA). To characterise the radiation pattern of the combined PA and antenna, wires have been soldered to the DC bias and supply connections of the package and the radiation patterns are measured on the far-field radiation pattern measurement setup (Section 4.3).

The gain of the antenna alone and the PA-antenna combination is compared in Fig. 7.16. It is observed that the gain of the PA is 0-4 dB lower than the gain of the antenna alone in the operating range of the antenna (57.7 - 65.0 GHz). This implies that the RF losses are equal or larger than the gain of the packaged PA. The main causes for these losses are

- **Mismatch**
  Both the PA and the antenna have been designed for an input and output impedance of 100 $\Omega$; the presence of the flip-chip interconnect can distort the matching between the RF probe and the input of the PA as well as the matching between the output of the PA and the input of the antenna. This can result in mismatch which reduces the gain of the system.

- **Interconnection loss**
  The flip-chip interconnection has been realised with gold stud-bumps in combination with an anisotropic conductive adhesive. This interconnect introduces some dissipative losses due to the finite conductivity of the transition. As a result, the system gain is reduced.

- **PA detuning**
  The PA has been characterised with on-wafer tests. The performance of the PA can be distorted when it is flip-chipped onto the package. This can possibly reduce the gain of the PA.
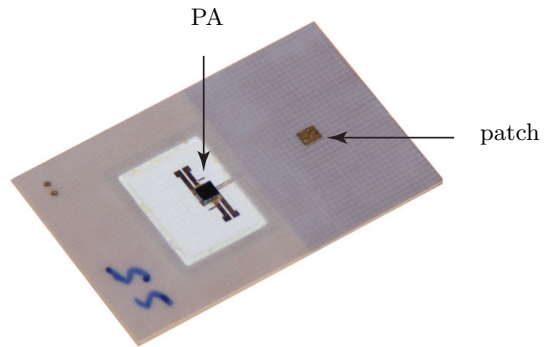
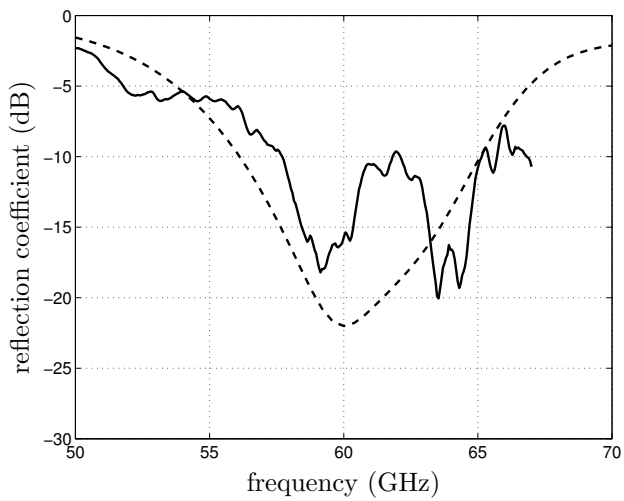Figure 7.13: Photograph of integrated PA and BFACP antena.



Figure 7.14: Reflection coefficient of the packaged BFACP antenna. Measurement (solid), simulation [Spark] (dashed).
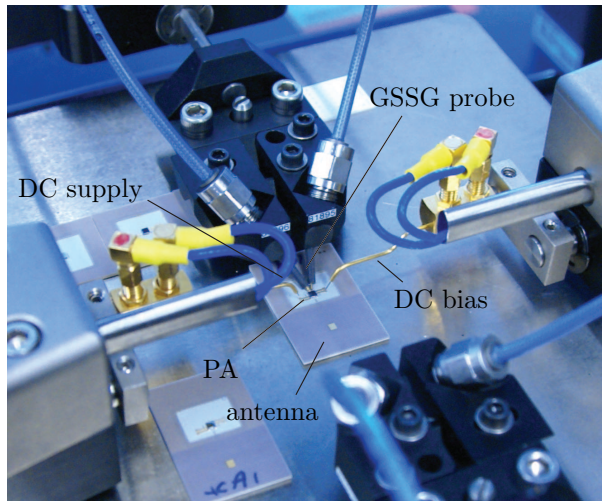
Figure 7.15: Measurement setup of antenna package on probe station.
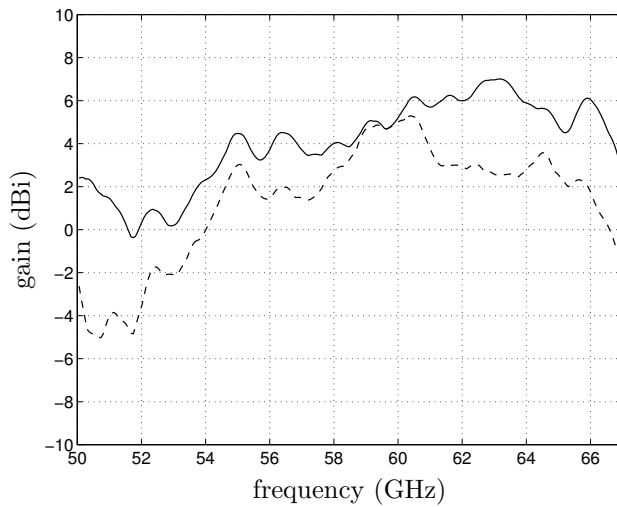


Figure 7.16: Maximum gain of the packaged BFACP antenna with PA (dashed) and without PA (solid).
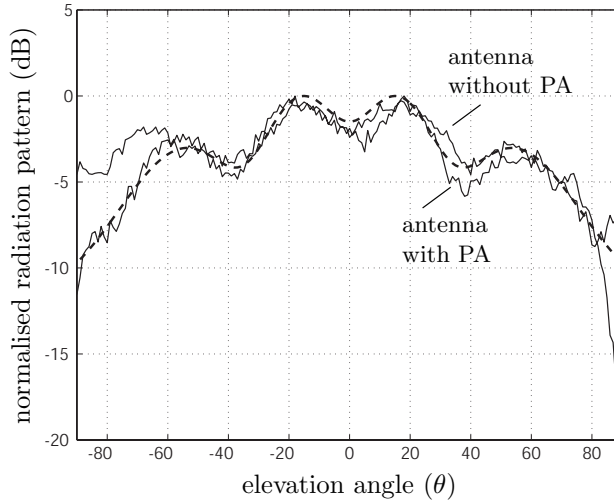
Figure 7.17: Measured radiation pattern of packaged antenna and power amplifier. E-plane, frequency $f = 60$ GHz. Measurements of antenna pattern with and without PA (solid), simulated radiation pattern [CST Microwave Studio] (dashed).

The normalised radiation patterns are compared in Fig. 7.17. It is observed that both measured radiation patterns are very similar. This indicates that the power is radiated by the antenna alone and no significant amount of power is radiated by the RF probe, the PA or the flip-chip transitions. Moreover, it is observed from Fig. 7.17 that the radiated patterns are in good agreement with simulated results.

## 7.5  Conclusions

In this chapter, the realisation of a transceiver package has been investigated. This transceiver package integrates the BFACP antenna array, active electronics, RF feed and control circuitry. First, the requirements on the package have been listed. Hereafter, several packaging topologies have been discussed and a specific topology has been proposed for the integration of the BFACP antenna and a PA. This topology has been designed in detail and the performance of the integrated module has been measured. It has been demonstrated that the embedded antenna shows good performance, viz a measured bandwidth that ranges from 57.7 to 65.0 GHz and a maximum gain of 7 dBi. Moreover, it has been shown that the BFACP antenna can be integrated with a PA although the gain of the PA-antenna combination is lower then expected. Possible causes for this reduction in gain have been discussed and will be a topic for future research.

# Summary, conclusions and outlook

## 8.1   Summary and conclusions

The 60-GHz frequency band can be employed to realise the next-generation wireless high-speed communication that is capable of handling data rates of multiple gigabits per second. Advances in silicon technology allow the realisation of low-cost radio frequency (RF) front-end solutions. Still, to obtain the link-budget that is required for wireless gigabit-per-second communication, antenna arrays are needed that have sufficient gain and that support beam-forming. This requires the realisation of antenna arrays that maintain a high radiation efficiency while operating at millimeter-wave frequencies. Moreover, the antenna array and the RF front-end should be integrated into a single low-cost package that can be realised in a standard production process. In this thesis, antenna solutions have been presented that meet these requirements. This work covers the complete development cycle, viz modelling, design, optimisation, manufacturing, measurement and verification for three antenna prototype generations. An in-depth view of each development step is provided, while the combined work provides an overview of millimeter-wave antenna development.

Modelling is a crucial step in the development cycle and has been discussed in Chapter 2. The production processes that are used for antenna design and packaging realise planar multi-layered structures. Therefore, the modelling of electromagnetic

(EM) structures in stratified media has been considered. First, the Green's function for stratified media has been derived. Second, a MoM-based approach has been proposed that provides an accurate analysis of the physical behaviour of these structures. Special attention has been given to the analysis of surface waves that propagate in the planar geometry, because they can significantly affect the radiation efficiency of planar antennas. The resulting model provides a computationally efficient tool (Spark) for the analysis and design of a wide range of planar antenna topologies.

The first prototype is the balanced-fed aperture-coupled patch (BFACP) antenna element, that employs a unique topology and therefore exhibits excellent performance regarding bandwidth and radiation efficiency. The modelling and design of this antenna has been discussed in Chapter 3. It has been shown that the use of two coupling slots improves the bandwidth of the antenna as well as the radiation efficiency. Simultaneously, the back radiation is significantly reduced by employing a reflector element. The resulting antenna design has a measured bandwidth of 15% in combination with a radiation efficiency that is larger than 80% and an accompanying measured gain of 5.6 dBi. In Chapter 3, an extension of the BFACP antenna element has been presented that supports dual polarisation and/or circular polarisation as well. The proposed BFACP antenna designs can be employed both as single-element antenna and as a building block for antenna arrays.

Obviously, the accurate measurement of the manufactured antenna prototypes is of importance for verification of both the modelling methods and the antenna designs. For this purpose, specific measurement setups have been designed. In Chapter 4 these setups have been introduced, motivated and explained. To obtain a reliable interconnection between the measurement equipment and the antenna under test, RF probes have been employed. Additional transitions (coplanar waveguide to microstrip transition, balun) have been designed to convert the single-ended signal of the measurement equipment to the balanced signal that is required by the antenna under test. Moreover, a far-field radiation pattern measurement setup has been developed from scratch which is completely tailored for the measurement of millimeter-wave antennas and beam-forming antenna arrays. It has been shown that these setups provide reliable measurement data that is in good agreement with the results obtained from the derived models.

To maximise the performance of the antenna, an optimisation algorithm has been presented in Chapter 5 that gives the designer the flexibility to obtain the best antenna design for the considered application. This algorithm extends the derived EM model of the BFACP antenna (Chapter 3) to include sensitivity information about design parameters. The sensitivity has been employed to jointly optimise the bandwidth and the radiation efficiency of the antenna element. In Chapter 6, the optimised antenna element is used in the design of antenna arrays. Here, the modelling of beam-forming antenna arrays is discussed and the performance of several array configurations is compared. It has been concluded that a 6-element circular array shows best performance in terms of gain and radiation efficiency. Moreover, the mutual coupling between

the elements of this array is low such that the active reflection coefficient remains well below -10 dB throughout the entire scan range. A second prototype has been designed that demonstrates beam-forming. For this prototype, 6-element circular arrays have been designed in combination with fixed feed networks that provide each antenna element with an RF signal that has the appropriate phase for beam-forming to a specific angle. The performance of these antenna arrays has been investigated in terms of radiation efficiency, bandwidth and gain. The prototype has a maximum measured gain of 11.8 dBi for broadside scan and it has been shown that these antenna arrays can be readily employed for the realisation of adaptive beam-forming at millimeter-wave frequencies.

Chapter 7 discusses the packaging of the transceiver. First, the package requirements are listed and several package topologies are discussed. For example, the performance of superstrate topologies is analysed. Additionally, a package is proposed that embeds the BFACP antenna. This package combines ceramic-based layers and teflon-based layers. The ceramic-based layers provide the package with stiffness and are used to realise the RF feed network, whereas the teflon-based layers are employed to allow an antenna design that has a high radiation efficiency. For a high-performance package design, it is important that the electrical properties of the materials used is well-defined. Therefore, special efforts have been undertaken to characterise the electrical material properties of the materials used at millimeter-wave frequencies. For this purpose, ring resonators have been designed. Measurement results indicate that the electrical properties at higher frequencies can differ significantly from the values that are specified by the manufacturer for an operating frequency of 10 GHz. To demonstrate the performance of the BFACP antenna in a package configuration, a third prototype has been developed, in which the BFACP antenna is packaged in combination with active electronics. This prototype demonstrates that the antenna can be embedded in a package that contains not only the antenna, but also the RF electronics, RF feed network and control circuitry. In the prototype, the BFACP antenna has been connected to a power amplifier that has been realised in CMOS technology. The PA has been connected to the RF feed through a flip-chip interconnection process. It has been demonstrated that the proposed packaging topology results in an efficient transmitter.

In conclusion, three antenna prototype generations have been presented and it is demonstrated that the presented concepts can be readily used for the design of a transceiver package that embeds a beam-forming antenna array and that supports gigabit-per-second communication.

## 8.2   Outlook

In the future, millimeter-wave transceivers will be developed for a wide range of applications. Apart from the employment of the millimeter-wave frequency bands for

broadband communication, other applications arise. An example of such an application is automobile radar [67] that has an allocated frequency band around 76 GHz. Automobile radar can be used for collision avoidance and traffic routing. These systems will soon be available on all cars and this also drives the development of millimeter-wave transceivers. Another application example is millimeter-wave imaging. With this technique it is possible to scan persons and equipment for hidden objects [68]. It is believed by many that it is an application with a lot of interest and market potential.

### 8.2.1   Full-fledged beam-forming transceiver

For the realisation of these applications, full-fledged beam-forming transceivers are needed that are completely packaged. It is stressed that the concepts that are presented in this thesis can be directly applied for the realisation of such transceivers. Currently, a lot of effort is put into the development of radio chips that embed the complete RF circuitry into a single chip. That is, the RF front-end except for the antennas. These chips include the VCO, mixers, phase shifters, PAs and/or LNAs. For these chips, silicon-based technologies are used to obtain low-cost solutions. It is believed that SiGe-based technology is already capable of delivering the performance that is needed for current-day applications, whereas CMOS technology, although the lowest-cost option, is not there yet. However, it will probably get there within a few years. Concepts that integrate these chips and antenna arrays into a single package are discussed in detail in Chapter 7 and [P1, P2]. The exploitation of these concepts allows the development of full-fledged beam-forming transceivers.

### 8.2.2   Antennas on chip

Another approach that is discussed in literature is the development of on-chip antennas [7], [8] or on-chip antenna arrays. If the antennas can be placed directly on the chip, interconnection and packaging problems can be partly avoided. However, there are several major drawbacks to this approach, viz,

- **Radiation efficiency**
  The radiation efficiency of these antenna will be very low, because of three important reasons:

  - Surface waves
    Silicon has a dielectric constant that is close to 12. Because of this high dielectric constant, antenna structures will excite a lot of surface waves. These surface waves will decrease antenna performance significantly. Moreover, they are likely to prohibit the design of beam-forming antenna arrays.

- Dielectric losses
  The resistivity of the silicon substrate in standard silicon processes is rather low. This results in large dissipative losses in the dielectric and prohibits antenna designs with a high radiation efficiency.

- Metal losses
  The metal that is employed in chip technologies is very thin ($t_m < 1 \ \mu m$) and is known to have large losses at millimeter-wave frequencies. In comparison, the loss of on-chip transmission lines is typically about 20 dB/cm, whereas the loss on PCB is about 1 dB/cm.

- **Cost**
  Although the size of antennas decreases as the frequency increases, the antenna structures are still quite large in comparison with the total chip size. This is especially the case for antenna arrays. Note that the distance between the antenna elements should be close to half a free-space wavelength. This puts stringent requirements on the chip dimensions and therefore, it is probably not the lowest-cost option to place the antennas on the chip.

- **Packaging topology**
  If the antennas are placed on the chip, the designer has no freedom to create a package in which antennas and RF electronics are shielded from each other. Moreover, flip-chip technologies cannot be employed since the chip cannot be placed upside down if antennas are located on top of the chip.

It is not ruled out that the use of on-chip antennas can be a solution for specific applications. However, it is pointed out that it is not envisioned as a suitable candidate for the next generation full-fledged beam-forming millimeter-wave transceivers.

### 8.2.3 Three-dimensional antennas

An aspect that is not discussed in detail in this work is the scan range of the antenna arrays. Ideally, the antennas should be able to direct their beams towards every possible direction. In practice, this is not possible since planar arrays have been employed. The planar structure limits the scan range of an antenna array roughly to $\theta = \pm 60°$ in elevation (see e.g. Fig. 6.5). A possible solution is the development of three-dimensional millimeter-wave antenna arrays. If the antenna array can be placed on a three-dimensional structure, the scan range can be enhanced and the coverage of the transceiver can be improved significantly. A three-dimensional antenna array solution is presented in Fig. 8.1 and [69], where a pyramid-shaped structure is placed on top of a planar antenna array. Each side of the pyramid structure is a passive planar transmit array that improves both the gain and scan range of the planar source array [69].
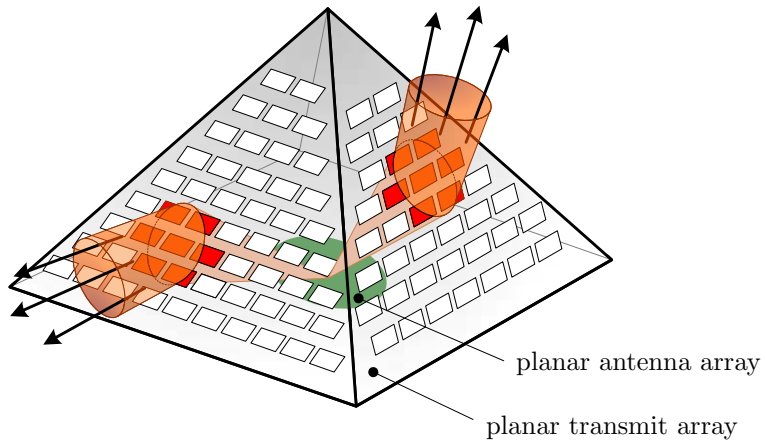
Figure 8.1: Planar antenna array with pyramid-shaped lens antenna. Each side of the pyramid acts as a planar transmit array that deflects the incoming electromagnetic waves towards a new direction.

# Green's function for stratified media

## A.1  Amplitude coefficients source layer

### A.1.1  Electric-current point source

**$x$-directed point source**

The boundary conditions for an $x$-directed electric-current point source in the spectral domain can be derived from (2.10) as

$$
\begin{aligned}
\hat{E}_x^u &= \hat{E}_x^d, \\
\hat{E}_y^u &= \hat{E}_y^d, \\
\hat{H}_x^u &= \hat{H}_x^d, \\
\hat{H}_y^u - \hat{H}_y^d &= -1.
\end{aligned}
\tag{A.1}
$$

From these boundary conditions, the amplitude coefficients in the source layer can be determined as (see also Section 2.4.3)

$$
\begin{aligned}
K_{A,u} &= \frac{jk_x\mu^{n_s}(1-\Gamma_{A,d}^{n_s})}{2k_\rho^2(1-\Gamma_{A,u}^{n_s}\Gamma_{A,d}^{n_s})}, \\
K_{F,u} &= \frac{jk_y\omega\mu^{n_s}\varepsilon^{n_s}(1+\Gamma_{F,d}^{n_s})}{2k_z^{n_s}k_\rho^2(1-\Gamma_{F,u}^{n_s}\Gamma_{F,d}^{n_s})}, \\
K_{A,d} &= -\frac{jk_x\mu^{n_s}(1-\Gamma_{A,u}^{n_s})}{2k_\rho^2(1-\Gamma_{A,u}^{n_s}\Gamma_{A,d}^{n_s})}, \\
K_{F,d} &= \frac{jk_y\omega\mu^{n_s}\varepsilon^{n_s}(1+\Gamma_{F,u}^{n_s})}{2k_z^{n_s}k_\rho^2(1-\Gamma_{F,u}^{n_s}\Gamma_{F,d}^{n_s})}.
\end{aligned}
\tag{A.2}
$$

### $y$-directed point source

For an $y$-direction electric-current source, the amplitude coefficients can be determined from the amplitude coefficients of the $x$-directed electric-current source by an interchange of $k_x$ and $k_y$, i.e.,

$$
\begin{aligned}
K_{A,u} &= \frac{jk_y\mu^{n_s}(1-\Gamma_{A,d}^{n_s})}{2k_\rho^2(1-\Gamma_{A,u}^{n_s}\Gamma_{A,d})^{n_s}}, \\
K_{F,u} &= \frac{jk_x\omega\mu^{n_s}\varepsilon^{n_s}(1+\Gamma_{F,d}^{n_s})}{2k_z^{n_s}k_\rho^2(1-\Gamma_{F,u}^{n_s}\Gamma_{F,d}^{n_s})}, \\
K_{A,d} &= -\frac{jk_y\mu^{n_s}(1-\Gamma_{A,u}^{n_s})}{2k_\rho^2(1-\Gamma_{A,u}^{n_s}\Gamma_{A,d}^{n_s})}, \\
K_{F,d} &= \frac{jk_x\omega\mu^{n_s}\varepsilon^{n_s}(1+\Gamma_{F,u}^{n_s})}{2k_z^{n_s}k_\rho^2(1-\Gamma_{F,u}^{n_s}\Gamma_{F,d}^{n_s})}.
\end{aligned}
\tag{A.3}
$$

### $z$-directed point source

Now, consider a $z$-directed electric-current point source. In a homogeneous medium, the Green's functions for this case can be derived from the requirement on the divergence of the electric-flux density (2.5) and the continuity equation (2.6), viz,

$$
\nabla \cdot \mathbf{E}(\mathbf{r}) = \frac{\rho_s(\mathbf{r})}{\varepsilon_r} = -\frac{1}{j\omega\varepsilon_r}\nabla \cdot \mathbf{J}(\mathbf{r}).
\tag{A.4}
$$

For a $z$-directed point source $\mathbf{J}(\mathbf{r}) = \delta(\mathbf{r}-\mathbf{r}_s)\mathbf{u}_z$ this results in

$$
\partial_z E_z(\mathbf{r}) = -\frac{1}{j\omega\varepsilon_r}\partial_z\delta(\mathbf{r}-\mathbf{r}_s),
\tag{A.5}
$$

which can be written in the spectral domain as

$$\partial_z \hat{E}_z(k_x, k_y, z) = -\frac{1}{j\omega\varepsilon_r}\partial_z\delta(\mathbf{z}-\mathbf{z}_s)e^{jk_x x_s + jk_y y_s}. \tag{A.6}$$

Next, the left-hand and right-hand terms of (A.6) are integrated with respect to $z$ and $\hat{E}_z$ is substituted with the relation given in (2.26), i.e.,

$$-j\omega\hat{A}_z(k_x, k_y, z) - \frac{j\omega}{k^2}\partial_z^2\hat{A}_z(k_x, k_y, z) = -\frac{1}{j\omega\varepsilon_r}\delta(\mathbf{z}-\mathbf{z}_s)e^{jk_x x_s + jk_y y_s}. \tag{A.7}$$

Using (2.15) this is reformulated as

$$-\frac{j\omega}{k^2}[k^2 + \partial_z^2]\hat{G}_{zz}^{AJ,h}(k_x, k_y, z|\mathbf{r_s}) = -\frac{1}{j\omega\varepsilon_r}\delta(\mathbf{z}-\mathbf{z}_s)e^{jk_x x_s + jk_y y_s}, \tag{A.8}$$

where $\hat{G}_{zz}^{AJ,h}$ is a component of the spectral dyadic Green's function of the magnetic vector potential for a homogeneous medium. A solution for this Green's function can be obtain from (A.8) by variation of constants and is given by (see also [18])

$$\hat{G}_{zz}^{AJ,h}(k_x, k_y, z|\mathbf{r_s}) = \frac{\mu}{2jk_z}e^{-jk_z|z-z_s|}e^{jk_x x_s + jk_y y_s}. \tag{A.9}$$

To obtain the Green's functions for a $z$-directed electric-current point source in a stratified medium, the solution in (A.9) is augmented to the solutions given in (2.22), (2.23) for the homogeneous regions directly above and below the source, i.e.,

$$\hat{G}_{zz,u}^{AJ,n_s}(k_x, k_y, z|\mathbf{r}_s) = \left\{ K_{A,u}^{n_s}\left[e^{-jk_z^{n_s}(z-z_s)} + \Gamma_{A,u}^{n_s}e^{jk_z^{n_s}(z-z_s)}\right] + \right.$$
$$\left. \frac{\mu}{2jk_z^{n_s}}e^{-jk_z^{n_s}(z-z_s)}\right\}e^{jk_x x_s + jk_y y_s},$$
$$\hat{G}_{zz,u}^{FJ,n_s}(k_x, k_y, z|\mathbf{r}_s) = K_{F,u}^{n_s}\left[e^{-jk_z^{n_s}(z-z_s)} + \Gamma_{F,u}^{n_s}e^{jk_z^{n_s}(z-z_s)}\right]e^{jk_x x_s + jk_y y_s},$$
$$\hat{G}_{zz,d}^{AQ,n_s}(k_x, k_y, z|\mathbf{r}_s) = \left\{ K_{A,d}^{n_s}\left[e^{jk_z^{n_s}(z-z_s)} + \Gamma_{A,d}^{n_s}e^{-jk_z^{n_s}(z-z_s)}\right] + \right. \tag{A.10}$$
$$\left. \frac{\mu}{2jk_z^{n_s}}e^{jk_z^{n_s}(z-z_s)}\right\}e^{jk_x x_s + jk_y y_s},$$
$$\hat{G}_{zz,d}^{FQ,n_s}(k_x, k_y, z|\mathbf{r}_s) = K_{F,d}^{n_s}\left[e^{jk_z^{n_s}(z-z_s)} + \Gamma_{F,d}^{n_s}e^{-jk_z^{n_s}(z-z_s)}\right]e^{jk_x x_s + jk_y y_s}.$$

Next, from the boundary conditions that the tangential electric and magnetic fields should be continuous, the amplitude coefficients can be obtained as

$$K_{A,u} = \frac{j\mu^{n_s}(1 + \Gamma_{A,d}^{n_s})}{2k_z^{n_s}(1 - \Gamma_{A,u}^{n_s}\Gamma_{A,d}^{n_s})},$$
$$K_{F,u} = 0,$$
$$K_{A,d} = \frac{j\mu(1 + \Gamma_{A,u}^{n_s})}{2k_z^{n_s}(1 - \Gamma_{A,u}^{n_s}\Gamma_{A,d}^{n_s})}, \tag{A.11}$$
$$K_{F,d} = 0.$$

### A.1.2    Magnetic-current point source

The magnetic-current point source is dual to the electric-current point source. For an $x$-directed magnetic-current point source, the amplitude coefficients are given as

$$
\begin{aligned}
K_{A,u} &= -\frac{jk_y\omega\mu^{n_s}\varepsilon^{n_s}(1+\Gamma_{A,d}^{n_s})}{2k_z^{n_s}k_\rho^2(1-\Gamma_{A,u}^{n_s}\Gamma_{A,d}^{n_s})}, \\
K_{f,u} &= \frac{jk_x\varepsilon^{n_s}(1-\Gamma_{F,d}^{n_s})}{2k_\rho^2(1-\Gamma_{F,u}^{n_s}\Gamma_{F,d}^{n_s})}, \\
K_{A,d} &= -\frac{jk_y\omega\mu^{n_s}\varepsilon^{n_s}(1+\Gamma_{A,u}^{n_s})}{2k_z^{n_s}k_\rho^2(1-\Gamma_{A,u}^{n_s}\Gamma_{A,d}^{n_s})}, \\
K_{F,d} &= -\frac{jk_x\varepsilon^{n_s}(1-\Gamma_{F,u}^{n_s})}{2k_\rho^2(1-\Gamma_{F,u}^{n_s}\Gamma_{F,d}^{n_s})}.
\end{aligned}
\tag{A.12}
$$

Again, the amplitude coefficients for an $y$-directed magnetic-current point source can be obtained from the amplitude coefficients of the $x$-directed mangetic-current point source by an interchange of $k_x$ and $k_y$.

In a homogeneous medium, the $zz$-component of the spectral dyadic Green's function for the electric vector potential is given by [compare with (A.9)]

$$
\hat{G}_{zz}^{FM,h}(k_x,k_y,z|\mathbf{r_s}) = \frac{\varepsilon}{2jk_z}e^{-jk_z|z-z_s|}e^{jk_xx_s+jk_yy_s}.
\tag{A.13}
$$

Following the same approach as in the case of a $z$-directed electric-current point source (previous section), the amplitude coefficients can be determined as

$$
\begin{aligned}
K_{A,u} &= 0, \\
K_{F,u} &= \frac{j\varepsilon^{n_s}(1+\Gamma_{F,d}^{n_s})}{2k_z^{n_s}(1-\Gamma_{F,u}^{n_s}\Gamma_{F,d}^{n_s})}, \\
K_{A,d} &= 0, \\
K_{F,d} &= \frac{j\varepsilon^{n_s}(1+\Gamma_{F,u}^{n_s})}{2k_z^{n_s}(1-\Gamma_{F,u}^{n_s}\Gamma_{F,d}^{n_s})}.
\end{aligned}
\tag{A.14}
$$

# Derivative of the reflection coefficient

It is shown that the derivative of the reflection coefficient $\Gamma(\omega, \mathbf{p})$ and the radiation efficiency $\eta(\omega, \mathbf{p})$ with respect to the parameter vector $\mathbf{p}$ can be expressed in terms of $\nabla_{\mathbf{p}} \mathbf{V}$ and $\nabla_{\mathbf{p}} \mathbf{Z}$. The derivative of the reflection coefficient can be determined as

$$
\begin{aligned}
\nabla_{\mathbf{p}} \Gamma(\omega, \mathbf{p}) &= \nabla_{\mathbf{p}} \frac{Z_{\text{in}}(\omega, \mathbf{p}) - Z_0}{Z_{\text{in}}(\omega, \mathbf{p}) + Z_0} \\
&= \frac{\nabla_{\mathbf{p}} Z_{\text{in}}(\omega, \mathbf{p})}{Z_{\text{in}}(\omega, \mathbf{p}) + Z_0} \\
&\quad - \frac{Z_{\text{in}}(\omega, \mathbf{p}) - Z_0}{(Z_{\text{in}}(\omega, \mathbf{p}) + Z_0)^2} \nabla_{\mathbf{p}} Z_{\text{in}}(\omega, \mathbf{p}).
\end{aligned}
\tag{B.1}
$$

From this point on, the dependencies of $\mathbf{V}(\omega, \mathbf{p}), \mathbf{I}(\omega, \mathbf{p})$ and $\mathbf{Z}(\omega, \mathbf{p})$ are omitted. The derivative of the input impedance is written as

$$
\begin{aligned}
\nabla_{\mathbf{p}} Z_{\text{in}}(\omega, \mathbf{p}) &= \nabla_{\mathbf{p}} \frac{\mathbf{V}_k}{\mathbf{I}_k} \\
&= \frac{\nabla_{\mathbf{p}} \mathbf{V}_k}{\mathbf{I}_k} - \frac{\mathbf{V}_k}{\mathbf{I}_k^2} \nabla_{\mathbf{p}} \mathbf{I}_k,
\end{aligned}
\tag{B.2}
$$

where $\mathbf{V}_k, \mathbf{I}_k$ denotes the $k^{\text{th}}$ element of the vectors $\mathbf{V}$ and $\mathbf{I}$, which represent the voltage and current at the port. The derivative of the current can be expressed as

$$
\begin{aligned}
\nabla_{\mathbf{p}} \mathbf{I} &= \nabla_{\mathbf{p}} [\mathsf{Z}^{-1} \mathbf{V}] \\
&= \mathsf{Z}^{-1} \Big( \nabla_{\mathbf{p}} \mathbf{V} - [\nabla_{\mathbf{p}} \mathsf{Z}] \mathbf{I} \Big).
\end{aligned}
\tag{B.3}
$$

The derivative of the radiation efficiency is found from

$$
\begin{aligned}
\nabla_{\mathbf{p}} \eta(\omega, \mathbf{p}) &= \nabla_{\mathbf{p}} \frac{P^{\text{rad,I}}(\omega, \mathbf{p})}{P^{\text{I}}(\omega, \mathbf{p}) + P^{\text{II}}(\omega, \mathbf{p})} \\
&= \frac{\nabla_{\mathbf{p}} P^{\text{rad,I}}(\omega, \mathbf{p})}{P^{\text{I}}(\omega, \mathbf{p}) + P^{\text{II}}(\omega, \mathbf{p})} \\
&\quad - \frac{P^{\text{rad,I}}(\omega, \mathbf{p})[\nabla_{\mathbf{p}}(P^{\text{I}}(\omega, \mathbf{p}) + P^{\text{II}}(\omega, \mathbf{p}))]}{(P^{\text{I}}(\omega, \mathbf{p}) + P^{\text{II}}(\omega, \mathbf{p}))^2},
\end{aligned}
\tag{B.4}
$$

where the derivative of the radiated power in Region I is

$$
\begin{aligned}
\nabla_{\mathbf{p}} P^{\text{rad,I}}(\omega, \mathbf{p}) &= \nabla_{\mathbf{p}} \frac{1}{2} \text{Re}\{\mathbf{I}^H \mathsf{Z}^{k_0} \mathbf{I}\} \\
&= \frac{1}{2} \text{Re}\Big\{ [\nabla_{\mathbf{p}} \mathbf{I}^H] \mathsf{Z}^{k_0} \mathbf{I} + \mathbf{I}^H [\nabla_{\mathbf{p}} \mathsf{Z}^{k_0}] \mathbf{I} + \mathbf{I}^H \mathsf{Z}^{k_0} [\nabla_{\mathbf{p}} \mathbf{I}] \Big\}.
\end{aligned}
\tag{B.5}
$$

The matrix $\mathsf{Z}^{k_0}$ represents the elements of the matrix $\mathsf{Z}$ of Eq. (3.5) that reside in region I. The elements of the $\mathsf{Z}^{k_0}$ matrix are computed with the integral over $k_\rho$ of the matrix terms restricted to $k_\rho \in [0, k_0]$, as explained in Section 2.7. Finally, the derivative of the total power is obtained as

$$
\begin{aligned}
\nabla_{\mathbf{p}} (P^{\text{I}}(\omega, \mathbf{p}) + P^{\text{II}}(\omega, \mathbf{p})) &= \nabla_{\mathbf{p}} \frac{1}{2} \text{Re}\{\mathbf{I}^H \mathsf{Z} \mathbf{I}\} \\
&= \frac{1}{2} \text{Re}\Big\{ [\nabla_{\mathbf{p}} \mathbf{I}^H] \mathsf{Z} \mathbf{I} + \mathbf{I}^H [\nabla_{\mathbf{p}} \mathsf{Z}] \mathbf{I} + \mathbf{I}^H \mathsf{Z} [\nabla_{\mathbf{p}} \mathbf{I}] \Big\}.
\end{aligned}
\tag{B.6}
$$

# Glossary

## General notation

| notation | description |
|---|---|
| $x$ | scalar or index |
| $\mathbf{x}$ | three-dimensional vector |
| $\mathbf{X}$ | three-dimensional vector with harmonic time-dependence |
| $\boldsymbol{\mathcal{X}}$ | three-dimensional vector with arbitrary time-dependence |
| $x_i$ | $i$-oriented component of $\mathbf{x}$ |
| $X_i$ | $i$-oriented component of $\mathbf{X}$ |
| $\underline{\underline{\mathbf{X}}}$ | dyadic |
| $\overline{\mathsf{X}}$ | matrix or column-vector |
| $\mathbb{X}$ | operator |

## Acronyms

| abbreviation | description |
|---|---|
| AUT | antenna under test |
| BFACP | balanced-fed aperture-coupled patch |
| CPS | coplanar microstrip |
| CPW | coplanar waveguide |
| EBG | electromagnetic bandgap |
| EFIE | electric-field integral equation |
| EM | electromagnetic |

| | |
|---|---|
| GSG | ground-signal-ground |
| GSSG | ground-signal-signal-ground |
| IC | integrated circuit |
| kbps | kilobit per second |
| LNA | low-noise amplifier |
| LOS | line of sight |
| LRM | load-reflect-match |
| Mbps | megabit per second |
| MFIE | magnetic-field integral equation |
| MoM | method-of-moments |
| MS | microstrip |
| PA | power amplifier |
| PCB | printed circuit-board |
| PEC | perfect electric conductor |
| PMCHW | Poggio Miller Chang Harrington Wu |
| RF | radio frequency |
| RFIC | radio frequency integrated circuit |
| RX | receiver |
| TX | transmitter |
| WLAN | wireless local area network |
| WPAN | wireless personal area network |

# Bibliography

[1] "Code of Federal Regulation, Title 47 Telecommunication," Tech. Rep. Section 15.255, U.S. Federal Communications Commission, 2004.

[2] "Code of Federal Regulation, Title 47 Telecommunication," Tech. Rep. Section 15.247, U.S. Federal Communications Commission, 2007.

[3] B. Razavi, *RF microelectronics.* Upper Saddle River: Prentice Hall, 1998.

[4] B. A. Floyd, S. K. Reynolds, U. R. Pfeiffer, T. Zwick, T. Beukema, and B. Gaucher, "SiGe bipolar transceiver circuits operating at 60 GHz," *IEEE J. Solid-State Circuits*, vol. 40, pp. 156–167, January 2005.

[5] B. Razavi, "A 60-GHz CMOS receiver front-end," *IEEE J. Solid-State Circuits*, vol. 41, pp. 17–22, January 2006.

[6] K. Scheir, S. Bronckers, J. Borremans, P. Wambacq, and Y. Rolain, "A 52GHz phased-array receiver front-end in 90nm digital CMOS," in *IEEE Int. Solid-state Circuits Conf.*, (San Francisco, USA), pp. 184–185, February 2008.

[7] Y. Zhang, M. Sun, and L. Guo, "On-chip antennas for 60-GHz radios in silicon technology," *IEEE Trans. Electron. Devices*, vol. 52, pp. 1664–1668, July 2005.

[8] C. Lin, S. Hsu, C. Hsu, and H. Chuang, "A 60-GHz millimeter-wave CMOS RFIC-on-chip triangular monopole antenna for WPAN applications," in *Antennas Propagat. Soc. Int. Sym.*, (2522-2525), IEEE, June 2007.

[9] P. Smulders, H. Yang, and J. Akkermans, "On the design of low-cost 60-GHz radios for multigigabit-per-second transmission over short distances," *IEEE Commun. Mag.*, vol. 45, pp. 44–51, December 2007.

[10] W. L. Stutzman and G. A. Thiele, *Antenna theory and design.* Chichester: Wiley, 2nd ed., 1998.

[11] H. Yang, M. Herben, J. Akkermans, and P. Smulders, "Impact analysis of directional antennas and multi-antenna beamformers on radio transmission," *IEEE Trans. Veh. Technol.*, vol. 57, pp. 1695–1707, May 2008.

[12] H. Visser, *Array and phased array antenna basics.* Chichester: Wiley, 2005.

[13] R. J. Mailloux, *Phased array antenna handbook.* London: Artech House, 2nd ed., 2005.

[14] D. Liu and B. Gaucher, "Design considerations for millimeter wave antennas within a chip package," in *IEEE Int. Workshop Anti-counterfeiting, Security, Identification*, pp. 13–17, April 2007.

[15] A. Jentzsch and W. Heinrich, "Theory and measurements of flip-chip interconnects for frequencies up to 100 GHz," *IEEE Trans. Microwave Theory Tech.*, vol. 49, pp. 871–878, May 2001.

[16] R. F. Harrington, *Field computation by moment methods.* New York: IEEE Press, 1993. original edition: 1968.

[17] N. K. Das and D. M. Pozar, "A generalized spectral-domain Green's function for multilayer dielectric substrates with application to multilayer transmission lines," *IEEE Trans. Microwave Theory Tech.*, vol. 35, pp. 326–335, March 1987.

[18] W. C. Chew, *Waves and fields in inhomogeneous media.* Piscataway: IEEE Press, 1995.

[19] J. Mosig, *Numerical techniques for microwave and millimetre-wave passive structures*, ch. 3. Integral equation technique. New York: Wiley, 1989.

[20] E. J. Rothwell and M. J. Cloud, *Electromagnetics.* London: CRC Press, 2001.

[21] A. Sommerfeld, *Partial differential equations in physics.* New York: Academic Press, 1949.

[22] D. B. Davidson, *Computational electromagnetics for RF and microwave engineering.* Cambridge: Cambridge University Press, 2005.

[23] A. Poggio and E. Miller, *Computer techniques for electromagnetics*, ch. 4. Integral equation solutions of three-dimensional problems, pp. 159–265. Berlin: Springer-Verlag, 1987.

[24] W. H. Press, S. A. Teukolsky, and W. T. Vetterling, *Numerical recipes in C: The art of scientific computing.* Cambridge: Cambridge University Press, 2nd ed., 1992.

[25] The Numerical Algorithms Group Ltd, Oxford, UK, *NAG Fortran Library*, 2001.

[26] A. Smolders, *Microstrip phased-array antennas: a finite-array approach.* PhD thesis, Eindhoven University of Technology, 1994.

[27] R. W. Jackson and D. M. Pozar, "Full-wave analysis of microstrip open-end and gap discontinuities," *IEEE Trans. Microwave Theory Tech.*, vol. 33, pp. 1036–1042, October 1985.

[28] T. F. Eibert and V. Hansen, "Full wave modeling of electrically wide microstrip open end discontinuities via a deterministic spectral domain method," in *Microwave Symposium Digest*, vol. 3, pp. 1155–1158, May 1990.

[29] Ansoft, Pittsburgh, USA, *Ansoft Designer*. http://www.ansoft.com.

[30] CST Computer Simulation Technology, Darmstadt, Germany, *CST Microwave Studio*. http://www.cst.com.

[31] S. Rao, D. Wilton, and A. Glisson, "Electromagnetic scattering by surfaces of arbitrary shape," *IEEE Trans. Antennas Propagat.*, vol. 30, pp. 409–418, May 1982.

[32] T. Weiland, "A discretization method for the solution of Maxwell's equations for six-component fields," *Electronics and Communications AEÜ*, vol. 31, no. 3, pp. 116–120, 1977.

[33] T. H. Lee, *The design of CMOS radio-frequency integrated circuits*. Cambridge: Cambridge University Press, 2nd ed., 2004.

[34] N. Alexopoulos, P. Katehi, and D. Rutledge, "Substrate optimization for integrated circuit antennas," *IEEE Trans. Microwave Theory Tech.*, vol. 83, pp. 550–557, July 1983.

[35] D. Jackson, J. Williams, A. Bhattacharyya, R. Smith, S. Buchheit, and S. Long, "Microstrip patch designs that do not excite surface waves," *IEEE Trans. Antennas Propagat.*, vol. 41, pp. 1026–1037, August 1993.

[36] G. Gauthier, A. Courtay, and G. Rebeiz, "Microstrip antennas on synthesized low dielectric-constant substrates," *IEEE Trans. Antennas Propagat.*, vol. 45, pp. 1310–1314, August 1997.

[37] A. Weily, L. Horvath, K. Esselle, B. Sanders, and T. Bird, "A planar resonator antenna based on a woodpile EBG material," *IEEE Trans. Antennas Propagat.*, vol. 53, pp. 216–223, January 2005.

[38] F. Yang and Y. Rahmat-Samii, "Reflection phase characterizations of the EBG ground plane for low profile wire antenna applications," *IEEE Trans. Antennas Propagat.*, vol. 51, pp. 2691–2703, October 2003.

[39] N. Llombart, A. Neto, G. Gerini, and P. de Maagt, "Planar circularly symmetric EBG structures for reducing surface waves in printed antennas," *IEEE Trans. Antennas Propagat.*, vol. 53, pp. 3210–3218, October 2005.

[40] T. Zwick, D. Liu, and B. Gaucher, "Broadband planar superstrate antenna for integrated millimeterwave transceivers," *IEEE Trans. Antennas Propagat.*, vol. 54, pp. 2790–2796, October 2006.

[41] T. Brauner, R. Vogt, and W. Bachtold, "A differential active patch antenna element for array applications," *IEEE Microwave Compon. Lett.*, vol. 13, pp. 161–163, April 2003.

[42] D. Pozar, "A microstrip antenna aperture coupled to a microstrip line," *Electron. Lett.*, vol. 21, pp. 49–50, January 1985.

[43] S. Targonski and R. Waterhouse, "Reflector elements for aperture and aperture coupled microstrip antennas," in *Antennas Propagat. Soc. Int. Sym.*, vol. 3, pp. 1840–1843, IEEE, July 1997.

[44] G. V. Eleftheriades and M. Qiu, "Efficiency and gain of slot antennas and arrays on thick dielectric substrates for millimeter-wave applications: A unified approach," *IEEE Trans. Antennas Propagat.*, vol. 50, pp. 1088–1098, August 2002.

[45] J. Huang, "The finite ground plane effect on the microstrip antenna radiation patterns," *IEEE Trans. Antennas Propagat.*, vol. 31, pp. 649–653, July 1983.

[46] P. L. Sullivan and D. H. Schaubert, "Analysis of an aperture coupled microstrip antenna," *IEEE Trans. Antennas Propagat.*, vol. 34, pp. 977–984, August 1986.

[47] V. Rumsey, "Reaction concept in electromagnetic theory," *Phys. Rev.*, vol. 94, pp. 1483–1491, June 1954.

[48] M. Qiu, M. Simcoe, and G. Eleftheriades, "Radiation efficiency of printed slot antennas backed by a ground reflector," in *Antennas Propagat. Soc. Int. Sym.*, vol. 3, pp. 1612–1615, IEEE, July 2000.

[49] D. Pozar, *Microwave engineering*. Chichester: Wiley, 3rd ed., 2005.

[50] R. Simons, "Novel on-wafer radiation pattern measurement technique for mems actuator based reconfigurable patch antennas," in *24th. Ann. Antenna Measure. Tech. Assoc. Meeting Symp.*, (Cleveland, OH), November 2002.

[51] J.-P. Raskin, G. Gauthier, L. P. Katehi, and G. M. Rebeiz, "W-Band single-layer vertical transitions," *IEEE Trans. Microwave Theory Tech.*, vol. 48, pp. 161–164, January 2000.

[52] E. Haug, K. Choi, and V. Komkov, *Design sensitivity analysis of structural systems*. London: Academic Press, 1986.

[53] G. V. Eleftheriades and J. R. Mosig, "On the network characterization of planar passive circuits using the method of moments," *IEEE Trans. Microwave Theory Tech.*, vol. 44, pp. 438–445, March 1996.

[54] R. C. Hansen, *Phased array antennas*. New York: Wiley-Interscience, 1998.

[55] N. Amitay, V. Galindo, and C. Wu, *Theory and analysis of phased array antennas*. New York: Wiley-Interscience, 1972.

[56] D. M. Pozar and D. H. Schaubert, "Scan blindness in infinite phased arrays of printed dipoles," *IEEE Trans. Antennas Propagat.*, vol. 32, pp. 602–610, June 1984.

[57] D. M. Pozar, "Analysis of finite phased arrays of printed dipoles," *IEEE Trans. Antennas Propagat.*, vol. 33, pp. 1045–1053, October 1985.

[58] A. W. Rudge, K. Milne, A. Olver, and P. Knight, *The handbook of antenna design.* Institution of Engineering and Technology, 1983.

[59] R. K. Ulrich and W. D. Brown, *Advanced electronic packaging.* New York: Wiley, 2nd ed., 2006.

[60] A. E. I. Lamminen, J. Säily, and A. R. Vimpari, "60-GHz patch antennas and arrays on LTCC with embedded-cavity substrates," *IEEE Trans. Antennas Propagat.*, vol. 56, pp. 2865–2874, September 2008.

[61] Park Electrochemical Corporation, Melville, USA, *Nelco RF / Microwave circuitry materials.*

[62] Rogers Corporation, Chandler, USA, *RO4000 Series high frequency circuit materials.*

[63] T. Zwick, A. Chandrasekhar, C. W. Baks, U. R. Pfeiffer, S. Brebels, and B. P. Gaucher, "Determination of the complex permittivity of packaging materials at millimeter-wave frequencies," *IEEE Trans. Microwave Theory Tech.*, vol. 54, pp. 1001–1010, March 2006.

[64] J. R. Bray and L. Roy, "Microwave characterization of a microstrip line using a two-port ring resonator with an improved lumped-element model," *IEEE Trans. Microwave Theory Tech.*, vol. 51, pp. 1540–1547, May 2003.

[65] A. Sutono, N. Cafaro, J. Laskar, and M. Tentzeris, "Experimental modeling, repeatability investigation and optimization of microwave bond wire interconnects," *IEEE Trans. Adv. Packag.*, vol. 24, pp. 595–603, November 2001.

[66] J. Jordan, "Gold stud bump in flip-chip applications," in *Int. Electronics Manufacturing Technol. Sym.*, pp. 110–114, IEEE/SEMI International, 2002.

[67] W. Jones, "Keeping cars from crashing," *IEEE Spectrum*, vol. 38, pp. 40–45, September 2001.

[68] J. Federici, D. Gary, R. Barat, and Z. Michalopoulou, "T-Rays vs. terrorists," *IEEE Spectrum*, vol. 44, pp. 47–52, July 2007.

[69] M. Kastelijn and J. Akkermans, "Planar passive electromagnetic deflector for millimeter-wave frequencies," *IEEE Antennas Wirel. Propag. Lett.*, vol. 7, pp. 105–107, 2008.

# Publications

## Related publications

### Journal papers

[J1] J. Akkermans, M. Herben, and M. van Beurden, "Balanced-fed planar antenna for millimeter-wave transceivers," *IEEE Trans. Antennas Propag.*, July 2009. accepted for publication.

[J2] J. Akkermans and M. Herben, "Millimeter-wave antenna with adjustable polarization," *IEEE Antennas Wirel. Propag. Lett.*, vol. 7, pp. 539-542, 2008.

[J3] M. Kastelijn and J. Akkermans, "Planar passive electromagnetic deflector for millimeter-wave frequencies," *IEEE Antennas Wirel. Propag. Lett.*, vol. 7, pp. 105–107, 2008.

[J4] H. Yang, M. Herben, J. Akkermans, and P. Smulders, "Impact analysis of directional antennas and multi-antenna beamformers on radio transmission," *IEEE Trans. Veh. Technol.*, vol. 57, pp. 1695–1707, May 2008.

[J5] P. Smulders, H. Yang, and J. Akkermans, "On the design of low-cost 60-GHz radios for multigigabit-per-second transmission over short distances," *IEEE Commun. Mag.*, vol. 45, pp. 44–51, December 2007.

### International conferences

[C1] U. Johanssen, A. Smolders, R. Mahmoudi, and J. Akkermans, "Substrate loss reduction in antenna-on-chip design," in *IEEE Int. Symp. on Antennas and Propagat. (AP-S 09)*, (Charleston, USA), June 2009. submitted.

[C2] J. Akkermans, M. Kazim, Y. Yu, M. Herben, P. Baltus, and P. Smulders, "Flip-chip integration of differential CMOS power amplifier and antenna in PCB technology for the 60-GHz band," in *European Conf. on Antennas and Propagat. (EuCAP09)*, (Berlin, Germany), March 2009.

[C3] D. Liu, J. Akkermans, and B. Floyd, "A superstrate patch antenna for 60-GHz applications," in *European Conf. on Antennas and Propagat. (EuCAP09)*, (Berlin, Germany), March 2009.

[C4] R. van Dijk, A. Neto, J. Akkermans and J. Mills, "EBG-based 60-GHz on-chip antenna in passive silicon" in *European Microwave Conf. (EuMC08)*, (Amsterdam, The Netherlands), November 2008.

[C5] J. Akkermans and M. Herben, "Planar beam-forming array for broadband communication in the 60 GHz band," in *European Conf. Antennas and Propagat. (EuCAP07)*, (Edinburgh, UK), November 2007.

[C6] J. Akkermans, R. van Dijk, and M. Herben, "Millimeter-wave antenna measurement," in *European Microwave Conf. (EuMC07)*, (München, Germany), pp. 83–86, October 2007.

[C7] J. Akkermans and M. Herben, "Sensitivity analysis and optimisation of electromagnetic structures," in *Int. Symp. Electromagn. Theory (EMTS-07)*, (Ottawa, Canada), July 2007.

[C8] J. Akkermans, M. van Beurden, and M. Herben, "Design of a millimeter-wave balanced-fed aperture-coupled patch antenna," in *European Conf. on Antennas and Propagat. (EuCAP06)*, (Nice, France), pp. 1–6, November 2006.

## International workshops

[W1] J. Akkermans and D. Liu, "Antennas and packaging for millimeter-wave phased-array transceivers," in *European Microwave Conf. (EuMC08)*, Workshop on System in Package Technologies for Microwave and Millimeter Wave Integration, (Amsterdam, The Netherlands), October 2008.

## Patent applications

[P1] J. Akkermans, B. Floyd, and D. Liu, "Radio frequency (RF) integrated circuit (IC) packages having characteristics suitable for mass production", *US Patent Application Number 12/168,328*, July 2008.

[P2] J. Akkermans, B. Floyd, and D. Liu, "Radio frequency (RF) integrated circuit (IC) packages with integrated aperture-coupled patch antenna(s) in ring and/or offset cavities", *US Patent Application Number 12/102,051*, April 2008.

# Other publications

## Journal papers

[OJ1] J. Akkermans, M. van Beurden, G. Doodeman, and H. Visser, "Analytical models for low-power rectenna design," *IEEE Antennas Wirel. Propag. Lett.*, vol. 4, pp. 187–190, 2005.

[OJ2] W. Heath, A. Wills, and J. Akkermans, "A sufficient condition for the stability of optimizing controllers with saturating actuators," *Int. J. Robust Nonlinear Control*, vol. 15, pp. 515–529, 2005.

## International conferences

[OC1] A. Wills, W. Heath, and J. Akkermans, "A sufficient robustness condition for constrained model predictive control," in *UKACC Control*, (Bath, UK), September 2004.

[OC2] J. Akkermans, A. Wills, and W. Heath, "Robust cross-directional control of paper making machines with saturating actuators," in *Control Systems*, (Quebec City, Canada), June 2004.

# Samenvatting

De 60-GHz frequentieband kan benut worden om de nieuwe generatie draadloze breed-bandcommunicatie te realiseren met bijbehorende datasnelheden van meerdere giga-bits per seconde. Door de vooruitgang in silicium chiptechnologie is het mogelijk om goedkope radiozendontvangers te realiseren. Echter, antennestelsels zijn nodig die voldoende versterking hebben en bundelvorming ondersteunen om het linkbudget te halen dat vereist is voor draadloze communicatie met deze hoge datasnelheden. Daarom is het belangrijk om antennestelsels te ontwikkelen die efficiënt werken op millimetergolffrequenties. Bovendien moet deze antenna met radio elektronica geïnte-greerd worden in een goedkope module die gemaakt kan worden in een standaard productie proces. In dit proefschrift is een antenna oplossing beschreven die aan deze eisen voldoet.

De relevante productieprocessen die voor antennes en radiomodules worden gebruikt realiseren vlakke gelaagde structuren. Daarom is de modellering van elektromagne-tische structuren in gelaagde media onderzocht. Een methode wordt gebruikt die een gedetailleerde analyse mogelijk maakt van het fysieke gedrag van het elektromagne-tische object. Deze modelleringstechniek vergt een beperkte rekenkracht en is ge-bruikt om een antenne-element te ontwerpen dat ook in een antennestelsel geplaatst kan worden. Dit antenne-element is een mikrostripantenne die via twee aperturen koppelt met een gebalanceerde voeding. In het ontwerp wordt de stralingsefficiëntie verbeterd door het gebruik van deze twee aperturen zodanig dat verliesgevende opper-vlaktegolven worden onderdrukt. Tevens vergroten de aperturen te bandbreedte van de antenne. Verder is een reflector toegevoegd om de straling van de antenne te min-imaliseren in de achterwaartse richting. De genoemde ontwerpstrategieën zijn gecom-bineerd om de prestaties van de antenne te verbeteren. De antenne is gerealiseerd in printplaattechnologie. Om de prestaties van het antenne element te verifiëren is een speciale meetopstelling ontwikkeld die het mogelijk maakt om de bandbreedte en het stralingspatroon van millimetergolfantennes te meten.

Een optimalisatie-algoritme is gepresenteerd dat de prestaties van de antenne verder

verbeterd. Dit algoritme optimaliseert zowel de bandbreedte als de stralingsefficiëntie van het antenne element en geeft de ontwerper de flexibiliteit om het beste antenne-ontwerp te vinden voor de toepassing. Hierna is het antenne-element in een antennestelsel geplaatst zodat bundelvorming mogelijk is. De bundelvorming van het antennestelsel is onderzocht en hierbij is gekeken naar stralingsefficiëntie, bandbreedte en versterking. Metingen aan antennestelsels tonen aan dat de antenne zeer goed gebruikt kan worden om de vereiste versterking en bundelvorming te realiseren.

Ook de integratie van de antenne en de radio-elektronica is onderzocht. Verschillende integratie topologieën zijn besproken en een prototype is gemaakt in printplaattechnologie waarin een vermogensversterker en een antenne-element zijn geïntegreerd. Het is aangetoond dat deze technologie succesvol gebruikt kan worden om een module te realiseren waarin een antennestelsel en bijbehorende radio-elektronica zijn geïntegreerd. De gepresenteerde concepten kunnen daarom direct benut worden voor de realisatie van een complete radiozendontvangmodule waarin een antennestelsel is geïntegreerd dat in staat is tot bundelvorming. Een dergelijke module ondersteunt draadloze communicatie met datasnelheden van gigabits per seconde.

# Acknowledgements

# Curriculum Vitae

Johannes A.G. Akkermans was born in Wouw, The Netherlands on July 18th, 1980. After the completion of secondary school at the Norbertuscollege in Roosendaal he started as a student in Electrical Engineering at the Eindhoven University of Technology. The research for the final project of his M.Sc. thesis was performed within TNO Science and Industry and was concerned with rectenna design for wireless low-power transmission. He received his M.Sc. degree in Oktober 2004.

In November 2004 he started working towards the Ph.D. degree within the Radiocommunications group at the Eindhoven University of Technology. His Ph.D. research involved the development of planar beam-forming antenna arrays for 60-GHz broadband communication. From September 2005 to May 2006 he did his research on millimeter-wave antennas at TNO Defence and Security and from January 2008 to May 2008 he contributed to the development of 60-GHz beam-forming antenna arrays at Thomas J. Watson research center. Results of his M.Sc and Ph.D. research have been published in international journals and conferences. Moreover, he contributed to several patent applications.